

Aus dem Max-Planck-Institut für Kolloid- und Grenzflächenforschung

Crystallization, Biomimetics and Semiconducting Polymers in Confined Systems

Dissertation

Zur Erlangung des Akademischen Grades
Doktor der Naturwissenschaften (Dr. rer. nat.)
in der Wissenschaftsdisziplin Physikalische Chemie

eingereicht an der
Mathematisch-Naturwissenschaftlichen Fakultät
der Universität Potsdam

von
Rivelino V. D. Montenegro
geboren am 23.10.1973 in Mossoró, Brasilien

Golm, Februar 2003

Die vorliegende Arbeit entstand in der Zeit von November 2000 bis Februar 2003 am Max-Planck-Institut für Kolloid- und Grenzflächenforschung, Golm.

Gutachter:

- Prof. Dr. M. Antonietti
- Dr. habil. K. Landfester
- Prof. Dr. U. Scherf

Tag der mündlichen Prüfung: 21.05.2003

We must draw our standards from the natural world. We must honor with the humility of the wise the bounds of that natural world and the mystery which lies beyond them, admitting that there is something in the order of being which evidently exceeds all our competence.

Vaclav Havel

...Consider the lilies of the field how they grow? they toil not, neither do they spin? And yet I say to you, that even Solomon in all his glory was not arrayed like one of these.

Jesus (Mat. 6:28-29)

Table of contents

<i>1 Introduction</i>	9
<i>2 Theoretical Section</i>	12
2.1 Heterophases Systems	12
2.1.1 Emulsions	12
2.1.2 Miniemulsions	13
2.1.3 Artificial Latex	19
2.2 Crystallization	21
2.2.1 Undercooling	21
2.2.2 Nucleation	23
2.2.3 Homogeneous nucleation	26
2.2.4 Heterogeneous nucleation	28
2.2.5 Crystal growth	29
2.2.6 Crystallization in confined systems	29
2.2.7 Metastable phases in alkanes	32
2.3 Bioengineered, biomimetics and self-assembling materials	33
2.3.1 Gelatin nanoparticles	34
2.3.2 Hydroxyapatite (HAP)	35
2.4 Semiconducting polymers	37
2.4.1 Principles of semiconducting polymer	37
2.4.2 Semiconducting polymer layers	38
2.4.3 Polymer mixtures	39
<i>3. Relevant methods for characterization</i>	42
3.1 X-ray Diffraction	42
3.1.1 Determination of crystallite sizes	43
3.2 Dynamic Light Scattering (DLS)	44
3.3 Atomic Force Microscopy (AFM)	46
3.4 Differential Scanning Calorimetry (DSC)	49
<i>4 Results and discussion</i>	52
4.1 Crystallization in miniemulsion droplets ^[163]	52
4.1.1 Direct Miniemulsion Systems	52
4.1.2 Inverse Miniemulsion	60
4.2 Metastable phases (rotator phase) in n-alkanes	64
4.2.1 Even alkanes	65
4.2.2 Odd-alkanes	72
4.3 Bioinspired materials	79

4.3.1 Gelatin nanoparticles	79
4.3.2 Biomineralization of hydroxyapatite within gelatin nanoparticles	89
4.4 Semiconducting polymer nanoparticles	95
4.4.1 Semiconducting polymer aqueous dispersions ^[175]	95
4.4.2 Fabrication of an Organic Light Emitting Diode (OLED) ^[179]	102
4.4.3 Blends of semiconducting polymers ^[183]	106
5 Conclusions	116
6 Experimental Section	119
6.1 Crystallization in miniemulsion droplets	119
6.2 Metastable phases (rotator phase) in n-alkanes	119
6.3 Gelatin Nanoparticles	120
6.4 Biomineralization of HAP within gelatin nanoparticles	121
6.5 Semiconducting polymer nanoparticles	122
7 Appendix	125
7.1 Methods	125
7.2 Abbreviations and symbols	127
8 References	129

1 Introduction

Wilder Bancroft, an American Pioneer in the field of colloid chemistry, summarized the importance of the studies on colloids when he said that colloid chemistry is "*essential to anyone who really wishes to understand oils, greases, soaps, glue, starch, adhesives, paints, varnishes, lacquers, cream, butter, cheese, cooking, washing, dyeing, colloid chemistry is the chemistry of life.*"^[1] By that time nearly half of each volume of the *Journal of Physical Chemistry* dealt with colloids. Seventy years later, Bancroft's belief is even more evident. The colloidal systems are present everywhere in many varieties such as emulsions (liquid droplets dispersed in liquid), aerosols (liquid dispersed in gas), foam (gas in liquid), etc. The studies on chemistry and physical chemistry of colloids are each day becoming more and more relevant. The developments of new techniques for the studies of colloids and methods of preparation have increased drastically in the last years. Among several new methods for the preparation of colloids, the so-called miniemulsion technique has been shown to be one of the most promising. Miniemulsions are defined as stable emulsions consisting of droplets with a size of 50-500 nm by shearing a system containing oil, water, a surfactant, and a highly water insoluble compound, the so-called hydrophobe.^[2] The advantages of this method include the narrow size droplet distribution, the droplet and subsequent particle size control and low amount of surfactant needed for stabilization. The nanodroplets can also be used as nanoreactors, where a large variety of chemical reactions can be performed. Moreover, this technique is not restricting just to the field of heterophase polymerization, but also in the creation of composites and hybrid materials, formulation of exquisite particle morphologies, along with many other applications. Therefore it is a strong tool for new areas such as nanotechnology, in the fabrication of nanocomponents for electronic devices or nanorobots, in pharmacy and medicine, for the preparation of drug delivery carriers with functional properties, e.g. target specific, or gene containing particles for tissue repair. Despite all the technological applications and the worldwide use of emulsions there are still many basic aspects, which are not fully understood, such as the unusual crystallization behavior of nanometer droplets. The differences in the crystallization between bulk and miniemulsion droplets have been examined for *n*-alkanes and water

during phase transition (sections 4.1 and 4.2), given that crystallization is a crucial phenomenon in nature, science and technology, such studies are of vital importance for the understanding of crystallization in confined structures, which have a strong influence in on macroscopic properties of the materials.

In order to develop superior materials, the scientists started to look to nature for inspiration, given that biology has had to solve engineering problems since the beginning of life on earth. Just as Da Vinci and other scientists and artists found inspiration from natural structures, modern scientists are also following this trend. Therefore in the last years there was a renaissance attempt to mimic nature from the molecular level to the macroscopic world. The design constraints and objectives are: functionality, optimization and cost effectiveness.^[3] The word *biomimetics* was then first used at a workshop in 1991 organized by the US air force office of scientific research. Its purpose was to look at what biology had to offer in terms of design and processing of materials. Since then the meaning has been broadened and a better definition of its current objectives as a discipline is the one coined by Vincent – “the abstraction of good design from nature”^[4]

The combination of the miniemulsion approach, natural polymers and the biomimetic concept can bring about very significant products with potential applications, for example, in medicine. A straightforward way of producing cross-linked gelatin nanoparticles is presented in section 4.3.1, where due to the thermo-reversible property of gelatin, the nanoparticles can be swollen and shrunk by a change of temperature when dispersed in water. Such nanoparticles have potential drug delivery applications, since gelatin, a natural polymer obtained from collagen, has the advantage of been recognized and able to interact with the biological environment, and the problems of the toxicity and stimulation of a chronic inflammatory reaction (that are often provoked by synthetic polymers) may be avoided.

In biology the combination of simple components and the way the architecture and interaction can bring the formation of better and tailored properties. For example collagen, which is highly elastic in the case of blood vessels, generates in combination with nanocrystals of hydroxyapatite (a biomineral) rigid materials such as bone via a biomineralization process.^[5]

Although the precipitation of biominerals such as hydroxyapatite, calcite etc. is a fairly common laboratory process, the control over the shape, size, orientation and assembly of the crystals is a much more complex task.^[3]

Thus the gelatin nanoparticles synthesized in section 4.3.1 are used in this work, (as reported in the section 4.3.2) as nucleation sites for the biomineralization of nanocrystals of hydroxyapatite. The hydroxyapatite crystals grow in the framework of the gelatin, resulting in the ability to control the morphology of the hydroxyapatite. As a result a hybrid material is obtained that can be used as a bone implant.

But not only bioengineering products can be produced from the combination of miniemulsions and other ideas. It will be shown in section 4.4 that benefits are also obtained from a combination of miniemulsions and artificial latexes in the field of optics and electronics. Miniemulsions are very useful in the preparation of aqueous polymer dispersions from conjugated polymers. These are semiconductors, therefore they can be used in a large range of applications such as light emitting diodes, solar cells, field effect transistors, organic wires, non linear optics, photoconductivity and much more. Given that such polymers are basically soluble only in an organic solvent, the transfer to an aqueous media brings several advantages, such as environmentally friendly products and it has a feasible application in inject printing technology. Furthermore it is also demonstrated how valuable the miniemulsion method is for the phase separation control on the nanometer scale via energy-transfer experiments.

2 Theoretical Section

2.1 Heterophases Systems

2.1.1 Emulsions

Oil and water do not mix. This observation is rather obvious and is easily observed everywhere: in the chemical laboratory, the oil field, and the kitchen. However, in many occasions the mixture of oil and water is desirable, and we accomplish this by means of emulsification. Thus an emulsion is defined as a heterogeneous system of two immiscible liquids in which one is dispersed in the other. There are two principal ways to prepare emulsions: the destruction of a large volume into smaller sub-units (comminution method) or the construction of emulsion droplets from smaller units (condensation method).^[6]

The emulsions are divided in “direct”, oil in water (o/w) and “inverse”, water in oil (w/o) emulsions, depending whether the continuous phase is aqueous or organic. The formation of o/w or w/o emulsions depends on the chosen emulsifier, the water to oil ratio and the temperature.

Using similar amounts of oil and water, it is important to consider the difference in the surface tension between the aqueous phase and hydrophilic block of the surfactant (γ_{A-H}) on one hand and the difference in surface tension between the organic phase and the lipophilic block of the surfactant (γ_{O-L}) on the other hand. An oil in water emulsion is formed if $\gamma_{A-H} - \gamma_{O-L} < 0$ and water in oil emulsion is formed if $\gamma_{A-H} - \gamma_{O-L} > 0$.^[7]

The term emulsion is subdivided into *macroemulsion*, *miniemulsion* and *microemulsion* with regard to some parameters, such as droplet size, amount of surfactant, stability, etc. The droplet sizes for macroemulsion, miniemulsions and microemulsions are in the range of several micrometers, hundreds of nanometers, and some tens of nanometers, respectively. The amount of surfactant used for emulsification and the stability of the emulsion are also used to differentiate the three kinds of emulsion. While in microemulsions the amount of surfactant often exceeds the amount of the dispersed phase, in miniemulsion and macroemulsion the surfactant content can be lower than 1% of the dispersed phase. Only microemulsions are thermodynamically stable, although,

macro and miniemulsions can be prepared in such way that their structure remains unchanged over longer periods of time, even up to years.

Moreover, while for the preparation macro- and miniemulsions one has to use shear forces (mechanical agitation, ultrasound, etc.), the microemulsions are formed spontaneously.

Furthermore miniemulsions are stable against molecular diffusion (Ostwald ripening) whereas macroemulsions are not. Miniemulsions will be discussed more in details in following section.

These types of emulsions have been subject to polymerization for the production of polymeric dispersions in continuous media, which enjoy great popularity in academy and industry. Among the reasons for this great popularity one can mention the searching for environmentally friendly products, since in general the solvent is water. On other hand, there is a technological trend towards a high solid content of polymer formulations, e.g., to minimize shrinkage effects or to shorten processing times. High polymer contents at reasonable processing viscosities can only be obtained by polymer dispersions, either in water or hydrocarbon solvents.

As a third advantage, polymer particles in dispersions allow one to control or imprint an additional length scale into a polymer bulk material, given by the diameter of the particle, which is offered by the process of film formation ‘for free’. That way, polymer materials can be generated employing rational structure design not only on the molecular scale, but also on the mesoscale, and superior rubbers or shock resistant thermoplastics are obtained.^[8]

2.1.2 Miniemulsions

Destabilization and breaking of emulsions can take place either by coalescence or by molecular diffusion degradation. Stabilization of emulsions against coalescence can be obtained electrostatically or sterically. In order to create a stable emulsion of very small droplets, which is, for historical reasons, called a miniemulsion (as proposed by Chou et al.,^[9]) the droplets must be also stabilized against molecular diffusion degradation, (called Ostwald ripening, a unimolecular process or τ_1 mechanism) *and* against coalescence by collisions (a bimolecular process or τ_2 mechanism).

The preparation of an emulsion results in a distribution of droplet sizes. Even when the surfactant provides sufficient colloidal stability of droplets, the outcome of this size distribution is determined by their different droplet or Laplace pressures, which increase with decreasing droplet sizes resulting in a net mass flux by diffusion between the droplets.^[8] If the droplets are not stabilized against molecular diffusion, small ones will disappear, increasing the average droplet size (Ostwald ripening).^[10]

Many theoretical works have been done in order to examine the diffusion process. It was stated that the emulsion stability is proportional to the particle volume^[11] and another work^[12] has shown that changes of the particle size distribution function are in accordance with the predictions of the Lifshitz-Slyozov theory.^[13]

The addition of a sufficient number of molecules (a third component) that are insoluble in the continuous phase and hence trapped within droplets can provide the stabilization against Ostwald ripening. An “osmotic stabilization” takes place, since the trapped molecules provide an osmotic pressure, which counteracts the Laplace pressure due to the surface tension^[14]. The idea of osmotic stabilization was brought to emulsion after the observation that droplets of aerosols or fog can be stabilized by the presence of a non-volatile third component.^[15] A thermodynamic description of this phenomenon was later given by La Mer et al. in 1952^[16], still for the aerosol case.

The obtained stability in so-called miniemulsions is discussed in the literature to be *metastable* or *fully stable*. According to Webster et al.^[14], who studied emulsions whose droplets contain a trapped species (insoluble in the continuous phase) even when the emulsion is polydisperse in both size and composition, the third compound can provide ‘full’ stability. As previously suggested by Kabalnov et al.^[12] a weaker condition for stability is sufficient only to prevent ‘spinodal’ coarsening and is best viewed as a condition for metastability. The coarsening of unstable emulsions is considered and shown at long times to resemble that of ordinary emulsions by the competition between the osmotic pressure of the trapped species and the Laplace pressure of the droplets. This is of high importance for the production of stable emulsions and miniemulsions. The increased stability that is provided by white mineral oil or other ripening inhibitors^[17] is technologically used in fields such as anesthetic/analgesic emulsions.

The rate of Ostwald ripening depends on the size, the polydispersity and the solubility of the dispersed phase in the continuous phase. This means that a hydrophobic oil dispersed as small droplets with a low polydispersity already shows slow net mass exchange, but by addition of an ‘ultrahydrophobe’, the stability can still be increased by additionally building up a counteracting osmotic pressure. This was shown for fluorocarbon emulsions, which were based on perfluorodecaline droplets stabilized by lecithin. By adding a still less soluble species, e.g., perfluorodimorphinopropane, the droplets' stability was increased and could be introduced as stable blood substitutes.^[18]

According to Davis et al.,^[19] the added material reduces the total vapor pressure as defined by Raoult's law. Thus in the case of the pure oil system, the smaller droplets will have a slightly higher vapor pressure (or solubility) than the larger ones. Therefore to reach equilibrium, the constituting oil will leave the small droplets and migrate to larger droplets. This loss will cause an increase in the mole fraction of the ultrahydrophobe in the small droplets and a decrease in the large droplets. Thus the small droplets will now have an osmotically reduced vapor pressure with respect to the larger droplets, which will continue until pressure equilibrium is obtained. In no case, droplets can disappear by this mechanism.^[8]

In addition to the molecular diffusion of the dispersed phase, collision and coalescence processes can cause a destabilization of emulsions. However this problem is usually solved by addition of appropriate surfactants, which provide either electrostatic or steric stabilization to the droplets.

2.1.2.1 Preparation and homogenization of miniemulsions

The formation of emulsions starts from a premix of the phases, which contain surface-active agents and further additives. The emulsification process requires the deformation and disruption of droplets, in order to increase the specific surface area of the emulsion. These newly formed interfaces have to be stabilized by surfactants.

Different methods can be used to promote the homogenization of emulsions to miniemulsions. Simple stirring was very frequently used in the beginning of the miniemulsion research. However, the energy transferred by these techniques is not enough to obtain small and homogeneously distributed droplets.^[20] Therefore a much

higher energy for comminuting large droplets into smaller ones is required, significantly higher than the difference in surface energy $\gamma\Delta A$ (with γ - surface/interfacial tension and ΔA - difference between former and the newly formed interface), since the viscous resistance during agitation absorbs most of the energy. The excess energy is dissipated as heat.^[21]

Nowadays the use of ultrasonication became very popular as a source of high energy, particularly for the homogenization of small quantities, whereas rotor-stator dispersers with special rotor geometries, microfluidizers or high-pressure homogenizers are favorable for the emulsification of larger quantities.

The first report about power ultrasound emulsification appeared in 1927.^[22] Several possible mechanisms of droplet formation and disruption under the influence of longitudinal density waves have been reported.^[23] One is the formation of droplets as a consequence of unstable oscillations of the liquid-liquid interface. These capillary waves may occur and have a contribution only if the size of droplets to be disrupted is sufficiently larger than the wavelength of the capillary waves. For ordinary systems of oil and water, this wavelength is in the range of 10 μm ,^[24] which is the usual size of droplets in a premix for continuous emulsification. Therefore, in such a system droplet formation or disruption by capillary waves is not likely.

The oscillation and subsequent disruption of droplets due to the action of sound is regarded as a mechanism related to that of capillary waves. The corresponding resonance radius at a frequency of 20 kHz is once more in the region of some 10 μm . This process has to be taken into account only for a small fraction of droplets with diameters exactly matching the resonance frequencies. For the case of an usually broad droplet size distribution in an emulsion premix, a wide range of sound frequencies would be a requirement for this mechanism to become the leading one.

The mechanism of cavitation is generally regarded as crucial under practical conditions.^[25] Parameters positively influencing cavitation in liquids improve emulsification in terms of smaller droplet size of the dispersed phase right after disruption. Imploding cavitation bubbles cause intensive shock waves in the surrounding liquid and the formation of liquid jets of high velocity with enormous elongational fields.^[26] This may cause droplet disruption in the vicinity of the collapsing bubble.

However, the exact process of droplet disruption, due to ultrasound as a result of cavitation, is not yet fully understood. At constant energy density, the droplet size decreases when adding stabilizers, whereas the viscosity of the oil in water-in-oil emulsions has no effect.^[27] This clearly indicates strong elongational flow components. As factors that influence droplet size in miniemulsions, can be mentioned the ratio of the dispersed to continuous phase, the density of the dispersed phase, the solubility and amount of surfactant. Initially the droplet size in miniemulsions is a function of the amount of mechanical agitation.^[28] The droplets also change rapidly in size throughout sonication in order to approach a pseudo-steady state. Once this state is reached, we found that the size of the monomer droplet is a function of the applied mechanical energy, assuming a required minimum is used. In the beginning of homogenization, the polydispersity of the droplets is still quite high, but by constant fusion and fission processes, the polydispersity decreases, the miniemulsion reaches then a steady state (see Figure 2.1).^[29]

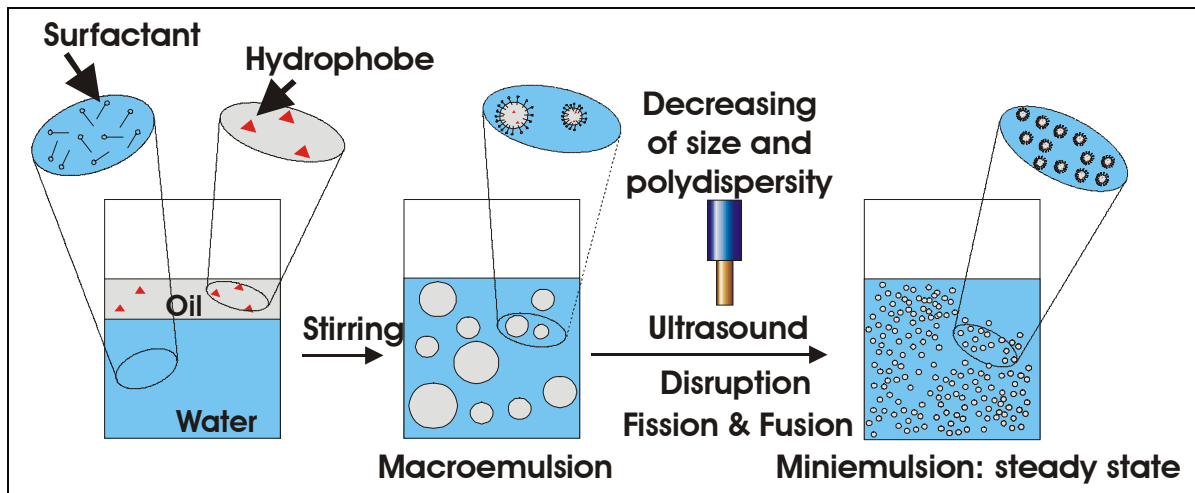


Figure 2.1. Scheme for the formation of a miniemulsion by ultrasound (US).

With increasing time of ultrasound, the droplet size decreases and therefore the entire interface oil/water increases. Since a constant amount of surfactant has now to be distributed onto a larger interface, the interfacial tension as well as the surface tension at

the air/emulsion interface increases since the droplets are not fully covered by surfactant molecules.

2.1.2.2 Inverse miniemulsions

The preparation of miniemulsion is not restricted to the classic example of oil-in-water emulsion, but the concept can be extended to inverse miniemulsions where an aqueous phase is dispersed in an organic media. In this case an agent insoluble in the continuous oily phase, a so-called ‘lipophobe’, builds up the osmotic pressure. As examples of ‘lipophobe agents’ for water-in-oil miniemulsions one can mention ionic compounds, simple salts or sugars, because they show a low solubility in organic solvents.^[30] Another adaptation of the process is that for the dispersion of polar compounds in non-polar dispersion media, surfactants with low HLB (hydrophilic-lipophilic balance) values are required. A number of surfactants were screened, including standard systems such as C₁₈EO₁₀, sodium bis(2-ethylhexyl)-sulfosuccinate (AOT), sorbitan monooleate (Span80), and the nonionic block copolymer stabilizer poly(ethylene-*co*-butylene)-*b*-poly(ethylene oxide) (P(B-E)/PEO, see Figure 2.2). P(B-E)/PEO turned out to be the most efficient due to its polymeric and steric demanding nature, providing maximal steric stabilization which is the predominant mechanism in inverse emulsions. A comparison of the direct and inverse miniemulsion is given in Figure 2.3.

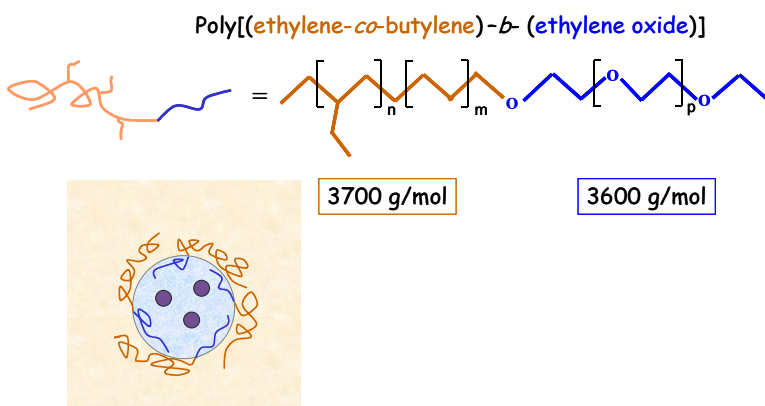


Figure 2.2. Amphiphilic block copolymer P(B-E)/PEO for the stabilization of inverse miniemulsions.

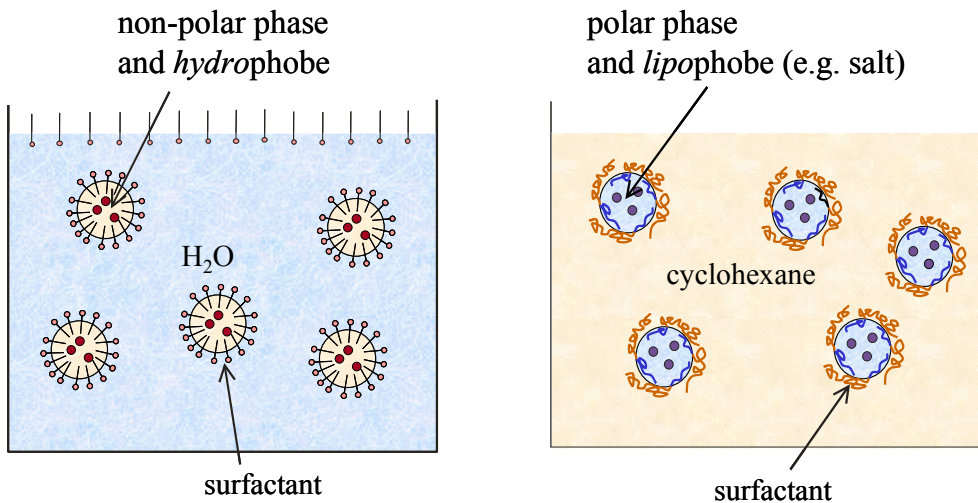


Figure 2.3. Comparison between direct and inverse miniemulsions.

The droplet size throughout the miniemulsification process runs into an equilibrium state (steady-state miniemulsion), which is characterized by a dynamic rate equilibrium between fusion and fission of the droplets, as it can be determined by turbidity measurements, as in the direct system (oil-in-water).^[8]

It seems that in inverse miniemulsions, the droplets undergo already shortly after miniemulsification a real zero-effective pressure situation (the osmotic pressure counterbalances the Laplace pressure), which makes them very stable. This is hypothetically attributed to the different stabilization mechanism and mutual particle potentials, which make a pressure equilibration near the ultrasonication process possible.

2.1.3 Artificial Latex

Polymer latexes can be obtained by polymerization of monomers in heterophase, e.g. in emulsion, miniemulsion, suspension, microemulsion polymerization, but latexes can also be prepared as secondary dispersions, also called *artificial latexes*. In this case the polymer is prepared prior to emulsification. It is then dissolved in a proper solvent, followed by emulsification of the low viscosity polymer solution. In a last step, the solvent is removed from the emulsion resulting in a polymer dispersion.^[8] The Figure 2.4 shows a simple scheme of the process.

Among the advantages of artificial latex one can cite the production of aqueous polymer dispersion for those cases where pure materials are needed, for example semiconducting polymers, because the polymerization of such materials is not viable in emulsions, since the removal of the catalyst is a major problem.

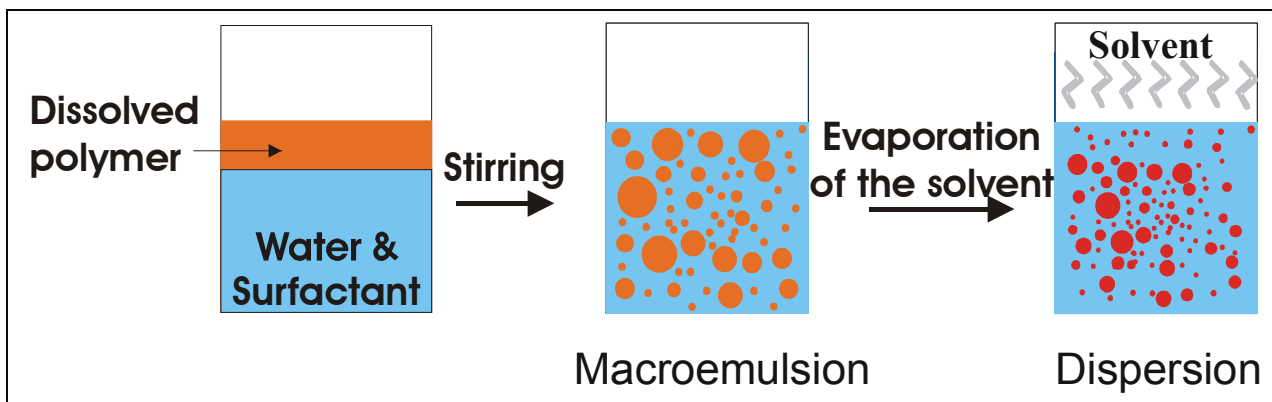


Figure 2.4. Basic principle of the preparation of artificial latex.

Generally for environmental and economic reasons the solvent should be separated easily from water. Thus toluene has been widely used as solvent, although, other hydrocarbons and chlorinated hydrocarbons are also possible.

For the preparation of artificial latexes the choice of the surfactant is a critical point, since the surfactant must survive the temperature and mechanical forces of the stripping operation and of course give final latex, which is mechanically stable.

Another important parameter is the viscosity of the initial dissolution phases what according to Burton and O'Farrell^[31] must be below 10 Pa·s (10.000 cps) in order to obtain the emulsion.

In the early 1923 first reports about artificial latex had been published by Tuttle^[32-34] and Ditmar^[35] who showed the preparation of latexes of rubber, gutta percha, and balata to be viable processes. Such artificial latexes were first used to the papermaking process, in the production of waterproof cloths,^[33] inner tubes^[34] and more hygienic mattresses.^[35]

Using the artificial latex concept, Beerbower et al.^[36] have reported the preparation of a chemically sensitive, mechanically stable and low unsaturated elastomer, such as butyl rubber, emulsion with roughly 50-68% solid content and a desirably low viscosity. Vanderhoff et al.^[37] reported the preparation of artificial latex made from different

polymers, such as: polystyrene, polyesters, epoxies, and cellulose derivatives. Also the use of different surfactant was investigated.

The preparation of a secondary dispersion of epoxy resin/curing agent is also described in order to obtain positively charged latex particles for coating purposes.^[38]

More recently Johnsen et al.^[39] reported the preparation of a thermally gellable artificial latex comprising of a stable aqueous colloidal dispersion of a preformed multiblock copolymer, which can be used for the fabrication of gloves, condoms or balloons.

Artificial latexes are also regarded as relatively uncomplicated processes and capable of operation without difficulty and/or at relatively low cost.

2.2 Crystallization

The crystallization is one of the most observable physical phenomena in the nature, from the water that freezes forming crystals of ice to the magma of a volcano that cools forming rocks, or a protein molecule that freezes forming a single crystal. The crystallization phenomenon is observed everywhere and has been used along the ages in many industrial processes such as sugar purification, the production of marine salt, the fabrication of metallic alloys and metallic crystals for electronic devices, etc. The crystallization is a phase separation and it is influenced by several kinetic and thermodynamic parameters. Therefore, in order to crystallize a system one has to overcome an energetic barrier, what is directly observed in an undercooling state of the system. The crystallization is commonly subdivided in two basic processes, first the nucleation, which is related to the aggregation of small entities to form the crystal embryo and secondly the crystal growth, which is governed by a process of molecular recognition at the growing interfaces, been a process of self-assembly of molecules into a lattice.

2.2.1 Undercooling

Fahrenheit initiated the investigation of phase equilibrium and undercooling in 1714 when he conducted the first recorded systematic study on the crystallization of water.^[40]

He found that boiled water in a sealed, airtight container could be kept overnight at the undercooled temperature of 15 °F (-9,4 °C) without crystallization. The introduction of

small ice particles however initiated the crystallization, at the temperature of ice-water mixture of 32 °F (0 °C), the melting temperature of water at atmospheric pressure. He noticed that a sudden jar to the container of undercooled water also initiated crystallization. As described by Dunning,^[41] these observations were confirmed rapidly and extended to other liquids.^[42] Lowitz^[43] first observed supersaturation in a salt solution and noted the analogy with undercooled water. Gay Lussac^[44] showed that supersaturation is a general phenomenon and supported Fahrenheit's observation of the effects of motion by demonstrating that shaking, scratching, and rubbing could also induce crystallization.

Schröder, von Dusch, and Violette recognized that the observed variability of results was due largely to airborne particles and particles residing in the containers.^[45] When these were partially eliminated, more consistent measurements were obtained.^[46] A particular relationship with the crystallization product was necessary for a strong catalytic effect of the heterogeneity. Lowitz^[43] found that seeding of supersaturated solutions or undercooled liquids with small crystallites of the stable phase led to rapid crystallization, while unrelated particles often had little effect. Ostwald^[47] demonstrated that only very small seeds in the ppm range were sufficient to crystallize sodium chlorate solutions.

Boisbaudran^[48] produced the first evidence for a metastability limit, he found that homogeneous nucleation occurred in highly supersaturated salt solutions, but did not occur in less supersaturated ones. De Coppet^[49] measured the average time lag before crystallization in solutions of known supersaturation. Ostwald^[47,50] defined two types of supersaturated solutions: (1) metastable solutions, which in the absence of heterogeneous sites would remain unchanged for long time, and (2) labile solutions, which will crystallize within a short time (at low undercooling). Tammann^[51] observed this boundary as a function of undercooling in piperine. In both regions, however, the transformation was initiated by a nucleation mechanism.

Gibbs^[52] first realized that the formation of a new phase requires as a necessary prerequisite the appearance of small clusters of building units (atoms or molecules) in the volume of the supersaturated phase (vapors, melt or solution).^[53] He considered these nuclei as small liquid droplets, vapor bubbles or small crystallites, or, in other words, small complexes of atoms or molecules which have the same properties as the

corresponding bulk phases with the only exception being that they are small in size. Although oversimplified, this picture has been a significant step towards the understanding of the transitions between different states of aggregation, because when phases with small sizes are involved the surface-to-volume ratio turns out to be large compared with that of macroscopic entities. Then the fraction of the Gibbs energy of systems containing small particles, which is due to the surface energy, becomes considerable. Moreover, this approach allows a description of phases with finite sizes in terms of such macroscopic thermodynamic quantities as specific surface and edge energies, pressure, etc.^[53] Following the first works of Gibbs, contributions of Volmer and Werner,^[54] Farkas,^[55] Stranski and Kaischew,^[56] Becker and Döring,^[57] Frenkel^[58] and others established the so-called *classical* theory of nucleation.

While of extreme importance to physics, chemistry, and materials science, crystallization of a liquid is only one example of a nucleation-initiated first-order phase transformation. Other examples are known in diverse physical systems. These include the condensation of supersaturated water vapor (rain), the phase separation in metallic alloys, polymers, liquids, and vapors, the crystallization (devitrification) of glasses, the orientational ordering in molecular crystals and nematic liquids, and the domain formation in ferromagnetic systems. The subject of nucleation is therefore an extremely broad one that continues to receive a considerable amount of experimental and theoretical attention.^[59]

2.2.2 Nucleation

The nucleation of a new phase or a crystal does not happen automatically in a supersaturated solution. The right conditions must be achieved for the nucleus to grow to a crystal. Nucleation sites are usually related with a low energy location in the melt, sites that offer a chance to atoms to diminish energy.

In a melt, atoms statistically approach each other up to the interatomic spacing of a solid and form clusters for short time. If $T > T_m$ (T_m the melting temperature) a cluster decays spontaneously. At the melting temperature ($T = T_m$) the thermodynamic equilibrium of the free energies of the solid (G_s) and the liquid (G_l) is reached (see Figure 2.5). As soon as the temperature is below the melting temperature ($T < T_m$) the clusters can grow.

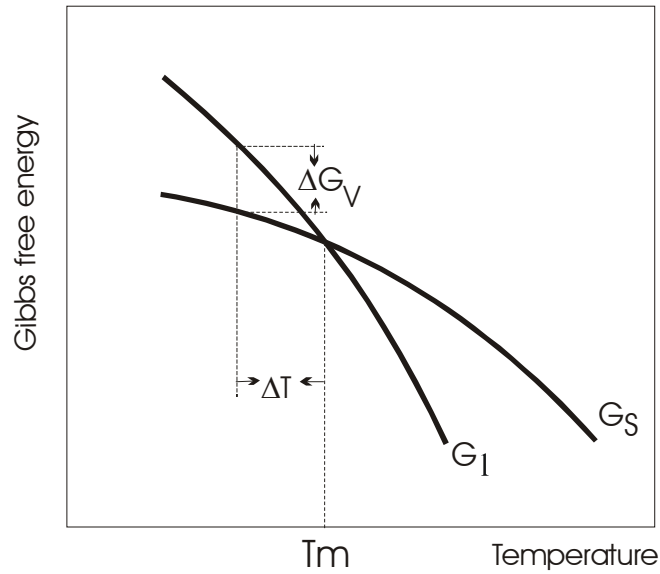


Figure 2.5. Gibbs free energies for solid (G_s) and liquid (G_l) versus the temperature. The free energies of solid (G_s) and liquid phase (G_l) are equal at T_m (melting temperature).

Undercooling by a temperature of $\Delta T = T_m - T$, leads to $G_s < G_l$ and $\Delta G_v = G_s - G_l$. Then spontaneous growth of the clusters is expected to occur, because negative ΔG_v should drive crystallization. However the cluster is characterized by a liquid-solid interface and exhibits the interface energy γ . That interface energy is a positive value and therefore acts as barrier against crystallization.

According to Gibbs, phase transformations in the metastable region are initiated by nucleation; phase transformations in the unstable region occur by spinodal mechanism involving long-range fluctuations of infinitesimal amplitude. This is illustrated schematically in Figure. 2.6a for the case of phase separation of a binary alloy. The solid line indicates the coexistence curve as a function of alloy composition. A Quench into the metastable region results in a transformation, which proceeds by nucleation and growth. The boundary of the spinodal region (quench m) within which phase transformations proceed by the spinodal mechanism (quench u) is called the spinodal curve and is noted in Fig. 2.6a. It is defined as the locus of points inside the coexistence curve for which the curvature of the free energy changes from convex to concave (Fig. 2.6b), (e.g. from positive to negative curvature). As seen in the Figure 2.6.b, the energy increases with a

spontaneous concentration fluctuation in the region, giving rise to an energetic barrier that stabilizes the system in the metastable state. No energetic barrier to phase separation exists in the spinodal region where the system is unstable to spontaneous fluctuations.

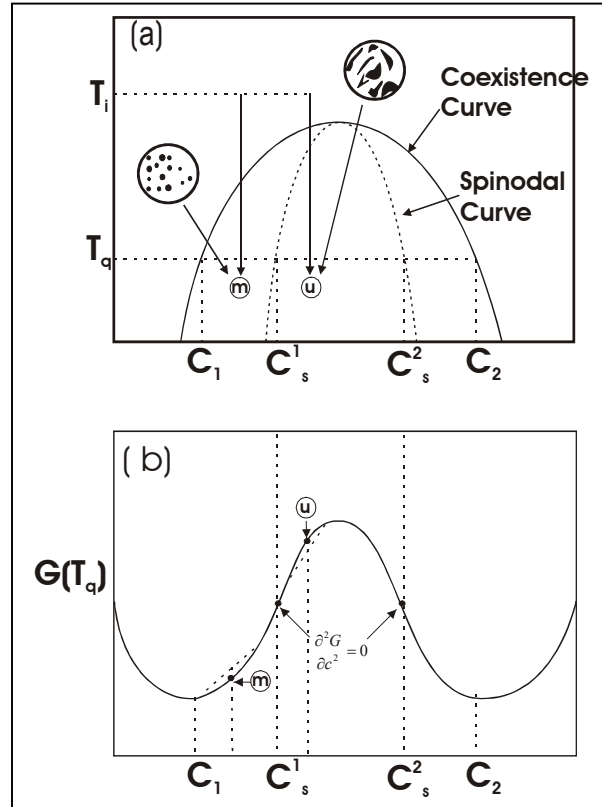


Figure 2.6. a) Scheme of the morphology of a crystallizing liquid obtained by quenching into the metastable (m) or unstable (u) regions. The liquid-solid coexistence and the classical spinodal curves are indicated. b) Schematic diagram showing the relation of the boundaries of the spinodal and coexistence regions to the shape of the Gibbs free energy curve.^[59]

As illustrated schematically in Figure 2.6, a nucleation-initiated phase transformation generally produces a certain morphology in a droplet. An interconnected structure results from a spinodal transformation. The phase morphology alone, however, is insufficient to identify unambiguously the transformation mechanism,^[60] since an interconnected structure can also result from the superposition of many separately nucleated grains.

Therefore, spinodal mechanism is best identified from the small-angle X-ray scattering experiments.^[61]

For the nucleation the kinetic barrier is very large, and the probability of occurrence for a significant number of fluctuations leading to the stable phase is infinitesimal. At large deviations from the equilibrium, but still within the metastability region, this barrier decreases to a few $k_B T$, defining a limit on metastability for which these fluctuations are present in appreciable numbers among the equilibrium fluctuations that describe the liquid state.^[59]

The nucleation can take place by two different mechanisms: homogeneous or heterogeneous nucleation. Heterogeneous happens in the metastable phase with nucleus, whereas homogenous at spinodal curve.

2.2.3 Homogeneous nucleation

Theoretically, homogeneous nuclei are formed by an aggregate of critical size cluster (modeled as tiny spheres for simplicity), which is in unstable equilibrium with the mother liquor.^[62]

In fact the energy required to form a spherical nucleus of radius r can be written as:

$$\Delta G = \frac{4}{3}r^3\Delta G_v + 4\pi r^2\gamma \quad (\text{Eq. 2.1})$$

where ΔG_v is the Gibbs' free energy per unit volume, $\frac{4}{3}\pi r^3$ is the volume of the spherical cluster, $4\pi r^2$ its surface area, and γ the interfacial tension.

The energy required to form a critical nucleus of radius r^* (Figure 2.7) can be written as

$$\Delta G^* = \frac{16}{3}\pi r^3\Delta G_v^2 \quad (\text{Eq. 2.2})$$

ΔG^* (what is the maximum value for ΔG) is the activation barrier against crystallization which occur exactly at r^* .

The clusters are either embryos or nuclei, depending on the required activation energy. They are embryos if $r < r^*$ (surface/volume ratio large) what leads to a spontaneous decay, as further energy is required to reach ΔG^* . But they are nuclei if $r > r^*$, thus a crystal grows by lowering its free energy.

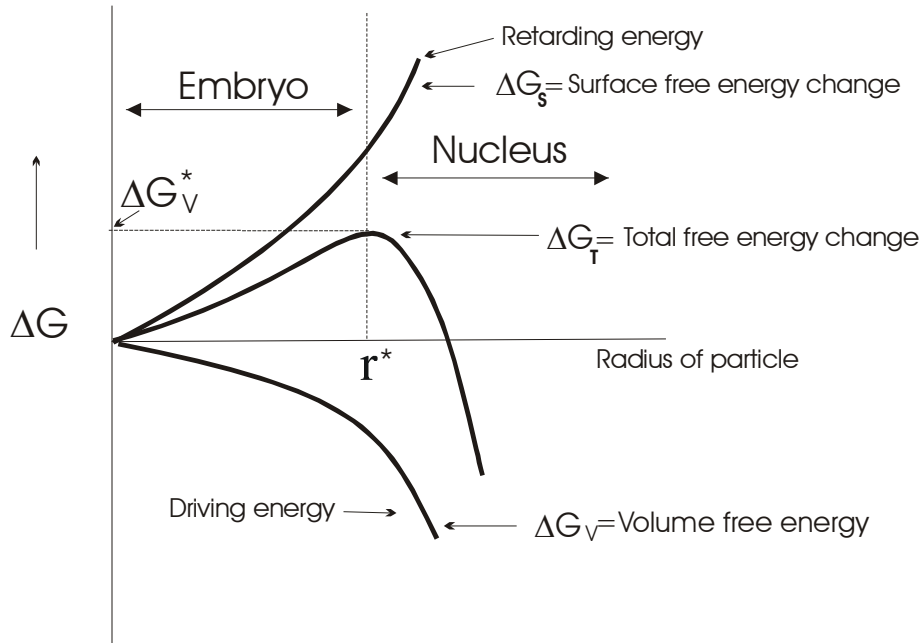


Figure 2.7. Scheme for the formation of the crystals. Beyond r^* a growth of the nucleus leads to a decrease of the Gibbs free energy of the system.

The rate of homogeneous nucleation J for stationary conditions is given by:

$$J = \left(\frac{dN}{dT} \right) \frac{1}{V} = A_k \exp\left(\frac{-\Delta G^*}{kT} \right) \quad (\text{Eq. 2.3})$$

where N is the number of nuclei produced per unit time and unit volume V , and A_k a composite term (generally around 10^{25}). So the nucleation rate can be written also as^[62]:

$$J = A_k \exp\left(\frac{-4\pi\gamma r^{*2}}{3kT} \right) \quad (\text{Eq. 2.4})$$

2.2.4 Heterogeneous nucleation

Nucleation in undercooled liquids frequently occurs on the container surface, foreign particles, or other heterogeneities that catalyze the nucleation by reducing the cluster interfacial energy.^[63]

The critical supersaturation and activation energy are considerably lower than for homogeneous nucleation,^[62] since a small number of atoms can cluster at a wetted surface to form a crystal cap (Figure 2.8). The curvature of the cap achieves a radius without the required large amount of clustered atoms for homogeneous nucleation. The thermodynamic energy barrier for the heterogeneous nucleation is smaller than for homogeneous nucleation and related to that as:^[64]

$$\Delta G_{het}^* = \Delta G_{hom}^* f(\theta) \quad (\text{Eq. 2.5})$$

where $f(\theta) = \frac{1}{4}(2 + \cos\theta)(1 - \cos\theta)^2$ and θ is the wetting angle.^[64,65]

For any wetting ($\theta \neq 180^\circ$) the nucleation barrier is decreased, resulting in an increased nucleation rate.^[59]

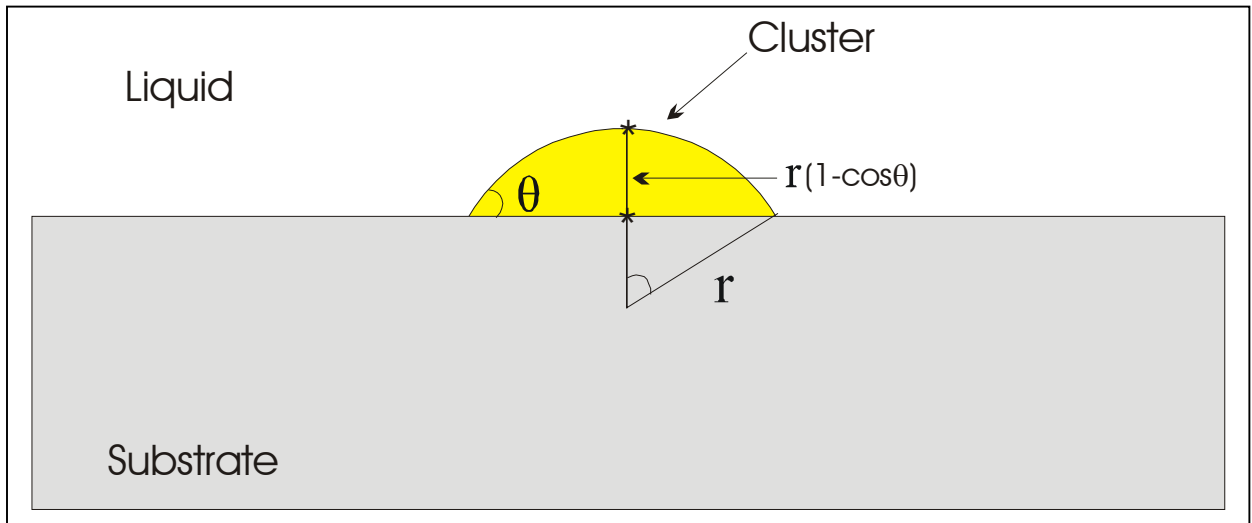


Figure 2.8. Formation of a cluster (radius r) in a substrate. Heterogeneous nucleation.

2.2.5 Crystal growth

The crystal growth is the step when the solutes present in the supersaturated solution feed the surface of the particles, leading to an increase of the crystal size.^[62] In other words the building units (atoms or molecules) become a part of the crystal when their chemical potential becomes equal to the chemical potential of the crystal.^[53]

A simple general model can be used to derive the crystal growth mechanism using an argument similar to those used for nucleation rate. The general equation for the crystal growth rate, U , is written as:

$$U = A' \left[1 - \exp\left(\frac{-\Delta G}{kT}\right) \right] \quad (\text{Eq. 2.6})$$

where ΔG is the bulk free energy change per unit mole and A' is a constant that inversely depends on viscosity. The temperature dependence of the crystal growth rate is very similar to that of the nucleation rate, the only difference is that crystal grows any temperature below the melting temperature as long as nuclei are available. If the viscosity is low, the growth rate will be determined by the thermodynamic values and tend to be large. As the temperature decreases, the viscosity increases rapidly, slowing and eventually halting the crystal growth.^[66]

2.2.6 Crystallization in confined systems

The physical properties of liquids in small droplets can be significantly different from those in bulk phase because small particles have high surface-to-volume ratios and the potential for surface effects to dominate over bulk.^[67] On the other hand, it has been known that a transformation from liquid oil to fat crystals remarkably influences the physical properties of the emulsions such as emulsion stability, rheology, appearance, etc.^[68] These physicochemical properties play an important role in the manufacture, storage, transport, and application of emulsions.^[69] Crystallization within micron-sized emulsions droplets has in addition critical implications in both biological and materials science research, such as the synthesis of nanosized particles for catalysis, semiconductors, opto-electronics and purification techniques. In spite of this wide

importance, crystallization in fluid nanostructures is just starting to be examined which we attribute to the accessibility of model systems.

2.2.6.1 Melting and Crystallization in Droplets

In several experimental studies on small nanoparticles or for material confined in small pores a decrease of the melting point was observed.^[70] Such shifts in melting temperature from the bulk transition can be understood on the basis of classical thermodynamical arguments by balancing the bulk and interfacial contributions to the free energy of the solid and liquid phases. From the Gibbs-Thomson equation:

$$\Delta T_m = T_{mb} - T_m = 2T_{mb}\gamma_{sl}v_l / \Delta_{sl}H \quad (\text{Eq. 2.7})$$

where T_{mb} and T_m represents the bulk and the droplet transition temperature, γ_{sl} the interfacial tension, v_l the molar volume of the liquid and $\Delta_{sl}H$ the molar enthalpy of melting, a linear dependence of ΔT_m on the inverse droplet size is predicted. As a second possibility, additional additives within the particles can also lower the melting point.

The crystallization in emulsions with larger droplets has been studied extensively, and a theoretical analysis of the crystallization kinetics is now well established.^[59,71-73] Recent studies focused on the use of such systems to modify crystallization in order to obtain favorable crystalline forms.^[74] Different to a bulk system, in emulsions one has to create a large ensemble of independent nucleation sites, and after nucleation, the crystal growth is governed and limited by the size of the droplet and is stopped when reaching the droplet border.

The nucleation can be either homogeneous if the droplet is an ideally pure liquid, e.g. without any added components (nanoparticles or foreign molecules), or heterogeneous if added components are present, which behave as nucleating sites. It is known that homogeneous nucleation occurs at lower temperatures than heterogeneous nucleation.^[75]

It is well known that emulsification tends to increase the undercooling required for crystallization over that of bulk liquids. A lowering of the crystallization temperature, i.e. the temperature where in a defined kinetic protocol crystallization occurs, is reported by McClements et al.^[76] and Kaneko et al.^[68] In their opinion, the reason for the shifting in

the crystallization temperature could be associated to the number of foreign crystallization nuclei which usually cause heterogeneous nucleation in the bulk phase and are now distributed amongst a large number of isolated droplets. So, only a small number of droplets contain now such a foreign element for heterogeneous crystallization, and therefore the probability for heterogeneous nucleation for all the droplets is drastically reduced.^[77]

The effect of added components or surfactant molecules on the nucleation in emulsion studies is not obvious. Clearly, one possible role is to act as heterogeneous nucleation sites, and Turnbull^[78] and Perepezko^[79] have discussed this. For example, in mercury, Turnbull^[72] showed that changes in the surfactant could increase the undercooling from 5 °C to 60 °C, but the melting was similarly influenced.

The nucleation rate is strongly temperature dependent; for example, in *n*-alkanes, the nucleation rate can change by a factor of 5000 per °C. The size of the emulsion droplets also plays a key role in nucleation studies. In homogeneous nucleation, the nucleation rate is proportional to the volume of the droplets. Typically, the determination of the size distribution for the emulsions is a large source of errors in nucleation rate measurements. Few groups have studied the alkane nucleation through the use of emulsion samples. The earliest work is from Turnbull and Cormia^[72,73] who studied C-16, C-17, C-18, C-24, and C-32 alkanes. They noted that there seemed to be an unusual spread in the melting temperatures, and a second anomaly observed in those study is the reduced undercooling. The reduced undercooling is defined as $\Delta T = (T_m - T_n) / T_n$ where T_n is the point where the nucleation rate becomes significant in the emulsion samples and T_m is the thermodynamic melting temperature. Other groups^[80] studying nucleation in emulsions focused on the behavior of C-16 using ultrasound transmission to measure the proportion of the liquid to solid in an emulsion sample. Their results exhibit the typical 14 – 15 °C undercooling as also found by other workers. The nucleation of alkanes in emulsions was recently review by Herhold et al.^[81]

2.2.6.2 Crystallization kinetics in droplets

Turnbull and co-workers provide comprehensive details on the crystallization kinetics of liquid metals and alkane liquids.^[72,73,82] In general, nucleation rates in emulsified samples

can be determined by measuring the volume fraction of the solid (ϕ) as a function of time (t). The crystallization rate will be proportional to the volume fraction of droplets that contain no crystals ($1-\phi$) and therefore decreases with time:

$$\frac{\partial\phi}{\partial t} = k(1-\phi) \quad (\text{Eq. 2.8})$$

For homogeneous volume nucleation, the rate constant k is proportional to the droplet volume. If nucleation proceeds at the droplet surface, the rate constant k is proportional to the droplet surface. Solving Eq. 2.8 leads to the following expression that gives the volume fraction of solidified droplets as a function of time:

$$\begin{aligned} \phi &= 1 - \exp(-kt) \\ \text{or} \\ \ln(1-\phi) &= -kt \end{aligned} \quad (\text{Eq. 2.9})$$

That way, the values of rate constant k can be calculated.

2.2.7 Metastable phases in alkanes

The crystallization of alkanes has been strongly studied because they have very important industrial applications, such as processing of oils, fats, and surfactant.^[83] Looking at the different n -alkane chain lengths, there is an unusual behavior of the crystallizing or melting for even and odd alkane chains, which is called the even-odd effect.

As early as in 1877, Baeyer already stated that the melting point of the fatty acids with even numbers of carbon atoms is relatively higher than those with odd numbers.^[84] Although the phenomenon of the even/odd alternation has been known for a very long time, there does not exist a plausible explanation pattern yet.^[85]

The even-odd effect is observed for the melting-crystallization as well as for the metastable phases, that can be detected few degrees before the melting. In 1932, Müller^[86] had shown by X-ray the existence of an intermediate phase where the molecular chains were in a state of more or less free rotation about their axes (the so-

called rotator phase), between the crystalline and the liquid phase for some paraffins. He described the rotator phase as a layered structure in which each layer is formed by the hexagonal packing of the aliphatic chains with their long axes perpendicular to the layer planes. After that first observation of the rotator phase, other works have been published in order to better understand those metastable phases.^[87-89]

While the structure of the crystalline phase of n -alkanes is characterized by a compact stacking of chain molecules, the long molecular axes being perpendicular to the stacking planes in odd-numbered and tilted in even-numbered compounds,^[90] the rotator phases are lamellar crystals which lack long-range order in the rotational degree of freedom of the molecules about their long axes.^[91] There are five rotator phases reported.^[88,89,92] They differ in their symmetries, in-plane molecular packing, layering sequences, and the amount of molecular tilt with respect to the layer spacing.^[93] In general words, the stable phase for n -alkanes are triclinic for $12 \leq n$ (even) ≤ 26 ^[83], orthorhombic for $9 \leq n$ (odd) ≤ 35 ^[94] and monoclinic for $28 \leq n$ (even) ≤ 36 ,^[83] while the rotator phase for n (odd) ≤ 23 is orthorhombic and hexagonal for n (even) ≤ 24 .^[89]

Those transition phases, once formed, may persist indefinitely, and have strong role in the crystallization process and crystal morphology.^[95]

It is well known that the melting temperatures and rotator transition phase temperatures increase with increasing alkane chain length.^[96] However, the difference between the melting temperature and the rotator equilibrium transition temperature in bulk systems is roughly constant as a function of chain length.^[97]

2.3 Bioengineered, biomimetics and self-assembling materials

Nature after had been source of inspiration for artists, musicians and architectures; has started to inspire the scientists, who wanted to understand the secrets of such advanced properties and hierarchy, which are based in self-assembly organization. The search for new materials with astonishing properties has brought the scientists and engineers to try to mimic the properties of natural structures such as skin, bones, silk of spider, and so on. Among many natural structures, with important and amazing properties, one can cite polymers and nanocrystalline inorganic particles.

Many biological organisms are able to synthesize inorganic particles and seem to be able to create an interaction with the nanoparticles in order to “use” them.^[98] Some bacteria, for example, *Gallionella* and *Leptothrix* produce iron-rich nanoparticles, which show an important crystallographic orientation.^[99] Others bacteria have developed nanoparticles for practical purpose, e.g. magnetotactic bacteria synthesize ribbons of elongated magnetic (Fe_3O_4) and greigite (Fe_3S_4) particles, which act as a compass under the influence of magnetic fields.^[100] Even more complex organisms such as ants,^[101] honeybees^[102] and trouts^[103] also synthesize nanoparticles and use them in connection with earth’s magnetic field for homing and navigation.

From the combination of nanocrystals and polymers one can form very strong structures, such as bones, which are formed via the biomineralization of hydroxyapatite in a matrix of collagen fibers.

The formation of the biomineral phase is almost always carefully and exquisitely orchestrated by complex spectrum of the organic matrix of the biopolymer.

Natural polymers have been used as biomaterials for many applications such as sutures, blood vessels replacement, and many other biomedical and pharmaceutical applications. Amongst those polymers, gelatin has become one of the most popular.

For the production of bioinspired materials, the use of emulsions is regarded as a very promising approach for the preparation of biomineralized exquisite architectures.^[104]

2.3.1 Gelatin nanoparticles

Gelatin is a hydrophilic polymer^[105] obtained by a controlled hydrolysis of the fibrous insoluble protein collagen, which is widely found in nature and is the major constituent of skin, bones and connective tissue^[106]. Being a protein, gelatin is composed of a unique sequence of amino acids such as glycine, proline and hydroxyproline.^[107]

In aqueous solution, gelatin forms physical thermo-reversible gels upon lowering the temperature below 35 °C as the chains undergo a conformational coil-to-helix transition during which they tend to recover the collagen triple-helix structure.^[108] Due to the ability to form thermo-reversible gels, it has been used along the years in many industrial applications, such as gelling agent, thickener, film former, protective colloid, adhesive agent, stabilizer, emulsifier, foaming/whipping agent, beverage fining agent, etc. Very

significant application of gelatin is found in the field of medicine and pharmacy. It is used for many biomedical applications, such as sealant for vascular prostheses,^[109] wound dressing and adsorbent pad for surgical use^[107,110].

Especially gelatin microspheres have been widely investigated for controlled drug release^[111]. The main characteristics of gelatin that suggest its use in the field of drug delivery are the biocompatibility and the degradation to non-toxic and readily excreted products^[112]. The production of gelatin particles in water is not an easy task since the hydrophilic gelatin dissolves in hot water. So, in order to produce gelatin nanoparticles in water (microgels), the gelatin chains have to be cross-linked to keep the structure of nanoparticles. In principle, many compounds have been used to promote chemical cross-linking, such as formaldehyde^[113], glutaraldehyde^[114], water-soluble carbodiimide,^[115] diepoxy compounds,^[116] or diisocyanates.^[117] Physical cross-linking by thermal heating and ultraviolet irradiation^[118] of gelatin has been also reported.

It was found that nano- and microparticles, prepared by means of different processes and hardened by a suitable cross-linking agent as glutaraldehyde, enhance tumoral cell phagocytosis^[119].

For a cross-linking of gelatin chains to form nanoparticles, a template system has to be chosen which keeps the particular structure. Therefore, in order to obtain stable gelatin particles in water, it seems to be highly favorable to first prepare gelatin particles containing chemically non-cross-linked gelatin in an inverse emulsion process and chemically cross-link the particles in that state to fix the particles. Then the cross-linked particles can be transferred to the water phase where they are expected to behave as microgels, and they do not dissolve at low (due to physical cross-linking) and at high temperature (due to chemical cross-linking). The very suitable approach to obtain small, homogeneously distributed and stable gelatin particles in oil is to use the miniemulsion process.

2.3.2 Hydroxyapatite (HAP)

Organic supramolecular assemblies are abundant in biological systems, for example in double and triple helices, multisubunit proteins, membrane-bound reaction centres,

vesicles, tubulus and so on, some of which (collagen, cellulose and chitin) extend to microscopic dimensions in the form of hierarchical structures.^[120,121]

Among many natural supramolecular structures, bone has become to one of the largest source of inspiration and studies. In spite of been formed from biocompatible materials such as calcium phosphate and proteins, it forms very durable structures.

Bone is regarded as a natural composite or hybrid material of inorganic crystals embedded in a collagen matrix. The hierarchical structure of bone is based on the nucleation of calcium phosphate (nanocrystals of hydroxyapatite (HAP): $\text{Ca}_5\text{OH}(\text{PO}_4)_3$) in nanoscale spaces organized within the supramolecular assembly of collagen fibrils.^[121,122]

Due to the embedding of inorganic crystals in a collagen matrix, bones are regarded as natural composite or hybrid material.

Hybrid materials as inorganic-organic composite can have very superior properties, the teeth therefore are good examples, which are known to be the hardest calcium-phosphate based biomineral, which show a very high elastic modulus of 131 Gpa^[123]. This is directly associated with hierarchical structure and the complex association of minute apatite crystals together with protein molecules. The strength of the HAP/collagen bonding and the quality/maturity of the collagen fibers are important for the mechanical behavior of bone.^[124]

Hydroxyapatite has been intensively investigated to develop suitable bone substitutes and many studies have been done to give the biocompatible, bioactive, biodegradable and osteoconductive properties of natural bone.^[125] Therefore the HAP is the most important constituent of the so-called bioactive ceramics, which can bind to living bones and undergo the proliferation of osteoblasts on it.^[126,127]

The system apatite-gelatin is also regarded as a simplified model for teeth formation because of its close chemical correspondence and remarkable analogy to structural aspects of dentine and enamel composites.^[128]

2.4 Semiconducting polymers

2.4.1 Principles of semiconducting polymer

Most of the polymers and organic solids are insulators because the sp^3 hybridized orbitals form sigma (σ) bonds where the electrons are highly localized. However conjugated molecules can be semiconductors, since p orbitals form more delocalizable π bonds. Therefore, the energy gap for a π bond (1 – 3 eV) is much smaller than for a σ bond (6 – 12 eV). In most cases, conjugated polymers are characterized by a regular alternation of single and double carbon-carbon bonds in the polymer backbone, the latter giving rise to delocalized π -molecular orbitals along the polymer chain. Due to the orbital overlap, the π -electrons are delocalized within molecules and the energy gap between the highest occupied molecular orbital (HOMO) and the lowest unoccupied molecular orbital (LUMO) is relatively small,^[129] therefore the orbitals can be thought of a “cloud” that extends along the entire conjugated chains. In this cloud the electrons are free to move along the molecules. Therefore, even though the charge density in pure undoped organic is very low, injected electrons and holes can be well transported through the conjugated materials.^[130] In the last few years, conjugated polymers started to become, a reasonable competitor for the silicon technology that still dominates the electronic devices world. The semiconducting polymers have several advantages. They show higher flexibility, are easier to manufacture and are potentially inexpensive. Conjugated polymers can be used in a large range of applications, e.g. light emitting diodes, field effect transistors, organic wires, solar cells, in non-linear optics and photoconductivity.

2.4.1.1 Example of conjugated polymers

The field of π -conjugated polymers was initiated by the discovery in 1977 when freestanding thin films of polyacetylene could be doped to obtain high electrical conductivity.^[131] Since then many new polymer systems have emerged and the main interest in these new polymer systems has then shifted to their semiconducting properties. Among those polymers we can mention, poly(*p*-phenylenevinylene) (PPV) and related polymers of which the films provide at relatively high quantum for electroluminescence (EL) or photoluminescence (PL) in the yellow/green portion of the visible spectrum.^[132] As derivatives of PPV poly(2-methoxy-5-(2'-ethyl-hexoxy)-1,4-phenylenevinylene)

(MEH-PPV),^[133] and a cyano-substituted PPV (CN-PPV),^[134] were used, both with emission more or less in the red/orange part of the spectrum.^[135] Moreover, Me-LPPP is a solution processable poly(*para*-phenylene)-type ladder polymer which has been widely used as active semiconducting material in electronic devices (light emitting diodes LEDs, solid state lasers, photodiodes)^[136,137] emitting in the blue region. Polyfluorene (PF) derivatives are characterized by a unique combination of semiconducting and liquid crystalline (LC) properties, the latter entails low viscosity in the LC-state and the tendency to align with their long axis along a preferred direction, which is known as director; PFs have been applied as high performance blue emitters in LEDs based on organic semiconducting polymers.^[138] Polycyclopentadithiophenes (PCPDT) as heteroaromatic PF analogues are characterized by a reduced band gap (HOMO/LUMO) energy in relation to PF, and are promising materials for a potential use in organic materials based field effect transistors (FETs) and solar cells.^[139]

2.4.2 Semiconducting polymer layers

Solid layers of conjugated polymers have been successfully included as active layers into various electrical and electrooptical devices such as light-emitting diodes (LEDs),^[140] solar cells^[141] and field-effect transistors (FETs).^[142] In the majority of cases, these layers have been deposited from solutions of the polymers in organic solvents. However, deposition from those solvents brings about several problems, particular when dealing with large area or multilayer devices. For example, large area light-emitting diodes or large area photodiodes require uniform coverage of large surface areas. Ink-jet printing or screen printing offer the ability to deposit pattern of the active species in a well-controlled fashion on large substrates. In the last years, ink-jet printing^[143] as well as well as screen-printing^[144] has been reported for the fabrication of organic light-emitting diodes and high-performance plastic transistors. While in most of these cases printing has been performed from solutions of the active components in organic solvents such as chloroform, the deposition from aqueous or liquid components would be most desirable. One major problem in constructing multilayer assemblies with polymers is that most polymers used as charge transport, emission layers or gate dielectric are soluble in the same organic solvents, and coating of several layers on top of each other will lead to

interdiffusion and undefined interfaces. One major approach used to avoid interdiffusion is to deposit a first layer from a common solvent and then to either cross-link (by thermal treatment or illumination with light) or chemically convert the polymer, resulting in an insoluble layer, which can subsequently be overcoated by the next layer.^[145] However, these processes often go along with chemical reactions, and reaction side products might affect device performance. Recently, polymeric conductors such as polyethylenedioxythiophene (PEDOT) doped with poly(styrene sulfonate) (PSS) have been deposited from water-based dispersions,^[146] but this approach is focused on the deposition of electrically conducting polyelectrolytes (PEDOT, or polyaniline (PANI)). In order to obtain polymer dispersions, one can start from a miniemulsion where the monomer droplets are polymerized to give polymer particles without changing the droplet identity. Another possibility is the formation of artificial latexes from the droplets consisting of a solution of the preformed polymer (see section 2.1.3). After evaporation of the solvent, polymer dispersion is obtained. Therefore the combination of the artificial latex concept with the miniemulsion approach seems to be the most efficient way for the case of semiconducting polymers, since by this approach products of high purity with very small and narrow distributed particles are easily obtained, what is essential for the application on the manufacture of electronic devices.

2.4.3 Polymer mixtures

Solid blends of polymers can exhibit mechanical, optical and electro-optical properties not attainable with single polymer components. Several of these applications require the blend morphology to be on sub-micrometer scales. Moreover, most biological, optical and electro-optical applications request thin layers of the blends, which are mostly deposited from solution. For example, highly efficient organic solar cells have been constructed from thin layers containing a blend of an electron donating and an electron-accepting polymer.^[141,147] In this case, the dimensions of phase separation must be comparable to the exciton diffusion length, which is in the range of few tens of nanometers, while the overall layer thickness should not largely exceed the penetration depth of light.

However, since the entropy of mixing of polymers is low, solid polymer blends tend to phase separate on the macroscopic scale in order to minimize the total interfacial area. Moreover, when a thin layer of immiscible polymers is deposited from solution, the morphology depends strongly on various parameters such as the difference in solubility of the polymers in the common solvent, the interaction with the substrate surface, the layer thickness as well as how the layers are deposited, dried and annealed.^[148] Therefore, the adjustment of a certain length scale of phase separation in a thin layer is mostly based on trial-and-error.

Several strategies have therefore been developed to form well-defined and predictable multicomponent polymer structures at nanometer scales. The most straightforward approach is to use linear block-copolymers.^[149] The drawback of this approach is, however, that two immiscible polymers, which differ in their chemical and electronic structure, have to be linked covalently, which limits the selection of possible A-B pairs. In fact, only few examples of block-copolymers containing two semiconducting polymers have been reported.^[150] Also, A-B blockcopolymers are used as compatibilizers in bulk blends of the corresponding homopolymers A and B.^[151] Very recently, co-continuous nanostructured polymer morphologies were prepared via reactive blending.^[152] In this approach, one component bears reactive groups along the backbone while the second component possesses complementary reactive moieties at one end, only. Even though this novel strategy is expected to be versatile, it needs yet to be proven that it is applicable to a wide range of polymers, including conductive or fluorescent materials and that it can be applied to thin layers.

Once again, the preparation of artificial latex via miniemulsion, already mentioned, seems to be a more practical method to prepare blends of polymers, in which the lateral dimension of phase separation in thin layers is precisely controlled by the diameter of the nanoparticles.

Homogeneous films made by polymer blends, free of big domains, can be obtained by the combination of different polymeric dispersions where the diameter of the particles determines the phase separation dimension, providing so an extraordinary mode of phase separation control in the nanometer scale. Moreover, this procedure can be used to combine two different polymers within the same particle, obtaining so even a smaller

phase separation, e.g. maximization of the interfacial area, what leads to higher efficiency.

3. Relevant methods for characterization

3.1 X-ray Diffraction

X-rays were discovered by W. C. Röntgen in 1895 and can be defined as relatively short-wavelength, high-energy beams of electromagnetic radiation.^[153] They are produced by bombarding a metal with high-energy electrons and can be diffracted when passing through a crystal as first suggested by von Laue in 1912.^[154] X-ray diffraction depends on the angle of the incident beam, as shown in Eq. 3.1. The planes in a crystal are separated by distance d . The incident beam meets the plane at angle θ . So the total deflection is 2θ . Therefore the lower beam travels an additional distance $d\sin\theta$ after reflection. This observation was described in the Bragg equation:

$$n\lambda = 2d\sin\theta \quad (\text{Eq. 3.1})$$

Where λ is the wavelength of the incident X-ray (in the range between 0.001 and 50 Å), d is the interplanar spacing of the crystal, and n is an integer ($n = 1, 2, \dots$)

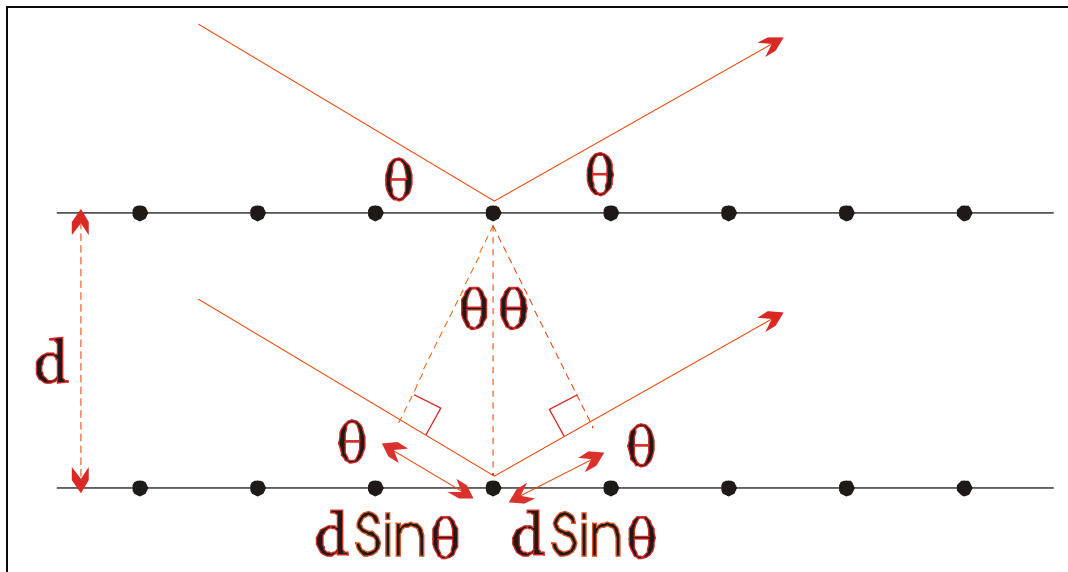


Figure 3.1. Graphical description of the principle of X-ray diffraction.

Analysis of X-ray diffraction data gives numerical values of two important parameters, the interplanar spacing and the intensity of diffraction. The interplanar spacing is characteristic of the pattern of the crystal from which the packing of the repeating units

can be determined, while the intensities of a certain number of diffractions can provide information on the structure of a crystal. The structure of a crystal is the symmetrical arrangement of one or more species of atoms in three directions at certain angles, including right angles.^[155] For the past several decades X-ray studies have provided a genuine elegance to macromolecular chemistry. Investigations have relied much on X-ray crystallography to develop a sense of how synthetic and biological polymers are shaped. Although the oldest and most popular kind of X-ray radiation is the X-ray radiography, what is largely used in medicine, the structure analysis of crystals is studied by X-ray crystallography, of which X-ray powder diffractometry is one important member. For the investigation of compounds by their diffraction patterns there are two methods, the wide-angle X-ray scattering (WAXS) and the small-angle X-ray scattering (SAXS) method. WAXS is used for the determination of crystalline structures on the atomic length scale ($\sim 1 \text{ \AA}$). This technique measures the intensity of scattered light in the range of 5 to 180° . SAXS on the other hand is used for the determination of ordered colloidal systems with characteristic length scales that range from 1 nm to several hundred nanometers. This technique measures the intensity in the range of 0 to 5° .

3.1.1 Determination of crystallite sizes

The broadening and the shape of the diffraction peaks are determined by several parameters such as experimental set up, defects and the finite sizes of the crystal and can give characteristic information on the sample. Neglecting defects, the size of the crystallites can be determined using the Scherrer equation:^[156]

$$\tau = K\lambda/(\beta \cdot \cos\theta) \quad (\text{Eq. 3.2})$$

where β is the line broadening due to the effect of small crystallites.

β is given by $\beta = (B-b)$, B being the width of the observed diffraction line at this half-intensity maximum, and b the instrumental broadening or width of a peak from a specimen that exhibits no broadening beyond inherent instrumental peak width. K is the so-called shape factor, which usually takes a value of about 0.9 .^[157]

3.2 Dynamic Light Scattering (DLS)

One of the most popular methods in colloid and polymer analysis is the so-called dynamic light scattering (DLS) or quasi-elastic light scattering. This technique enables the determination of particles sizes and their size distribution in dispersion in a range of 1 – 2000 nm. The method of DLS is based on the survey of the Brownian motion of small particles in diluted solutions.

When a laser irradiates dispersions, the particles (colloidal particles or micelles) become scattering centers, scattering the light in all directions. By constructive and destructive interferences of the emitted secondary waves, characteristics patterns of the light are built, and together with the relative movement of the particles, one originates a fluctuating interferograms. The principle of DLS is based on the Doppler-effect. The frequency of a moving source will be displaced to higher or lower frequencies if it moves away or closer to the receptor. As a result of the Doppler-effect the frequency of the emitted irradiation is displaced, whereas the absolute value of the displacement depends on the speed of the particles. Dispersed particles move under the Brownian motion, thus they have a velocity distribution, which results in a symmetric broadening of the scattered light.

The full width at half maximum Γ of the spectral distribution of light scattering is proportional to the translatorial diffusion coefficient D .

As the colloidal movement of the particle, which takes place in solution, is very slow, the frequency displacement is also extremely small and cannot be observed directly in this frequency range. The spectral broadening of the scattered light cannot be solved experimentally. The scattered light contained all information about the diffusion movement of the particles enabling the determination of the size of the particle. The Wiener-Knintschin Theorem provides a solution for the problem. It says that for an intensity distribution $I(\omega)$ in the real frequency scale exists a fourier-transformation function $g(t)$ (time or autocorrelation function) in the reciprocal time scale:

$$I(\omega) = \frac{1}{2\pi} \int_{-\infty}^{+\infty} g(t) e^{i\omega t} dt \quad (\text{Eq. 3.3})$$

$$g(t) = \int_{-\infty}^{+\infty} I(\omega) e^{-i\omega t} d\omega \quad (\text{Eq. 3.4})$$

with time t and frequency ω .

The more narrow the frequency broadening in the real scale, the wider is the distribution in the reciprocal time scale. The small frequency broadening in the real scale introduces a measurable relaxation in the reciprocal scale. Since the temporal fluctuation of the scattered light intensity $I(t)$ is measured, the determination of the autocorrelation function of the scattered light intensity $g_I(q,t)$, is defined as:

$$g_I(q,t) = \frac{\langle I(q,t_0) \cdot I(q,t) \rangle}{\langle I(t_0) \rangle^2} = \lim_{t \rightarrow \infty} \frac{1}{T} \int_0^T I(t) I(t+t') dt \quad (\text{Eq. 3.5})$$

From this equation it results a correlation function, which mirrors the relationship between the average intensity for the time $(t+t')$ and the intensity $I(t)$. $I(t)$ and $I(t+t')$ are independent of each other for big values of t . For small values, the correlation function g_I corresponds to the squared averaged scattered intensity $\langle I^2 \rangle$. The autocorrelation function $g_I(q,t)$ is connected with $g(q,t)$ by the Siegert-relation:

$$g_I(q,t) = 1 + |g(q,t)|^2 \quad (\text{Eq. 3.6})$$

For monodisperse, spherical particles without interparticle interaction that means high dilution, $g(t)$ is expressed by a simple exponential function, of which the characteristic time constant is related to the diffusion coefficient D :

$$g(q,t) = A e^{-q^2 D t} \quad (\text{Eq. 3.7})$$

Using the Stokes-Einstein relation one can calculate a hydrodynamic averaged intensity radius from the diffusion coefficient D :

$$R_H = \frac{k_B T}{6 \pi \eta_0 D} \quad (\text{Eq. 3.8})$$

Where η_0 is the viscosity of the medium, k_B the Boltzmann constant and T the absolute temperature. This relation is the basis of the particle size determination by dynamic light scattering, but it is valid only for spherical monodisperse particles.

For polydisperse particles, it is necessary to do a cumulant analysis. The correlation function is then represented by:

$$\ln g(q,t) = \sum_{n=0}^{\infty} \frac{(-1)^n \Gamma_n t^n}{n!} \quad (\text{Eq. 3.9})$$

The determination of the cumulant Γ_n is done by the extrapolation of the initial slope of the plot of $\ln g(q,t)$ versus t :

$$\Gamma_n = \left(\frac{\partial^n \ln g(q,t)}{\partial t^n} \right)_{t \rightarrow 0} \quad (\text{Eq. 3.10})$$

The cumulants are related to the diffusion coefficient D through the scattering vector q :

$$D = \frac{\Gamma_1}{q^2} \quad (\text{Eq. 3.11})$$

The polydispersity of a sample can be determined through the fitting of the cumulant analysis in a gaussian distribution of the intensity weighted diffusion coefficient. By the quotient of the first and second cumulants, one can obtain the variance μ of the gaussian distribution, which represents a square standard deviation σ .

The relation between the best fitting of the logarithmic correlation function and the width of a gaussian distribution is then established by:

$$\mu = \frac{\Delta D}{D} = \frac{\Gamma_2^2}{\Gamma_1} = \sigma^2 \quad (\text{Eq. 3.12})$$

3.3 Atomic Force Microscopy (AFM)

The atomic force microscope was invented in 1986 by Binnig and enables the detection of atomic-scale features of insulating surfaces^[158] and it overcomes limitations of the scanning tunneling microscope (STM), which can be used only for the investigation of conducting or semiconducting materials, since a tunneling current is employed.

In atomic force microscopy (AFM) the repulsive force between the tip (located at the end of a cantilever) and sample is usually measured on the basis of the cantilever deflection. In general, the AFM enables one to detect surface morphology, nanoscale structures, molecular and atomic-scale lattices.^[159]

The spring in the atomic force microscope is a critical component. We need the maximum deflection for a given force. This requires a spring that is as soft as possible. At the same time a stiff spring with high resonant frequency is necessary in order to minimize the sensitivity to vibrational noise from the building near 100 Hz. The resonant frequency, f_0 , of the spring is given by:

$$f_0 = \left(\frac{1}{2\pi} \right) \sqrt{\frac{k}{m_0}} \quad (\text{Eq. 3.13})$$

where k is the spring constant and m_0 is the effective mass that loads the spring. As we decrease k to soften the spring we must also decrease m_0 to keep the ratio k/m_0 large.^[158] The spring constant k of a rectangular cantilever is expressed as:^[160]

$$k = \frac{Et^3w}{4L^3} \quad (\text{Eq. 3.14})$$

where E is the elasticity modulus and w , L , and t are the width, length and thickness of the cantilever, respectively.

The Figure 3.2 shows the principle of AFM measurement. The deflection of the cantilever causes a twofold larger angular deflection of the laser beam. The reflected laser beam strikes a position-sensitive photodetector consisting of two side-by-side photodiodes. The difference between the two-photodiode signals indicates the position of the laser spot on the detector and thus the angular deflection of the cantilever. The piezo-scanner is used to position the tip or the sample.

The two most used modes in AFM are the contact-mode and the tapping mode.

Contact-mode AFM was originally introduced for high-resolution surface profiling. With the progress in AFM applications, it became clear that for many materials this objective can be achieved only by minimizing tip-sample force interactions, because it may modify the topography of a sample surface. In addition, it was also realized that these interactions can be utilized to determine mechanical properties of surfaces such as indentation, adhesion and friction. For example, the tip may cause elastic or inelastic surface deformations,^[161] which can be recognized from the images obtained with high forces. In imaging with low forces, the influence of the weak surface forces (e.g., van der Waals, hydrophobic, and electrostatic interactions) on the cantilever movement becomes significant. It is a challenging task to deconvolute the contributions of these forces to the image contrast. Important information about the tip-sample force interaction can be obtained by analyzing the force-vs-distance curves.^[159]

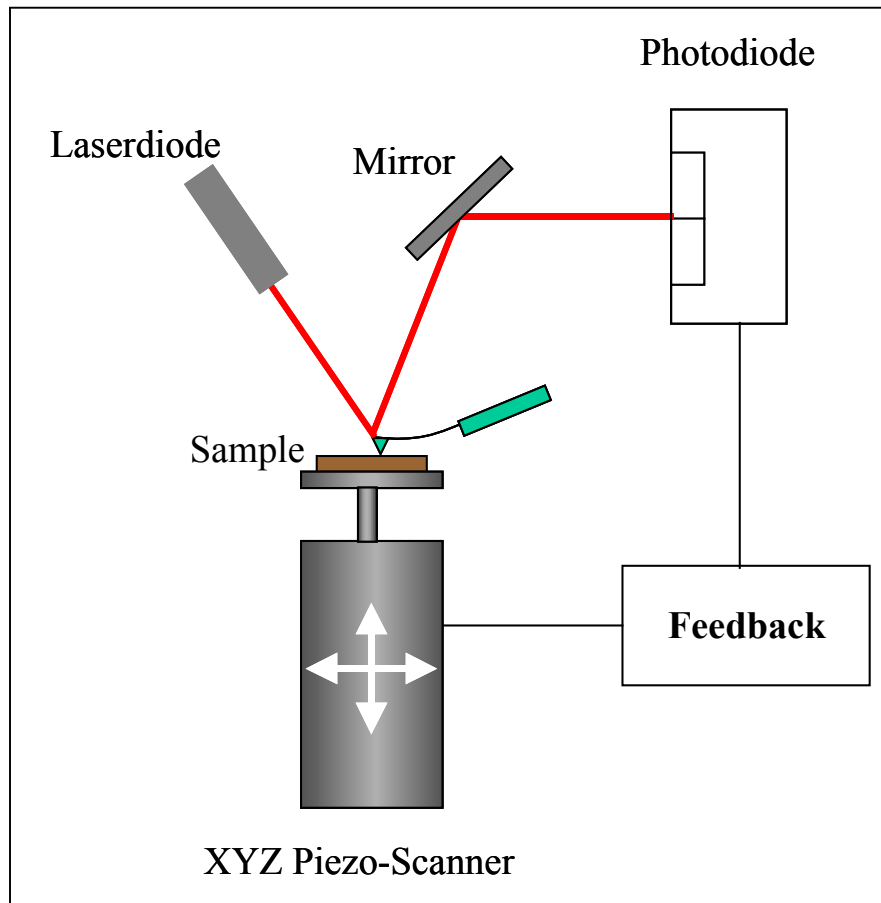


Figure 3.2. Principle of atomic force microscopy measurement.

Among the different modes used in AFM, the tapping mode is the most used in polymer science and biological samples. In this mode the tip is vertically oscillated at its resonance frequency. When the sample approaches the vibration tip, they come into intermittent contact (“tapping”), thereby lowering the vibrational amplitude. The amplitude drop is used for the feedback. In this mode, the tip-sample lateral force is greatly reduced and the short tip-sample contact time prevents inelastic surface modification. As expected, a comparison of the imaging in the contact and tapping modes shows that soft surfaces are less modified in the tapping mode.^[162]

The tapping mode was originally introduced for ambient-condition experiments. For the tip to “penetrate” through the contamination overlayer, application of rigid cantilevers

(resonance frequencies in the 300-400 kHz range) and high operating amplitudes (10-100 nm) is required. In the tapping mode, the energy delivered to the sample from the vibration tip is determined by the amplitude of the free vibration (A_0) and the set-point drop (ΔA) in the amplitude. For high-resolution imaging and studies of soft materials, small values should be chosen for the A_0 and ΔA parameters. In ambient conditions, the reduction of these parameters is limited because of the contamination overlayer. Under liquid, however, one can operate the tapping mode with much smaller A_0 and ΔA values.^[159]

3.4 Differential Scanning Calorimetry (DSC)

One of the most popular techniques applied in polymer science and colloids is the differential scanning calorimetry (DSC). Since DSC monitors the heat adsorbed versus temperature, it measures the heat uptake. With DSC one can measure from helix-coil transitions in DNA, protein denaturation to crystallization, melting or decomposition reactions.

In practical words a DSC device consists of two separated heaters (Fig. 3.3). On the first heater is placed a pan (usually an aluminum pan) with the sample, in the second heater a pan with a reference material, or just an empty pan.

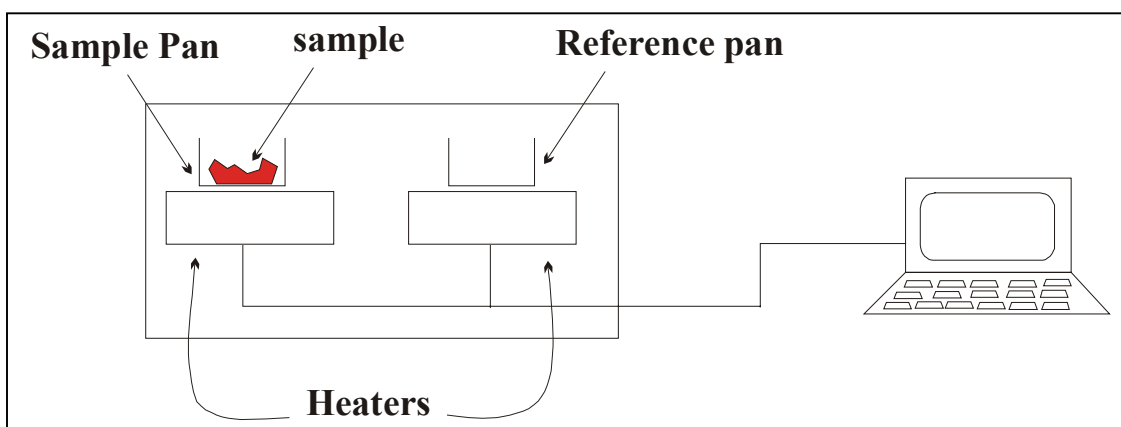


Figure 3.3. Basic principle of a DSC device.

The two pans must be heated at a specific rate, what has to be exactly the same for the two pans throughout the experiment, e.g. the temperature difference between the sample

pan and the reference has to be nearly zero. Since an extra material is present in one of the pans, it is necessary that the heater underneath the pan with the sample “work harder” than the one under the reference pan to keep the temperature of the sample pan increasing at the same rate as the reference.

Thus, from a DSC measurement one can plot the difference in the heat output of the two heaters against the temperature, either in the heating or in the cooling. From a DSC plot one can obtain information from the sample, such as heat capacity, latent heat, melting, crystallization temperature, etc.

For applications mainly the change of enthalpy ΔH between two states is relevant.

$$\Delta H = \int c_p \cdot dT \quad (\text{Eq. 3.15})$$

Changes that cause an increase of enthalpy (melting, evaporation, etc) are called endotherms; changes that lower the enthalpy such as crystallization, hardening, and degradation are called exotherms.

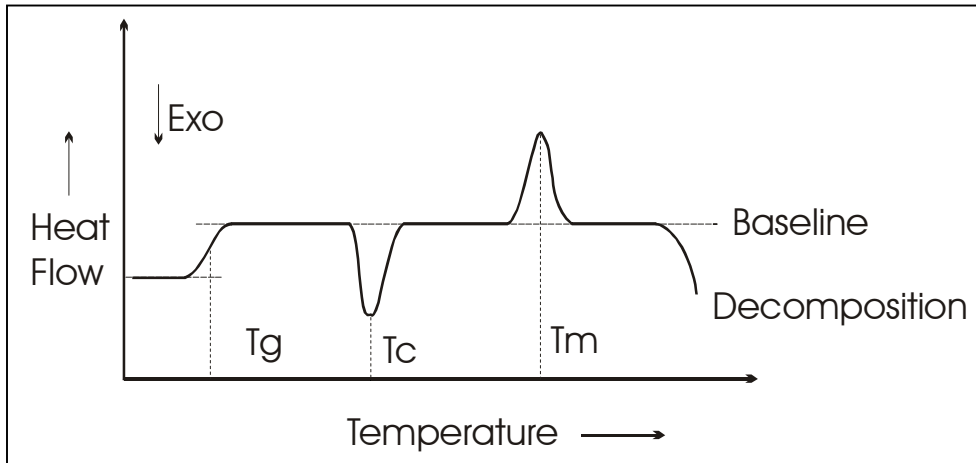


Figure 3.4. Typical DSC curve for a polymer: T_g - glass transition, T_c - crystallization temperature, T_m - Melting temperature and the decomposition of the polymer.

The specific heat capacity, C_p , is a measure for the energy required in order to heat one gram of a substance by 1 °C at constant pressure. In differential scanning calorimetry the

heat flow \dot{Q} that measures the heat per time and mass is measured. The heat flow is

directly proportional to the heat capacity C_p the factor of proportionality is the heating (or cooling) rate, v :

$$\frac{\dot{Q}}{m} = v \cdot c_p \quad (\text{Eq. 3.16})$$

Using this equation, the relationship between the most important parameters – heating rate and mass- is obtained.

The heating or cooling rate is a very important factor, since the exact temperature where each phenomenon happens is dependent on that. It means that the melting or crystallization temperature for a sample will slightly vary for different heating or cooling rates.

4 Results and discussion

4.1 Crystallization in miniemulsion droplets^[163]

The crystallization phenomenon plays a very important role in both science and technology. As already stated the physical properties of liquids in small droplets can be significantly different from those in bulk phase. Thus the aim of this section is to investigate the influence of liquids confined in nanodroplets on the crystallization behavior. In order to have narrowly size distributed droplets were used for the experiment direct (hexadecane in water) and inverse (water in oil) miniemulsions. The strong undercooling underwent by the droplets is studied in details, taking into account variables such as particle size, interfacial tension, etc. The evidence of a changing in the crystallization mechanism from heterogeneous to homogeneous due to size effect is supported.

4.1.1 Direct Miniemulsion Systems

In a first set of experiments, direct miniemulsions were prepared consisting of hexadecane as dispersed phase, perfluorohexane as ultrahydrophobe, SDS as surfactant and water as continuous phase. Using different ultrasonication times varied the droplet size. Since measuring the droplet size is a quite difficult task, the droplet sizes in miniemulsions were characterized by cooling down the miniemulsions in order to solidify the droplets, resulting in the particles diameters shown in Table 1. In all cases, the standard deviation of the particle size is smaller than 10 %. Although hexadecane is added as an ultrahydrophobe in many literature known recipes, pure hexadecane miniemulsions still show Ostwald ripening due to the absence of a counteracting osmotic force. Therefore, a third component with lower water solubility than hexadecane is needed to osmotically stabilize the hexadecane miniemulsion. We have chosen perfluorohexane as an effective ultrahydrophobe for hexadecane as it only weakly perturbs the crystallization process.

Table 4.1. Characteristics of the direct miniemulsion systems.

Sample	Diameter (nm)	Crystallization point (°C)	Melting point (dynamic) (°C)	Number of droplets per liter*
direct-1	410	-3.2	19.1	$0.68 \cdot 10^{16}$
direct-2	326	-3.6	19.1	$1.4 \cdot 10^{16}$
direct-3	308	-3.9	18.9	$1.6 \cdot 10^{16}$
direct-4	276	-4.0	18.7	$2.2 \cdot 10^{16}$
direct-5	241	-4.5	18.5	$3.3 \cdot 10^{16}$
direct-6	218	-4.7	18.4	$4.5 \cdot 10^{16}$
direct-7	183	-4.8	18.3	$7.6 \cdot 10^{16}$
direct-8	167	-4.9	18.3	$10.0 \cdot 10^{16}$
direct-9	136	-5.0	18.2	$18.5 \cdot 10^{16}$

* for 20 wt.% hexadecane in water.

DSC measurements were used to investigate the dynamical crystallization temperature of the hexadecane. It is important to note that the continuous phase, the water, is not frozen under the measurement conditions (cooling until -10 °C). Figure 4.1 shows the DSC curves for hexadecane in bulk and for the miniemulsion with hexadecane in droplets (sample direct-6, particle size 218 nm). In order to be able to compare the systems, the bulk hexadecane also contained the same amount of perfluorohexane as the hexadecane in the miniemulsion droplets (2.7 mol-%). The addition of perfluorohexane is expected to depress the (static) melting point only by 0.362 K (calculated with $\Delta H_m = 53.8$ kJ mol⁻¹, $T_m = 18.4$ °C). Heating up the samples with crystallized droplets results in a slight decrease of the (dynamic) melting point in droplets of 0.7 °C from 19.1 °C to 18.4 °C. The temperature at which (dynamic) crystallization of hexadecane in the miniemulsion occurs is much lower than in bulk hexadecane, it was strongly shifted from 12 °C in bulk to about -4 °C in miniemulsion. That means, that the dynamic crystallization is much more influenced than the melting process. Kinetic retardation of crystallization in the droplets as a source of this effect can be excluded by a simple variation of the

undercooling protocol. The miniemulsion was cooled down to 5 °C or 0 °C and hold at the chosen temperature for 24 h no crystallization in the droplets was observed.

In the bulk system, a few nuclei are sufficient to induce (heterogeneous) nucleation followed by crystal growth. In miniemulsion, 10^{16} to 10^{17} sites per liter have to nucleate separately, and crystal growth is limited to the dimension of the droplet. As already stated, the probability of nanodroplets to contain a “foreign” element (not hexadecane) acting as a substrate for heterogeneous nucleation is practically zero. This shifts the mechanism from heterogeneous nucleation to homogeneous nucleation.

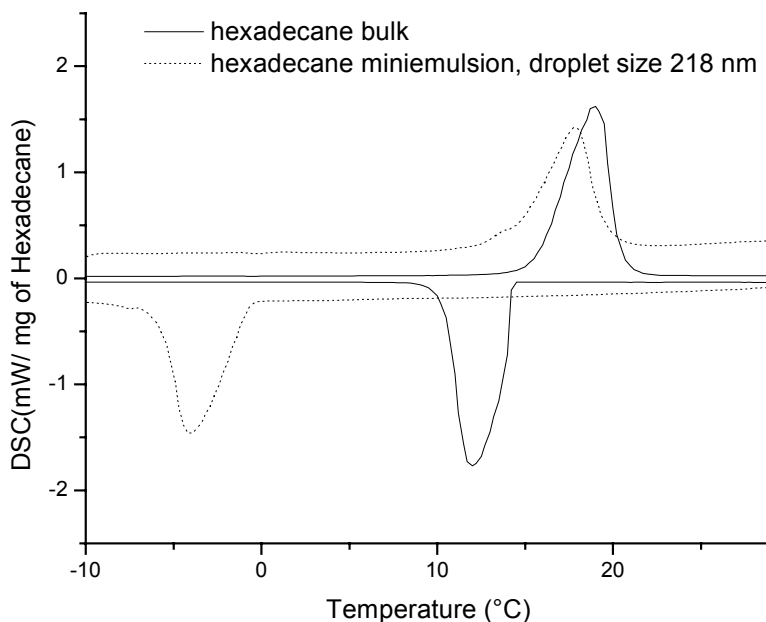
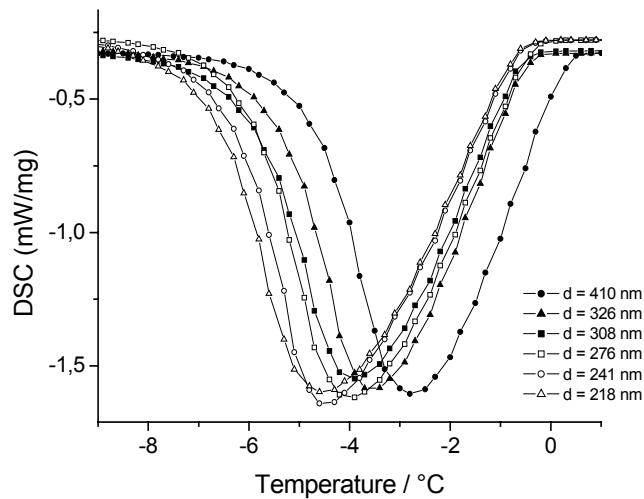


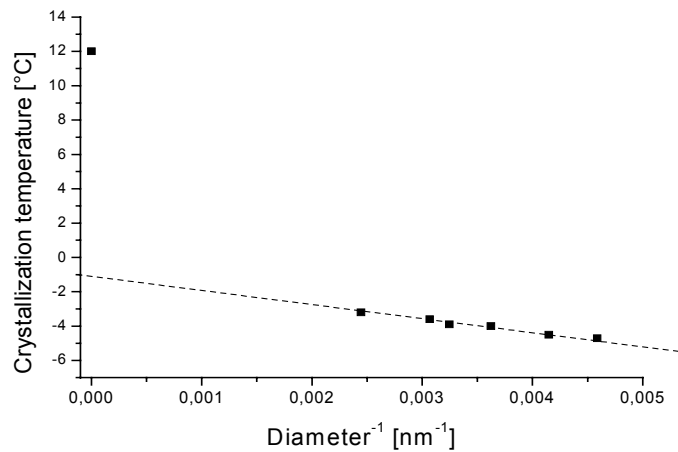
Figure 4.1. Comparison of the crystallization and melting behavior between bulk hexadecane and hexadecane miniemulsion droplets (sample direct-6, 218 nm) as determined by DSC. Cooling and heating rates: $5 \text{ K}\cdot\text{min}^{-1}$.

In Figure 4.2a the DSC scans of miniemulsions with different droplets sizes are shown. In general, the crystallization temperatures decreases with miniemulsions size (see also Table 1), for instance the maximum crystallization temperature for a miniemulsion with average droplet sizes of ca. 400 nm is -3.2 °C while at smaller droplets sizes of ca. 200 nm the crystallization temperature is ca. -4.7 °C . It should be noted that all DSC scans were carried out at the same cooling rate (5 °K min^{-1}), and therefore the effect of cooling rate on crystallization temperatures, which is very strong, can be disregarded. The high stability of the measurements is also indicated by the small fluctuations seen in the plot of

the maximum of crystallization temperature versus the droplet sizes, which shows linear behavior (Figure 4.2b). The fact that the extrapolation for $1/d$ against 0 (which represent the bulk material) leads to a crystallization temperature of $-1\text{ }^{\circ}\text{C}$, far away from the measured $12\text{ }^{\circ}\text{C}$, again clearly indicates a change of nucleation mechanism from heterogeneous nucleation in the bulk to homogeneous nucleation in the droplets. The fact that smaller droplets rely on higher undercooling is also a direct consequence of homogeneous nucleation and the underlying Cahn-Hilliard mechanism:^[164] smaller droplets rely on smaller wavelengths of the chemical potential, which are only stabilized by a deeper temperature quench.



a



b

Figure 4.2. a) Crystallization temperature against the particle size for the direct system. b) Maximum crystallization temperature versus the droplet size.

To be sure that the crystallization behavior in the droplets is not influenced by interactions between the droplets and that indeed each droplet nucleates separately, samples with the same droplet sizes, but in different droplet concentrations were prepared. Indeed, the DSC curves of these samples did not show any dependency of the number of droplets on the crystallization temperature, which indicates the independence of each droplet and no influence by other droplets.

Another potential reason for a change in the crystallization temperature is the thermodynamic influence of the interfacial tension between the droplets and the continuous phase. This can excellently be analyzed since miniemulsions allow one to easily change the interfacial tension without changing the droplet size by post-titrating with surfactant.^[29] After preparing the miniemulsion, SDS was added stepwise in order to decrease the surface and the connected droplet interfacial tension while keeping the droplet size constant. Figure 4.3 shows the *surface* tension of the miniemulsion (γ in $\text{mN}\cdot\text{m}^{-1}$) against the SDS concentration.

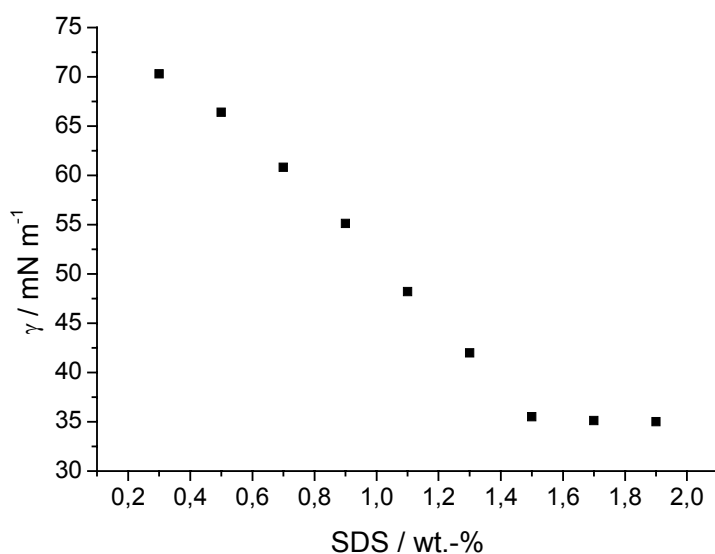


Figure 4.3. Surface tension of the miniemulsion versus the SDS concentration (SDS wt.-%); sample direct-6, droplet size 218 nm, 20 % solid content of hexadecane in water.

A *surface* tension of $70 \text{ mN}\cdot\text{m}^{-1}$ is connected to droplets with a very low surfactant coverage and an *interfacial* tension of $38 \text{ mN}\cdot\text{m}^{-1}$ (this value has been independently measured by an interfacial tension measurement on a plane interface of hexadecane and

water), a *surface* tension of $35 \text{ mN}\cdot\text{m}^{-1}$ represents droplets fully covered by surfactant and corresponds to an *interfacial* tension of $8.7 \text{ mN}\cdot\text{m}^{-1}$ (also independently determined between hexadecane and aqueous SDS solution at the *cmc* concentration). The DSC curves for the samples with different surface tensions are shown in Figure 4.4.

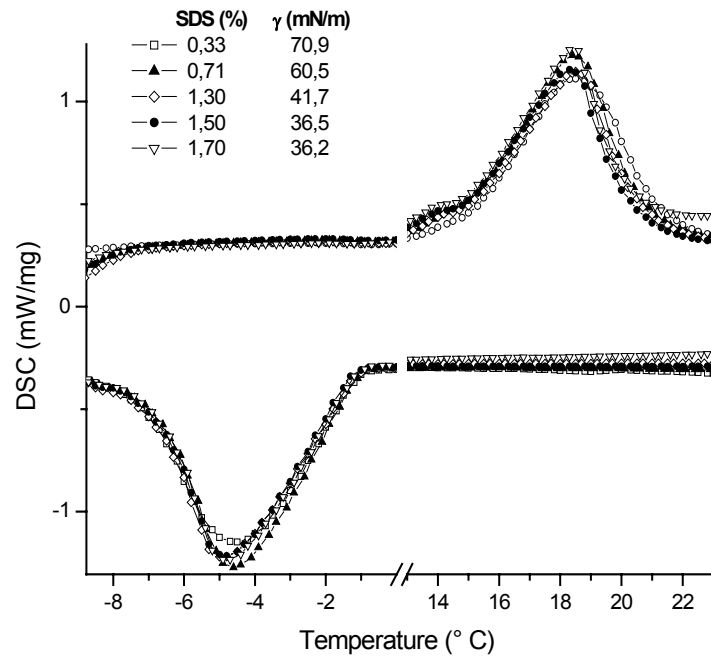
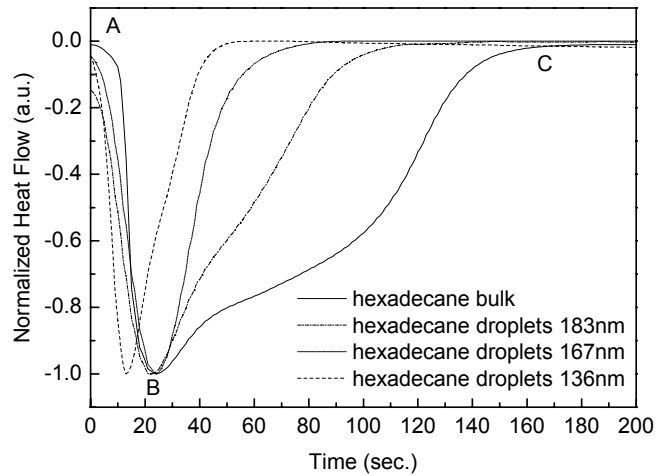


Figure 4.4. DSC curves for miniemulsions with same droplet size, but different interfacial tensions between the hexadecane droplets and the continuous phase.

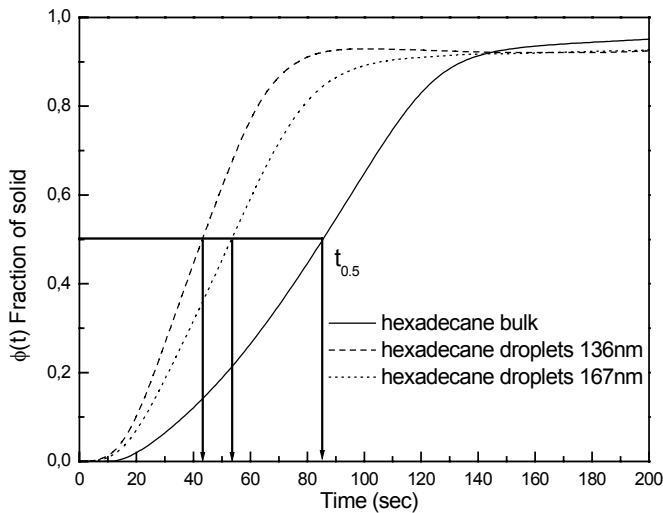
As can be seen, once a miniemulsion with droplets of a defined size is created, the interfacial tension between the continuous and the dispersed phase does not play any role in the changing of crystallization or melting temperature for the droplets, even for the maximal changes as demonstrated in this set of experiments. This result has a number of important implications for the physical chemistry of such nanodroplets:

- The Gibbs-Thomson relation has (still) no importance in this range of droplet sizes. This is not trivial since a surface might influence thermodynamically the crystallization to a certain depth.
- There is also no influence of a droplet- or Kelvin-pressure on the crystallization behavior, at least in this range of droplet sizes or surface sites.
- Nucleation from the surfactant layer can again be excluded.

In order to analyze the crystallization behavior in detail, a closer look to the DSC exotherm is necessary. In Figure 4.5a, a typical DSC crystallization exotherm for isothermal crystallization of hexadecane in miniemulsions of different droplets sizes (183, 176 and 136 nm) and of bulk hexadecane are compared. (All DSC spectra are normalized to bulk hexadecane crystallization).



a



b

Figure 4.5. a) Crystallization exotherms for isothermal crystallization of hexadecane in miniemulsions of different droplets size and of bulk hexadecane. b). The half - time of crystallization, $t_{0.5}$, for hexadecane bulk, and hexadecane droplets of 136 and 167 nm.

Crystallization is assumed to begin at point *A*, which is preceded by a short period presumably due to the required thermal equilibration. Increasing heat flow due to evolution of the enthalpy of crystallization is evident until a maximum is observed at point *B*. The rate of evolution of the enthalpy of crystallization depends strongly on the kinetics of the crystallization process, which is very sensitive to changes in the crystallization temperature. After point *B*, crystallization slows down significantly, and the measurement is terminated (i.e. at point *C*) when no noticeable change in the heat flow is further detected.

An important parameter, which can be measured from Figure 4.5a, is the half time of crystallization, $t_{0.5}$, which is defined as the time from the onset of the crystallization to the point where the crystallization is 50 % complete (see Figure 4.5b). As it can be seen from Figure 4.5, the crystallization rate in the droplets of the miniemulsion (as reflected in the $t_{0.5}$ values) is higher than for the bulk. $t_{0.5}$ for miniemulsion droplets of ca. 140 nm is as short as 42 s, while for the bulk case $t_{0.5}$ is about 85 s. One possible explanation for this effect is an increase of the rate constant with decreasing droplet size. Another explanation for this behavior however is that the heat which is evolved during crystallization can be much better transported from smaller droplets with a large surface to the medium water acting as a heat bath. Attempts to fit the crystallization rate to homogeneous or heterogeneous nucleation (by plotting the rate constant k versus the droplet surface or droplet volume) did not result in a simple relationship illustrating the importance of heat flow effects.

Wide angle X-ray measurements have been used in order to analyze the crystals formed in bulk hexadecane and in hexadecane nanodroplets (confined conditions). Figure 4.6 shows the X-ray diffraction for the bulk hexadecane and the miniemulsions with different particle sizes. The peak positions are slightly shifted to smaller values indicating an expansion of the crystals in the droplets compared to the crystals obtained in bulk. The relative peak intensity ratios shows major changes, and additional weak peaks are coming up, speaking for a change of the crystal shape and a slight distortion of crystal symmetry within the nanodroplets. The crystal morphology therefore indeed sensitively reacts to the droplet confinement. Since the changes in melting behavior are only practically non-existing, these changes mainly concern the crystal superstructure.

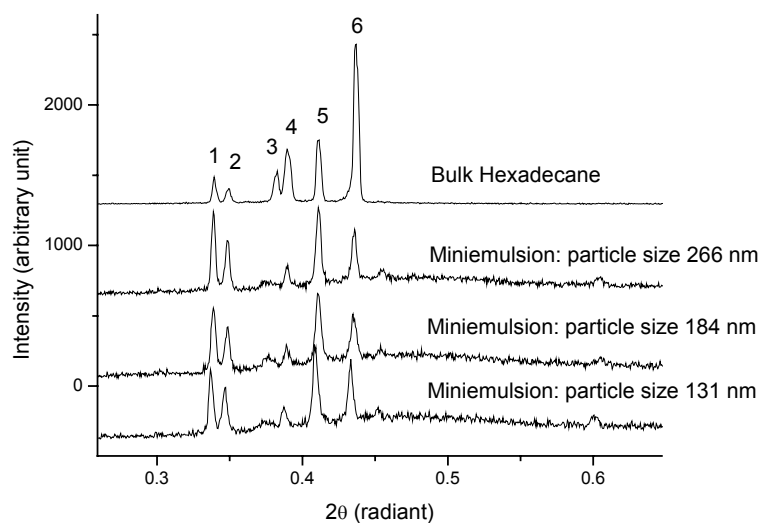


Figure 4.6. X-ray of bulk hexadecane and miniemulsions with different particle sizes. (hkl) interference peaks: 1: (010); 2: (011); 3: (101); 4: (013); 5: (111); 6: (110).

4.1.2 Inverse Miniemulsion

For the preparation of aqueous nanodroplets in a continuous oily environment (inverse miniemulsions), 0.1 M NaCl aqueous solution was miniemulsified in Isopar M. By increasing the time of sonication, different particle sizes were created. The hydrophilic salt NaCl, which is completely insoluble in the continuous phase, is used as the osmotic control agent. The characteristics of the inverse miniemulsions examined are summarized in Table 4.2.

Table 4.2. Characteristics of the inverse miniemulsions

	Droplet size (nm)	Crystallization point (°C)	Melting point (°C)	Number of droplets per liter*
inverse-1	330	-44.6	-0.8	$0.13 \cdot 10^{17}$
inverse-2	257	-45.0	-0.7	$0.27 \cdot 10^{17}$
inverse-3	191	-45.8	-0.5	$0.67 \cdot 10^{17}$
inverse-4	133	-46.3	-1.0	$1.98 \cdot 10^{17}$
inverse-5	109	-46.6	-1.1	$3.65 \cdot 10^{17}$

* for a 20 wt.% dispersion of 0.1 M NaCl solution in IsoparM.

The melting points have to be seen in view of the fact that water crystallizing from salt solutions is practically free of salt (as icebergs), i.e. the melting is the melting of bare ice in presence of a high salt containing droplet, that is a complicated redissolution phenomenon. In the smallest droplets, it is that about 33000 NaCl are pressed out of the water crystals, presumably forming a separate nanophase. This is why we focus for the water nanodroplets only on the undercooling and freezing behavior.

By DSC as shown in Figure 4.7 was observed for the 109 nm droplets a strong shifting of the dynamic crystallization temperature from the bulk NaCl solution (251 K) to the droplets (227 K – 229 K). This is again related to the change of the nucleation mechanism from heterogeneous to homogeneous nucleation in each individual droplet. For the inverse miniemulsion, it is again that the dynamic crystallization temperature is shifting with the droplet size (Figure 4.8).

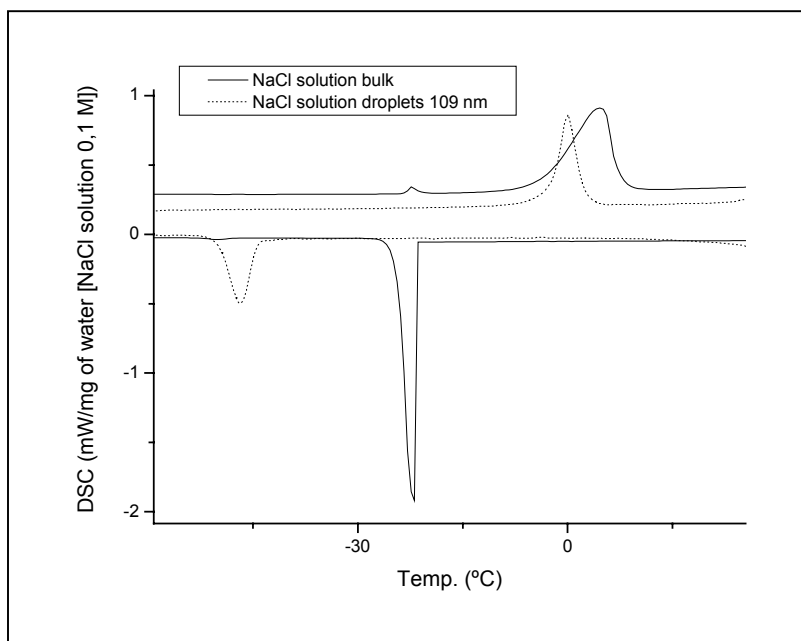


Figure 4.7. Comparison between bulk water (NaCl solution 0.1 M) and in the inverse miniemulsion. Cooling and heating rates: $5 \text{ K} \cdot \text{min}^{-1}$.

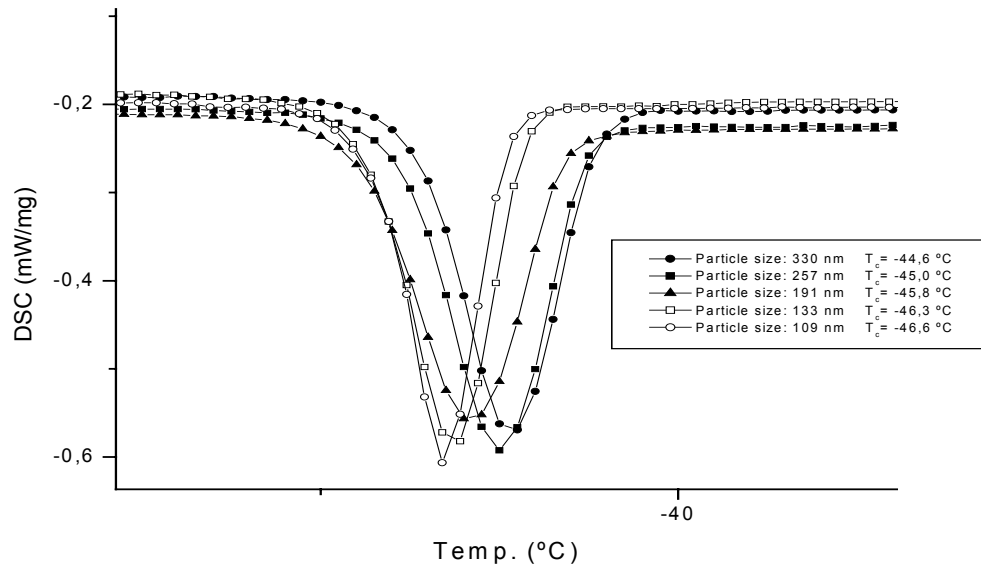
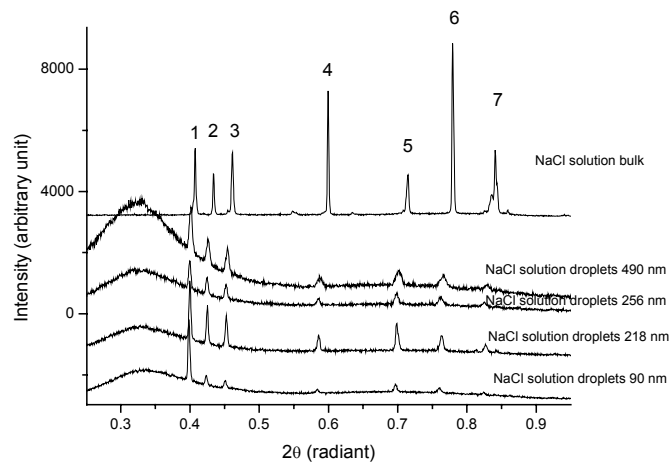


Figure 4.8. The dependence of the crystallization temperature with the particle size in inverse system.

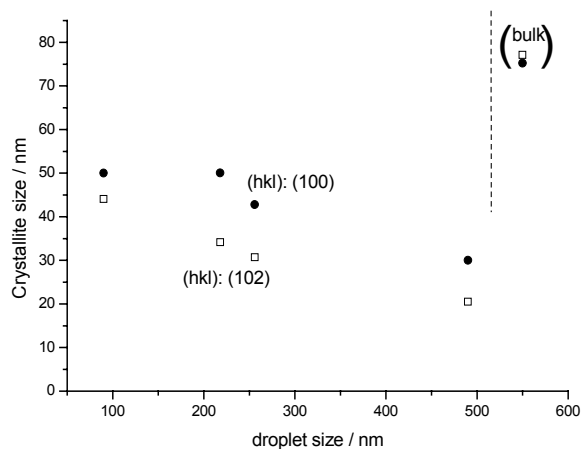
This means that the effects described above do not depend on the chemical nature of the material in the droplet: It is indeed that the wavelength of chemical potential required for homogeneous nucleation is simply smaller for smaller droplets.

The structure of the water crystals however sensitively reacts towards the liquid confinement and shows some interesting peculiarities. Figure 4.9a compares the WAXS spectra of ice crystals grown from bulk NaCl solution and from the corresponding nanodroplets are shown. In any case, a hexagonal ice structure is detected, making crystallization in liquid nanodroplets different from corresponding experiments in mesoporous solids.^[70] Interestingly, although taken clearly from an isotropic dispersion state, the ratios of peak intensity ratios differ between the bulk and the droplet experiments. It is obvious that all the peaks with a z -component are significantly decreased or even wiped out for the droplets, indicating that the ice nanocrystals do just weakly grow in z -direction (growth of xy nanoplatelets).

It can be speculated if this restriction to a close-to-two dimensional shape is typical for the primary nuclei of homogeneously nucleated ice from salt-water or just induced by the nanodroplet starting situation; we however strongly favour the first explanation.



a



b

Figure 4.9. a) Wide angle X-ray for water bulk and droplets with different sizes. (hkl) interference peaks: 1: (100); 2: (002); 3: (101); 4: (102); 5: (110); 6: (103); 7: (200); 8: (112). b) Evaluation of the (hkl) peaks (110) and (102).

From the wide-angle X-ray scattering (WAXS) data, the average size L of the crystallites was estimated from the integral widths B_{hkl} of the (hkl) reflections using the Scherrer equation in the form $L_{hkl} = \frac{k\lambda}{B_{hkl} \cos \theta_{hkl}}$, where the integral width is used in units of radians. The integral widths of the single reflections were obtained from the WAXS data after subtraction of the scattering from the dispersion agent, Isopar M. Taking into

account the instrumental resolution, our WAXS setup allows to determine crystallite sizes up to 80 nm.^[165]

The evaluation of (hkl) peaks (110) and (102) are exemplarily shown in Figure 4.9b. Expectedly, the (110) peak gives a larger L than the (102) peak, containing a weak z -component, again suggesting a rather flat crystal shape. For all peaks it is found that the crystallite size decreases with increasing droplets size. In the 90 nm droplets, crystallites with an in-plane L_{100} of about 50 nm were found, whereas for 490 nm droplets, the crystallites show a size of only about 25 nm. The crystal size of the heterogeneously nucleated water is expectedly very large, i.e. beyond instrumental resolution.

The ice nanocrystals are in all cases smaller than the droplets, which provides non-rupture and droplet stability also in the frozen case. This is not true for all materials showing a pronounced tendency towards one- or two-dimensional crystallization, e.g. naphthalene. This also means that in all cases more than one nucleation site is present in every droplet, presumably a consequence of the spinodal crystallization mechanism, which generates wave-like patterns of nuclei simultaneously.

Since the number of crystals per unit volume depends on the ratio $v_{\text{nucl}}/v_{\text{growth}}$ (velocity of nucleation/velocity of growth), smaller droplets show either a decreased v_{nucl} and/or an increased v_{growth} . Assisted by the kinetic data, it is nearby to assume that indeed it is the rate of homogeneous nucleation, which is smaller for the smaller droplets, although heat flow effects can also not be excluded.

4.2 Metastable phases (rotator phase) in n -alkanes

Since n -alkanes are present in many industrial fields, mainly in the chemical industry, the investigation of the crystallization process of those compounds is of great interest and has attracted the attention of many scientists from different areas, because additionally to its industrial importance, the n -alkanes present remarkable properties during phase transitions, such as the existence of metastable phases, the so-called rotator phase, which are dependent upon the carbon chain length, and even-odd affect. The aim of the following section is the investigation of such metastable phases when confined in miniemulsion droplets. The n -alkanes from hexadecane (C_{16}) to tetracosane (C_{24}) were investigated.

4.2.1 Even alkanes

In the first set of experiments, the crystallization behavior of tetracosane (C_{24}) droplets was compared to that of tetracosane in bulk, using DSC measurements. The crystal structure is determined by X-ray measurements. Cooling down the bulk system leads to a first transition at 45.2 °C (see Figure 4.10a) to obtain the rotator phase as determined by X-ray (see Figure 4.10b) and a second transition at 40.3 °C where a triclinic structure is formed. The characteristic peaks for this structure are: (0 1 0) at 19.40°; (0 1 1) at 20.00°; (0 1 2) at 21.92°; (1 0 1) at 22.31°; (0 1 3) at 23.54° and (1 1 1) at 24.97°.

In miniemulsion, the crystallization occurs in one single step at 30 °C. While heating the miniemulsion droplets, multiple transitions can be detected. For 560 nm and 120 nm droplets, a first transition is seen at 43 °C and another large transition at 51 °C, but in both cases a third very weak transition at 46.3 °C is also visible. Therefore, the temperature at which (dynamic) crystallization of tetracosane in the miniemulsion occurs is lower than in bulk (shifted from 40 °C in bulk to about 30 °C in miniemulsion), whereas the melting process is not much influenced. This can be explained by different nucleation mechanism. In the bulk system, a few nuclei are sufficient to induce (heterogeneous) nucleation followed by crystal growth. In miniemulsion, 10^{16} to 10^{17} sites per liter have to nucleate separately, and crystal growth is limited to the dimension of the droplet. As already stated, the probability of nanodroplets to contain a “foreign” element acting as a substrate for heterogeneous nucleation is practically zero. This shifts the mechanism from heterogeneous nucleation to homogeneous nucleation.

The fact that the melting point of the nanodroplets occurs roughly in the same point as in the bulk system, in contrast to the crystallization, is expected since the release of energy of a droplet during the crystallization, due to the undercooling, is practically instantaneous, because it occurs far from the thermodynamics equilibrium but, at the melting, the droplets absorb energy at a fixed melting point and the kinetics depends on the exchanges with the surrounding medium.^[166] However, as it will be shown for alkanes with different chain length, also the melting point can be shifted significantly.

The X-ray measurements reveal that in the case of 150 nm droplets the stable phase has an orthorhombic structure (instead of the triclinic structure of the bulk phase). This means

that a finite size effect is effective due to confinement of crystallization in the droplets, which influences the crystal morphology. In the 560 nm droplets, the system forms triclinic crystals as in the bulk phase, which leads to the conclusion that for induction of structural changes the droplets must be very small.

In the bulk system, the enthalpy changes for the transition into the rotator phase during cooling were determined to be $-170 \text{ J}\cdot\text{g}^{-1}$ for tetracosane and for the transition into the stable phase $-75 \text{ J}\cdot\text{g}^{-1}$. While heating, the enthalpy ratios of the two transitions only slightly shifted (86 for the first and $159 \text{ J}\cdot\text{g}^{-1}$ for the second transition), the sums of $\Delta H_{\text{cryst1}} + \Delta H_{\text{cryst2}}$ and $\Delta H_{\text{melt1}} + \Delta H_{\text{melt2}}$ are constant. In the miniemulsion, the enthalpy change of the only transition in the cooling procedure, ΔH_{cryst} , is $-240 \text{ J}\cdot\text{g}^{-1}$ for tetracosane, which nicely corresponds to the sum of the bulk system. Evaluating the enthalpy in the heating process, ΔH_{melt} , the first transition has a ΔH_{melt} of $32 \text{ J}\cdot\text{g}^{-1}$ and the second large one has ΔH_{melt2} of $114 \text{ J}\cdot\text{g}^{-1}$. The fact that the enthalpy ratio of the two transitions $\Delta H_{\text{melt1}} / \Delta H_{\text{melt2}}$ is different to the bulk phase can tentatively be explained that in the droplets, tetracosane needs less energy to reach the rotator phase than in the bulk i.e. the molecules in the droplets can easier be mobilized. The seemingly smaller enthalpy during heating might also be attributed to a constant loss of the ordering during the heating process as recently discussed by Thurn-Albrecht et al.^[167]

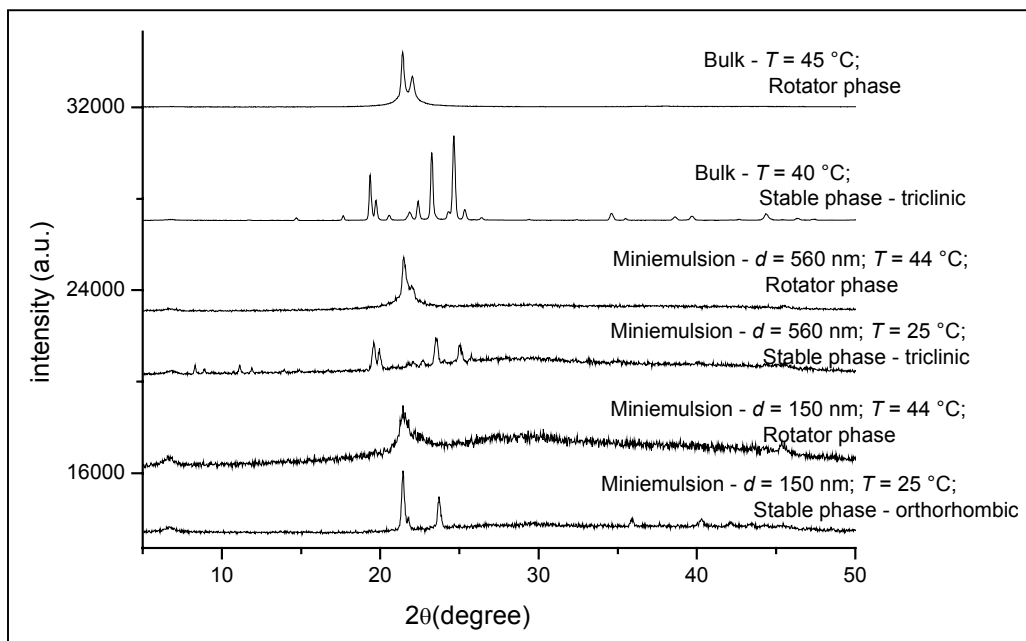
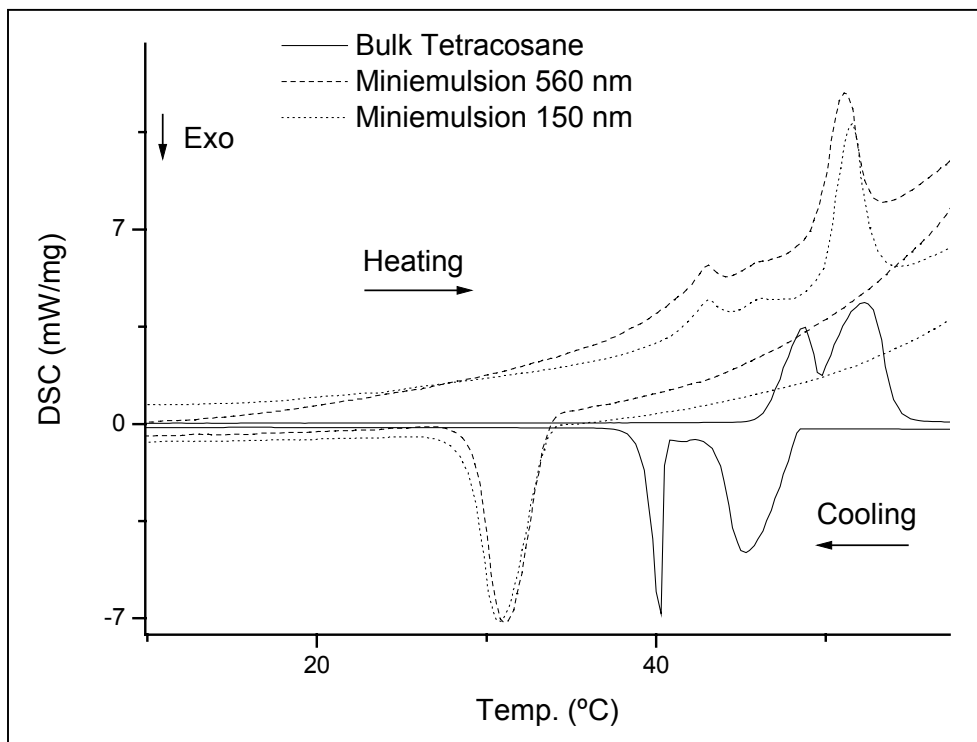


Figure 4.10. DSC and X-ray measurements for tetracosane (C_{24}), droplets and bulk system.

Table 4.3. Melting and crystallization temperature (stable and rotator) for the *n*-alkanes ($15 \leq n \leq 24$)

Number of Cs		Cooling			Heating		
		T_{C1} (°C)	T_{C2} (°C)	ΔT_C (°C)	T_{m1} (°C)	T_{m2} (°C)	ΔT_m (°C)
15	bulk	3.7	-6.9	10.6	-1.7	11.6	13.3
	droplets: 169 nm	-9.4	-14.4	5.0	-3.7	9.7	13.4
16	bulk	-	12.0	-	-	19.0	-
	droplets: 208nm	-	-4.7	-	-	18.8	-
17	bulk	14.3	5.6	8.7	12.3	25.0	12.7
	droplets: 140nm	2.8	-1.4	4.2	9.6	21.9	12.3
18	bulk	-	19.5	-	-	31.2	-
	droplets: 125nm	8.2	5.6	2.6	15.3	27.3	12.0
19	bulk	25.6	17.4	8.2	22.7	33.7	11.0
	droplets: 111nm	13.4	11.7	1.7	17.7	31.2	13.5
20	bulk	30.1	28.4	1.7	-	40.2	-
	droplets: 129 nm	-	19.0	-	24.1	36.2	12.1
21	bulk	34.2	27.3	6.9	33.1	42.7	9.6
	droplets: 126 nm	-	21.8	-	30.0	40.7	10.7
22	bulk	37.0	33.9	3.1	44.8	48.0	3.2
	droplets: 121 nm	-	25.0	-	35.1	44.4	9.3
23	bulk	41.6	35.5	6.1	41.6	50.2	8.6
	droplets: 128 nm	-	28.5	-	39.2	47.8	8.6
24	bulk	45.2	40.3	4.9	48.7	52.2	3.5
	droplets: 150 nm	-	30.6	-	43.2	51.5	8.3

T_{C1} : Transition from the liquid phase to the metastable (rotator phase) crystalline phase during the cooling process

T_{C2} : Transition from the metastable (Rotator phase) crystalline phase to the more stable phase

$\Delta T_C = T_{C1} - T_{C2}$: Difference between these two crystallization steps

T_{m1} : Transition from the stable crystalline phase to the metastable (rotator phase) during the heating process

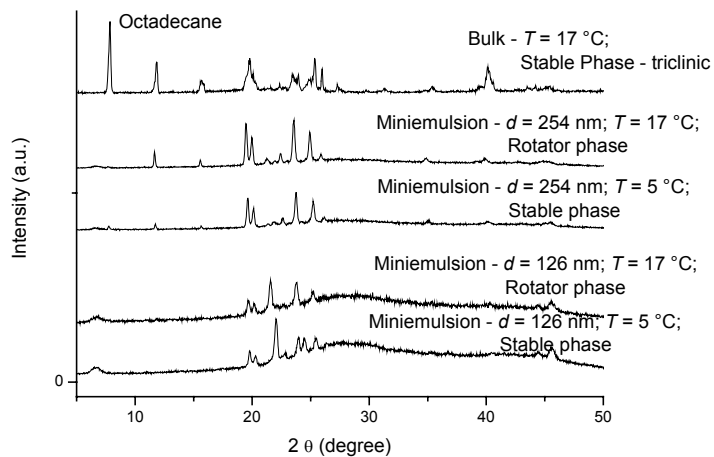
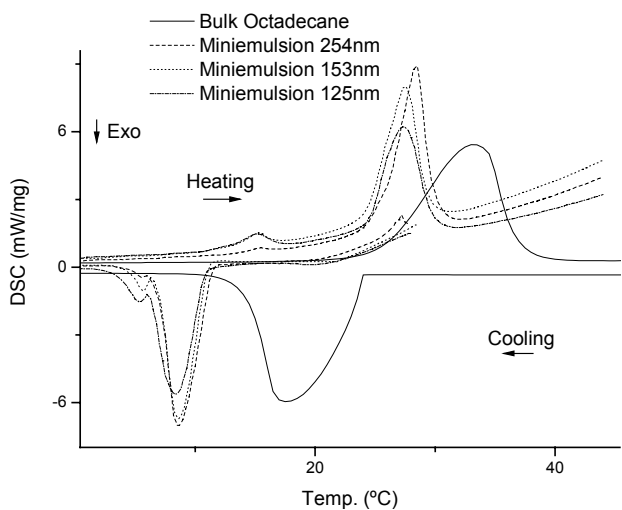
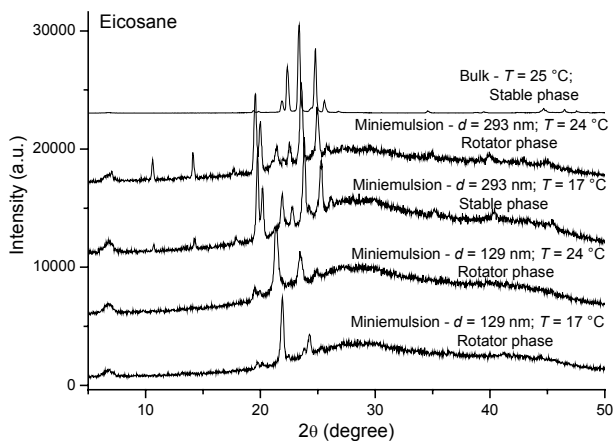
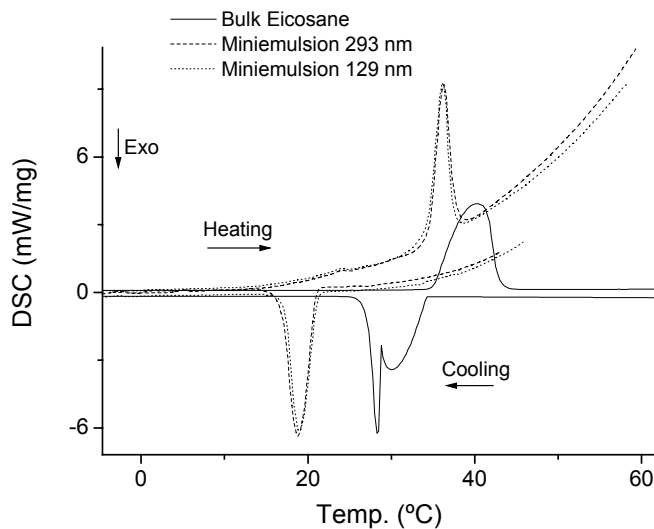
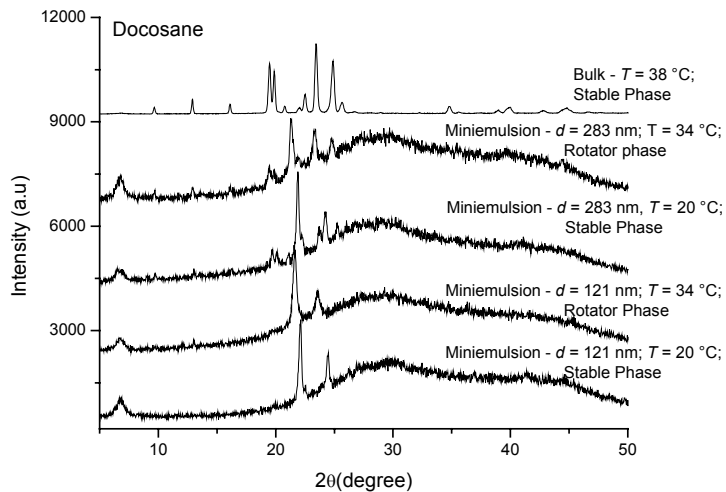
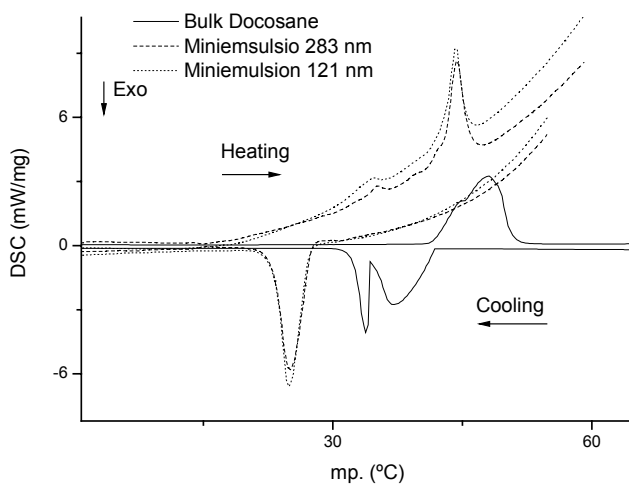
T_{m2} : Transition to liquid state

$\Delta T_m = T_{m1} - T_{m2}$: Difference between the beginning of the metastability (rotator phase) and the melting point during the heating process

Table 4.4. Areas under the transitions of the DSC curves and ratios.

Number of Cs		ΔH_{cryst1}	ΔH_{cryst2}	$\frac{\Delta H_{cryst1}}{\Delta H_{cryst2}}$	ΔH_{melt1}	ΔH_{melt2}	$\frac{\Delta H_{melt2}}{\Delta H_{melt1}}$
15	bulk	-161.2	-39.2	4.1	40.6	157.2	3.9
	droplets: 210nm	-148.7	-22.4	6.6	-	140.6	-
	droplets: 169 nm	-151.1	-26.6	5.7	26.4	142.5	5.4
16	bulk	-	-220.8	-	-	219.8	-
	droplets: 308 nm	-	-206.5	-	-	205.9	-
	218 nm	-	-205.7	-	-	193.2	-
17	bulk	-175.7	-42.46	4.1	43.8	161.2	3.7
	droplets: 490 nm	-171.4	-31.67	5.4	29.6	150.0	5.1
	droplets: 153 nm	-147.3	-21.75	6.8	29.0	149.8	5.2
	droplets: 134 nm	-150.1	-26.0	5.8	26.3	149.0	5.7
18	bulk	-	-213.3	-	-	212.2	-
	droplets: 254 nm	-261.5	-8.30	31.5	1.88	239.4	127.3
	droplets: 153 nm	-256.0	-23.6	10.8	8.07	210.5	26.1
	droplets: 125 nm	-225.4	-39.1	5.8	17.7	188.5	10.6
19	bulk	-176.3	-47.4	3.7	55.0	168.2	3.1
	droplets: 198 nm	-169.6	-47.4	3.6	15.8	136.6	8.6
	droplets: 135 nm	-157.9	-36.4	4.3	8.0	112.6	14.1
	droplets: 111 nm	-163.0	-30.0	5.4	10.7	109.2	10.2
20	bulk	-145.8	-84.9	1.7	-	233.1	-
	droplets: 293 nm	-	-248.2	-	-	189.3	-
	droplets: 129 nm	-	-179.7	-	2.29	155.8	68.0
21	bulk	-170.4	-51.0	3.3	65.4	156.6	2.4
	droplets: 193 nm	-	-205.3	-	19.8	110.0	5.6
	droplets: 126 nm	-	-197.7	-	14.8	93.5	6.3
22	bulk	-147.3	-63.0	2.3	57.4	162.6	2.8
	droplets: 283 nm	-	-199.3	-	11.5	115.1	10.1
	droplets: 121 nm	-	-198.1	-	12.4	99.2	8.0
23	bulk	-133.4	-43.6	3.1	61.0	116.8	1.9
	droplets: 196 nm	-	-173.9	-	17.4	90.0	5.2
	droplets: 150 nm	-	-165.7	-	10.2	78.9	7.8
24	bulk	-170.5	-75.23	2.3	86.4	159.7	1.9
	droplets: 560 nm	-	-242.2	-	31.8	114.3	3.6
	droplets: 150 nm	-	-239.1	-	27.2	134.3	4.9

In the next sets of experiments, the behavior of shorter even alkanes, namely C₂₂, C₂₀, C₁₈, and C₁₆, in droplets is examined and compared to the properties in bulk. The DSC graphs and the X-ray diagrams are shown in Figure 4.11, the data extracted from the DSC curves are summarized in Table 4.3 and 4.4.



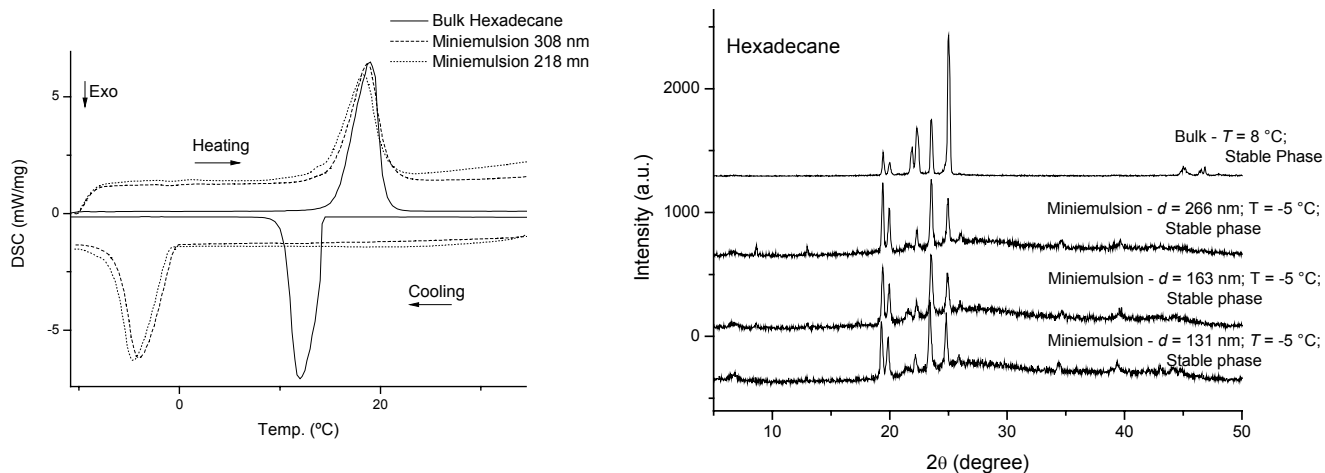


Figure 4.11. DSC and X-ray measurements for some even alkane, droplets and the bulk systems. Docosane (C_{22}), eicosane (C_{20}), octadecane (C_{18}) and hexadecane (C_{16}).

In the case of the C_{22} , C_{20} , and C_{18} alkanes, the situation for crystal formation is very similar to the C_{24} case. Whereas in the bulk systems of C_{22} and C_{20} throughout cooling a transition into the rotator phase and then into the stable phase is obtained, in miniemulsion only one single transition is detected. For the C_{18} , the metastable phase was also not observed in the bulk, as this alkane crystallizes directly in the most stable phase, the triclinic one. When melting, it goes directly from the stable phase to the liquid phase. This may be the possible reason for the relative higher melting points of the even-alkanes, since the triclinic systems have greater packing efficiency and thus stability compared with monoclinic and orthorhombic systems.^[83] Gerson et al.^[168] and Roberts et al.^[169] have shown through alkane solubility measurements that the triclinic is the most stable solid phase. As seen earlier, the transition into the stable structure occurs in miniemulsion at much lower temperatures, which can be attributed to homogeneous nucleation. However, it should be noted here that for the C_{22} , C_{20} and C_{18} alkanes also the melting point is significantly lowered by up to 4 K.

However, heating up the miniemulsion droplets consisting of those alkanes leads again to two transitions, the first transition into the rotator phase is very weak, the second transition is strong. In the case of C_{18} , there is a strong dependence on the droplet size on the ratio of $\Delta H_{\text{melt}1}$ and $\Delta H_{\text{melt}2}$. With decreasing droplet size, $\Delta H_{\text{melt}1}$ increases

significantly which leads to the conclusion that the confinement in the droplets has a supporting influence on the pre-melting transition. Comparable to the C24 miniemulsion, the sum of ΔH_{melt} of the two transitions is significantly smaller than the sum of ΔH_{cryst} of the systems. The X-ray measurements reveal that for small droplets (120 nm), an orthorhombic phase is formed. From the positions of the peak, it is seen that in this phase the crystal is better packed than in the rotator phase. The stable phase of the bulk system is triclinic.

This again shows nicely the influence of the droplet confinement on the crystal morphology. For larger droplets (300 nm), mixed structures (triclinic and orthorhombic) are obtained, in the case of C₂₂, the orthorhombic structure, and in the case of C₂₀ and C₁₈, the triclinic structure is favored. From these measurements we can estimate that below a critical size of about 250 nm the confinement has a strong influence on the crystal structure. In addition, the finite size effect becomes less significant with decreasing chain length.

In the case of C₁₆, we have neither for the bulk nor for the miniemulsion detected a rotator phase, and direct crystallization into the triclinic structure occurs. While the peak (1 1 1) is the more intense in the bulk it decreases in the droplets, and the first two peaks (0 1 0) and (0 1 1) that are small in the bulk become very intense in the droplets. In addition, the (0 1 2) peak almost fully disappears in the droplets, indicating a preferential two-dimensional growth and shape selectivity in the droplets.

Although Sirota et al. reported that the difference between the melting temperature and the rotator equilibrium transition temperature is roughly constant as a function of chain length,^[97] we have seen (Figure 4.12) that for the bulk odd-alkanes this distance decreases with increasing the alkyl chain, and for the bulk even-alkanes it increases from C₂₀ on, as we did not observe the rotator phase in the even-bulk alkanes before that size.

4.2.2 Odd-alkanes

The size quantization effect on odd alkanes turned out to be qualitatively very different so that the experiments with odd alkanes have to be separately discussed in this section.

For the bulk odd-alkanes one can clearly see a double transition in the cooling as well as in the heating step. In the cooling step the first transition, T_{C1} , corresponds to the

transition from the liquid state to the rotator phase (orthorhombic), the following one, T_{C2} , corresponds to the final crystallization in the immobile phase, again an orthorhombic one. For the melting process, the first transition, T_{m1} , corresponds to the transition from the immobile orthorhombic to the mobile orthorhombic phase, and T_{m2} the transition from the rotator phase to the liquid state.

In miniemulsions, the crystallization takes place also for the odd alkanes at lower temperature, but the structure in the droplets does not undergo any structure shift. As in the bulk system, the orthorhombic structure is formed. The X-ray diffractogram shows two characteristic peaks, the first (1 1 0) at $2\theta = 21.7^\circ$ and the second (2 0 0) at $2\theta = 24.1^\circ$. As expected the low temperature phase shows more well defined peaks than the rotator phase. The transition from the rotator to the low temperature phase promotes a homogeneous strain on the crystals as indicated by the slight shift in the peak position. For all odd alkanes for a chain length between C_{15} and C_{23} , neither the increase in chain length nor the different droplet sizes show a remarkable influence on the orthorhombic crystals. The crystallite size roughly decreases (see Table 4.5) with increasing alkyl chain, but does not show any direct relationship with droplet size, probably due to the stochastic nature of the nucleation.

Beside the absence of structural differences between the bulk and the miniemulsion droplets of different sizes for the odd alkanes, the temperature shifts of the phase transitions are of interest.

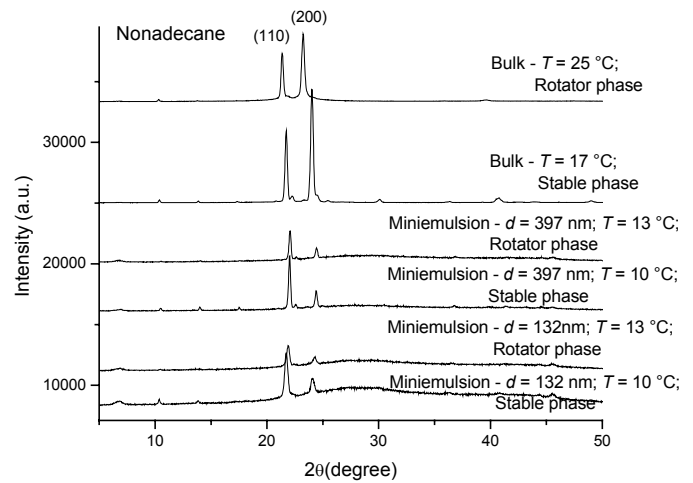
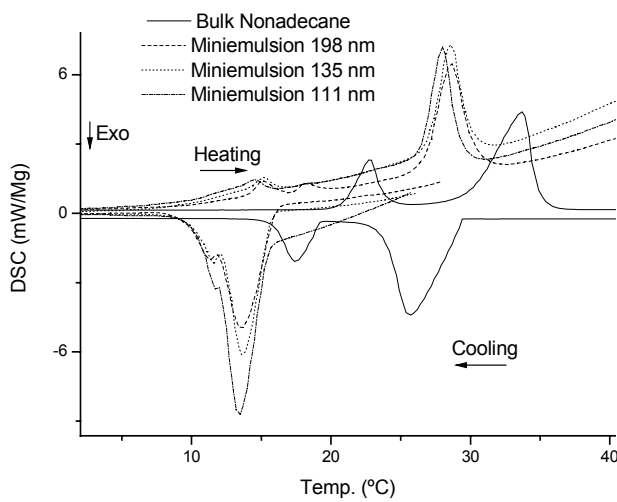
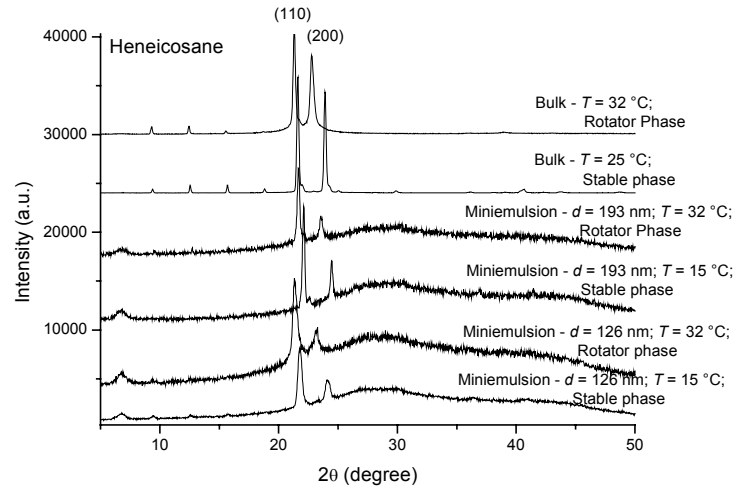
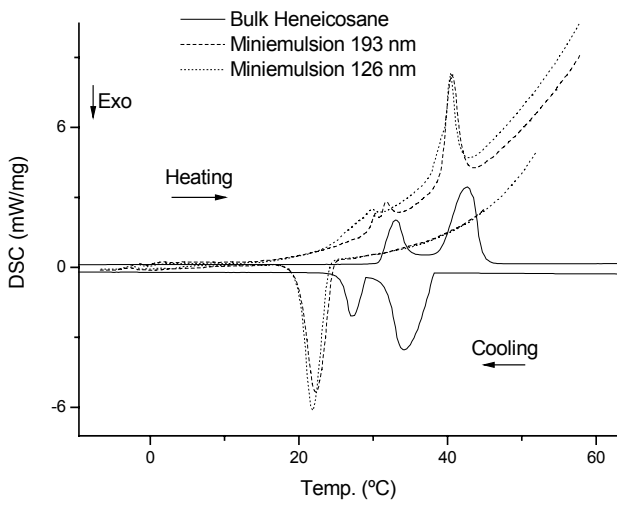
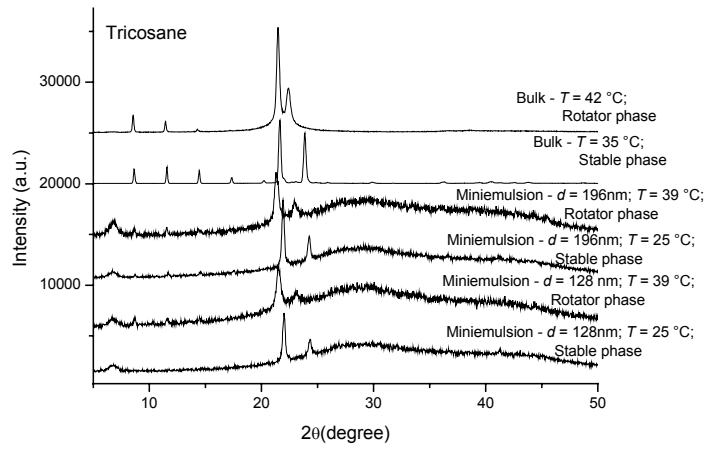
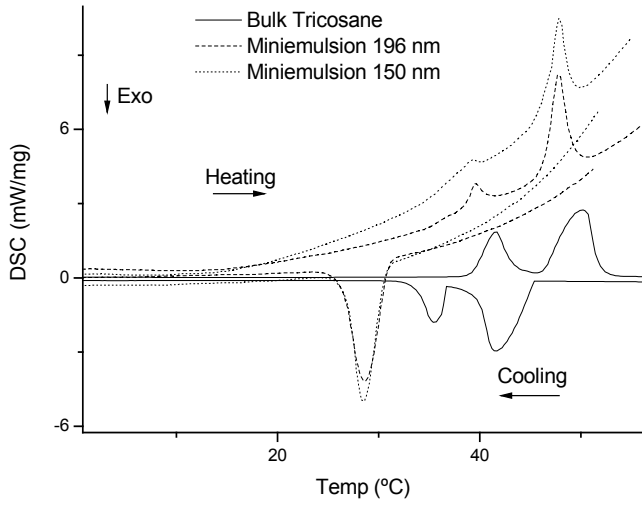
For the cooling step the difference between T_{C1} and T_{C2} decreases for the odd alkanes in the bulk phase. For the miniemulsions of these alkanes, the difference between the first and second transition in the cooling step ($\Delta T_C = T_{C1} - T_{C2}$) is drastically reduced in comparison to the bulk and decreases with increasing alkyl chain from C_{15} to C_{19} . During the heating procedure, the nanodroplets and the bulk behave however very similar, and ΔT_m ($\Delta T_m = T_{m2} - T_{m1}$) only decreases with increasing the alkyl chain. This is indicative for the kinetic character of the found temperature shifts.

Figure 4.13 shows the differences of the transition temperatures between the bulk and miniemulsion for the even alkanes and the odd alkanes as well. For the cooling step we took the difference between the transitions to the stable phase of the bulk and the miniemulsion, and for the heating step, the transitions to the liquid state.

Looking at the differences of the transition temperature to the stable phases (T_{C2} and T_{m2}) between the bulk and the miniemulsion, it is seen that the crystallization and the melting in droplets is always shifted by the same factor for odd alkanes and is independent of the chain length which corresponds well to the fact that the confinement leads to a decrease of the crystallization and melting temperatures, but does not influence the structure.

Even alkanes in comparison show in the cooling process that this temperature shift decreases with increasing the alkyl chain until C_{20} , at carbon chains $> C_{20}$ the difference increases again. For the melting process one can see the inverse effect, the difference increases until C_{20} and decreases afterwards. This is now due to the fact in the case of the even alkanes also a structural shift is observed which additionally influences the transition to the stable phase.

In Figure 4.14 the ratio of $\Delta H_{\text{cryst1}}/\Delta H_{\text{cryst2}}$ (from cooling) and $\Delta H_{\text{melt2}}/\Delta H_{\text{melt1}}$ (from heating) are presented for all alkane miniemulsions. For the even alkanes, the ratios show minimal values for small droplets and increase with increasing particle size, resulting in an infinite value of bulk (where only one transition is seen). The reverse case is seen for the odd alkanes, where the bulk shows small ratios for $\Delta H_{\text{cryst1}}/\Delta H_{\text{cryst2}}$ and $\Delta H_{\text{melt2}}/\Delta H_{\text{melt1}}$. Here, with decreasing droplet size the ratios increase.



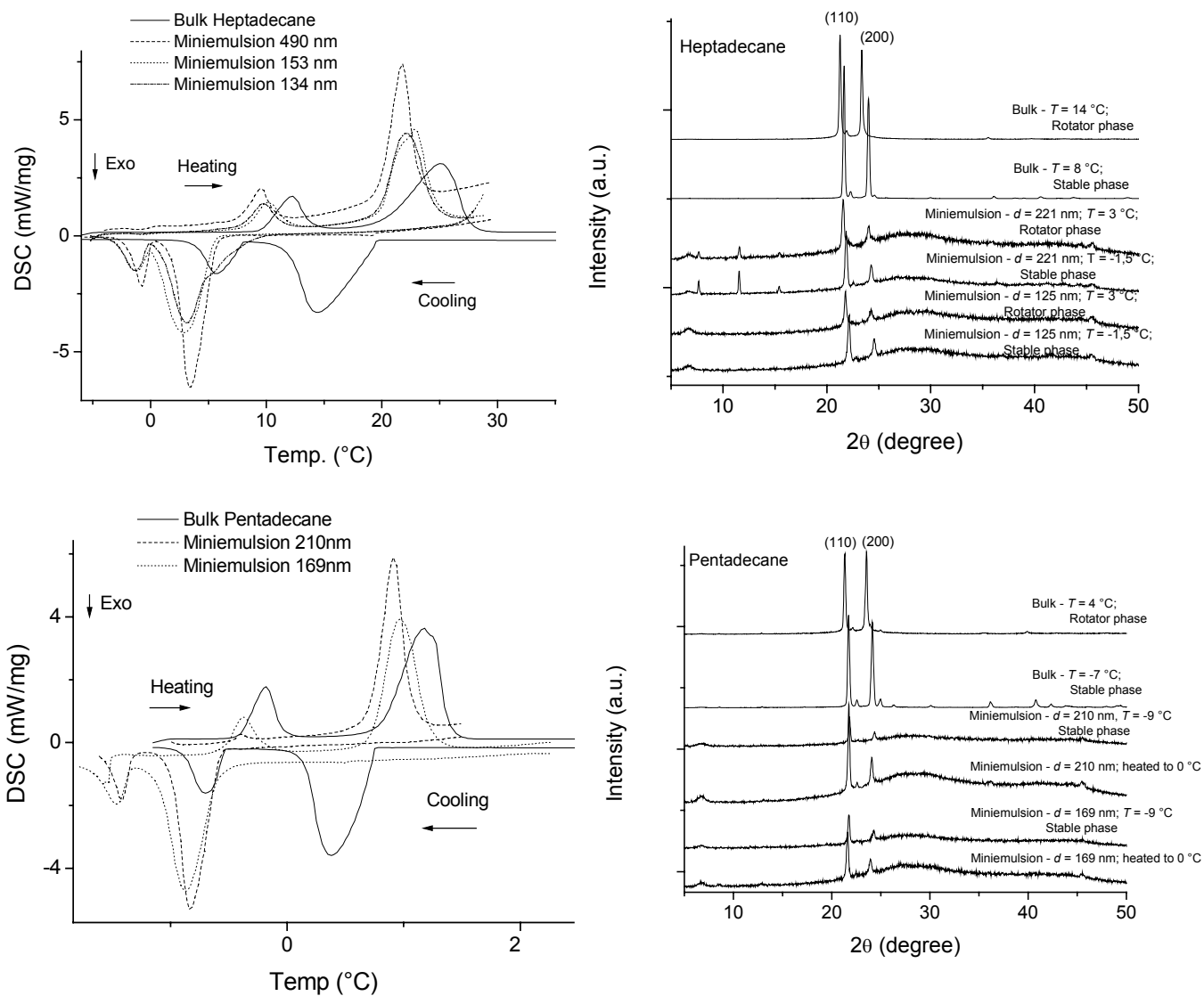


Figure 4.12. DSC and X-ray measurements for odd alkane droplets and bulk systems, tricosane (C_{23}), heneicosane (C_{21}), nonadecane (C_{19}), heptadecane (C_{17}) and pentadecane (C_{15}).

Table 4.5. Crystal sizes (in Å) obtained from the X-ray measurements.

number of atoms	bulk-rotator		bulk-stable		miniemulsion (ca. 200 nm* droplets) rotator phase		miniemulsion (ca. 200 nm*) stable phase		miniemulsion (ca. 120 nm*) rotator phase		miniemulsion (ca. 120 nm*) stable phase	
	(110)	(200)	(110)	(200)	(110)	(200)	(110)	(200)	(110)	(200)	(110)	(200)
15	375	431	374	378	426	378	426	377	373	300	427	335
17	498	428	427	378	376	501	334	335	428	500	374	376
19	375	336	376	378	427	431	499	431	333	336	300	300
21	375	274	499	431	242	244	428	431	229	336	230	201
23	217	251	243	335	229	300	375	334	230	200	333	378

* for exact sizes see Table 4.2.

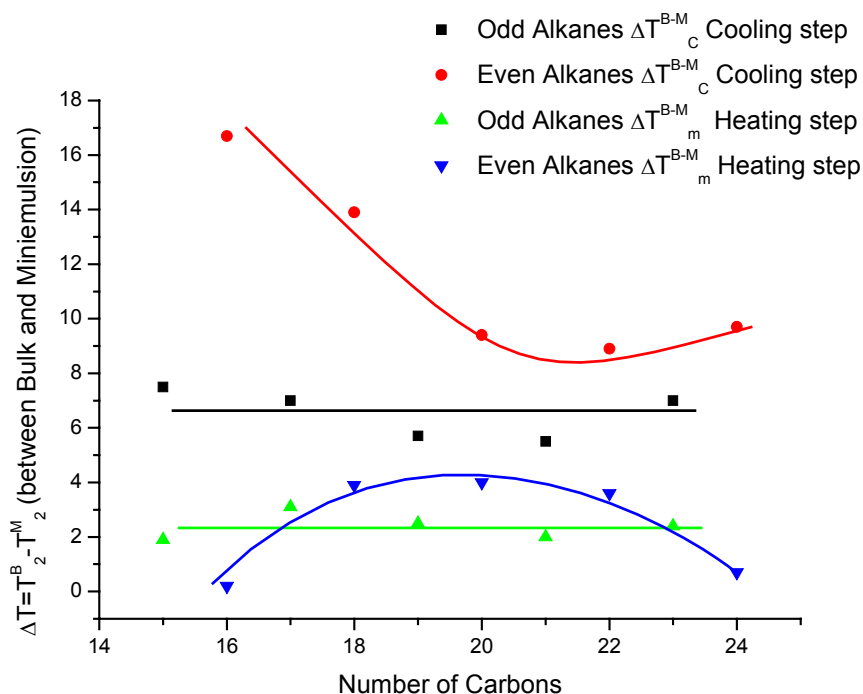


Figure 4.13. Temperature shift for the crystallization and melting (only the transition in the stable state) between the bulk and the miniemulsions. Data taken from Table 4.3.

ΔT_C^{B-M} : difference of the stable transitions between bulk and minemulsion on cooling.

ΔT_m^{B-M} : difference of the stable transitions between bulk and minemulsion on heating.

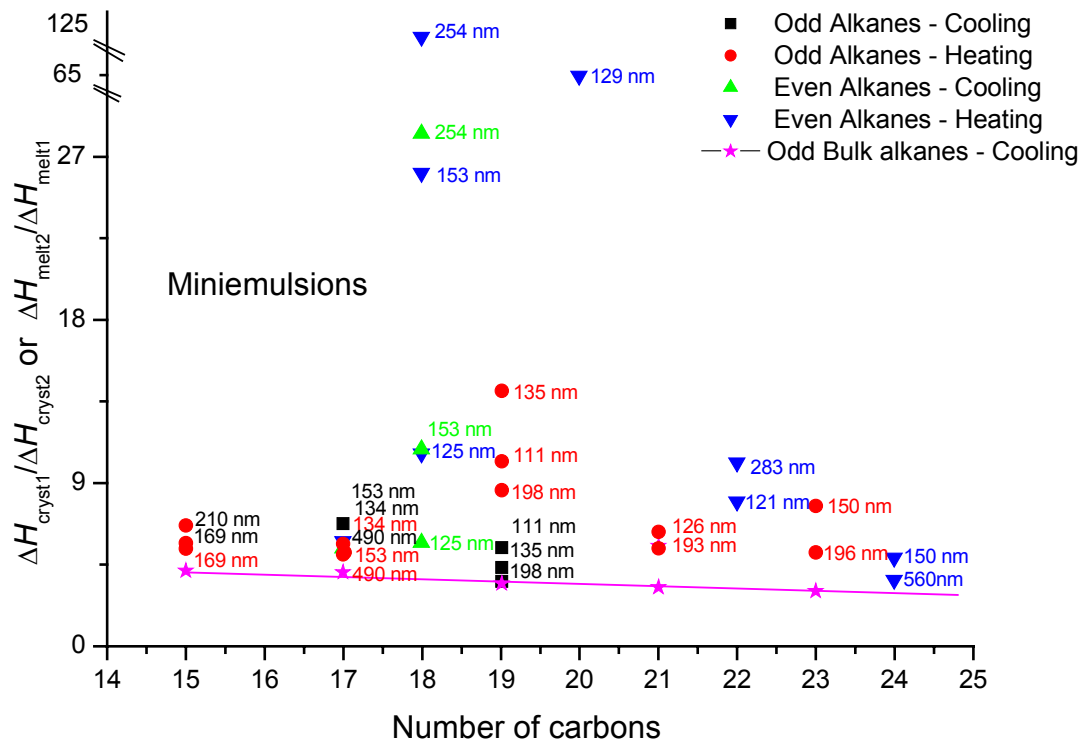


Figure 4.14: Ratio of $\Delta H_{\text{cryst1}}/\Delta H_{\text{cryst2}}$ (from cooling) and $\Delta H_{\text{melt2}}/\Delta H_{\text{melt1}}$ (from heating) for the miniemulsions. Data taken from Table 4.4.

4.3 Bioinspired materials

The search for materials with improved properties and for very delicate applications, as required in pharmaceutical and medical fields has brought the scientists to look to nature for inspiration. In this section we apply the miniemulsion approach to prepare cross-linked gelatin nanoparticles, which have potential applications in the pharmaceutical field. Given that gelatin is a biocompatible material and shows thermo-reversible properties, it is suitable for use as drug carrier.

Since these particles can be dispersed in water to obtain stable dispersions, one can mimic nature and carry out biomineralization reactions. In section 4.3.2 it is shown that the procedure to obtain a hybrid material, which is the combination of gelatin nanoparticles and nanocrystals of hydroxyapatite, which were biomineralized within those particles. Such a material has the potential to be used as a bone implant.

4.3.1 Gelatin nanoparticles

Since gelatin is a hydrophilic biopolymer and dissolves in hot water, the formation of distinct nanoparticles directly in water is not easily possible. In order to obtain now gelatin particles in water, a three-step procedure was developed. In the first step, gelatin droplets in an organic phase were created at high temperature in the absence of physical cross-linking; these droplets were cross-linked in the second step of the procedure. In the third step, the cross-linked particles were transferred to water.

In the first step, stable inverse miniemulsions consisting of droplets containing 500 mg of gelatin and different amounts of water were obtained by using only 70 mg of the block copolymer P(B-E)/PEO as stabilizer. The droplet size was about 100 nm. The continuous phase was chosen to be cyclohexane in order to allow an easy removal of this phase for further application. The gelatin chains themselves act as hydrophilic agent to suppress Ostwald ripening in the inverse miniemulsion since gelatin is practically insoluble in cyclohexane.

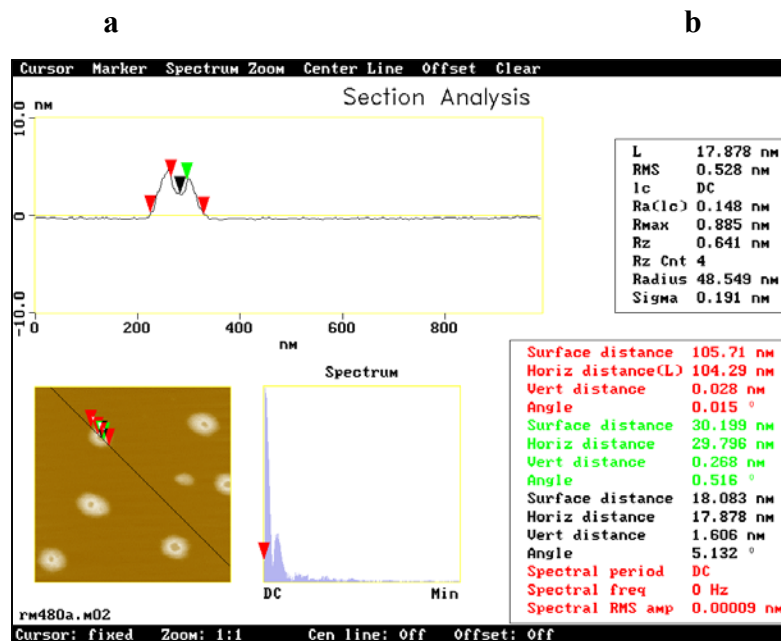
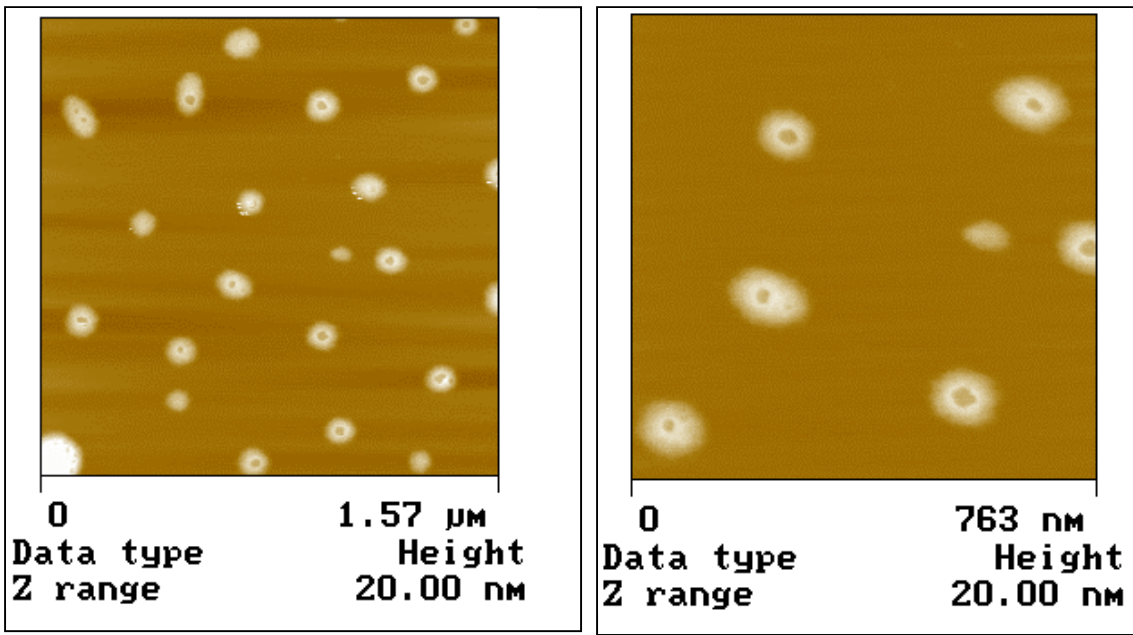
In the second step, the reaction was carried out by the concept of the fission and fusion process.^[170] A second miniemulsion containing droplets with the cross-linking agent was added and the mixed miniemulsions were csonicated in order to have a forced exchange

of the droplet contents. Table 4.6 shows the different samples prepared under different conditions. In the third step, the inverse miniemulsions were freeze-dried to remove the cyclohexane and then redispersed in cyclohexane. In all cases, stable dispersions in water were obtained.

Table 4.6. Different samples of gelatin particles obtained with varying contents of water varying cross-linking time.

Sample	Glutardialdehyde [mg]	Water [g]	Cross-linking time [min]
RM480	50	10	8
RM484	50	10	20
RM485	50	10	60
RM487	50	15	8
RM491	50	8	8

AFM measurements were first used to investigate the morphology of the re-dispersed gelatin particles. Figure 4.15 shows the spin-coated aqueous dispersion consisting of gelatin particles RM480 (cross-linking time: 8 min) as measured at room temperature. The photographs show well-defined gelatin particles, which are soft and collapse under its own weight forming a concave in the middle of the particles, as better seen in the section analysis picture (Figure 4.15c).



c

Figure 4.15. AFM of the gelatin particles after redispersion in water (sample RM480: 8 min of cross-linking) measured at room temperature.

Increasing cross-linking time leads to a higher number of agglomerated and bigger particles as one can see in the AFM views for the samples RM484 and RM485 (Figure 4.16a and 4.16b). Whereas in the case of 8 min cross-linking only the intraparticle

cross-linking was favored, longer cross-linking times lead to a significant amount of undesired interparticular cross-linking. This is in accordance with Leo et al.^[171] who carried out hardening of gelatin with glutardialdehyde, and reported that time longer than 11 min led to many large particles.

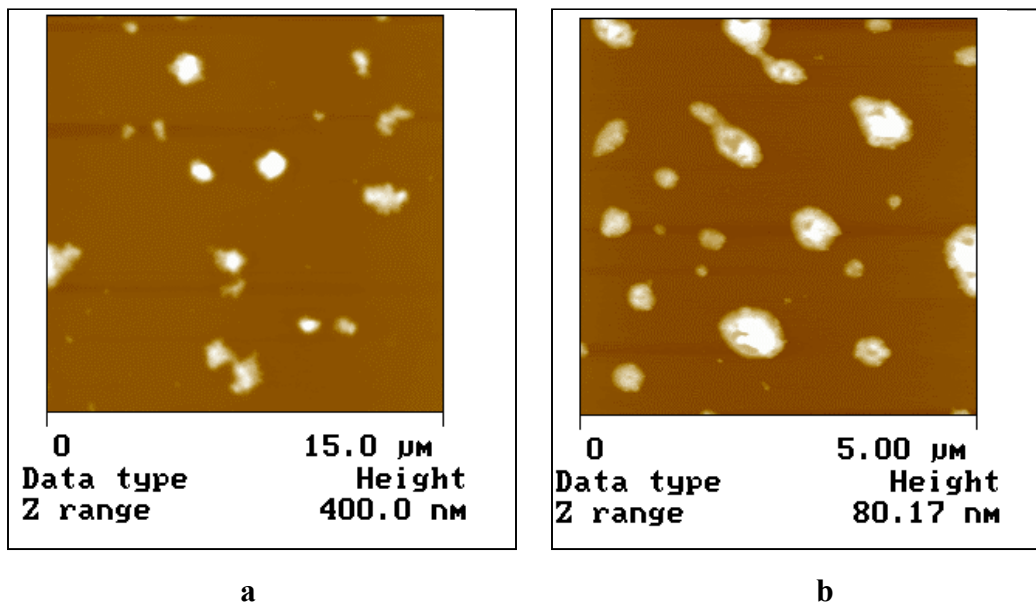
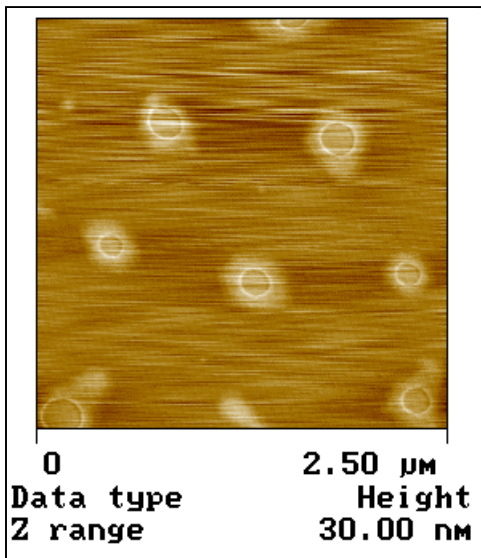
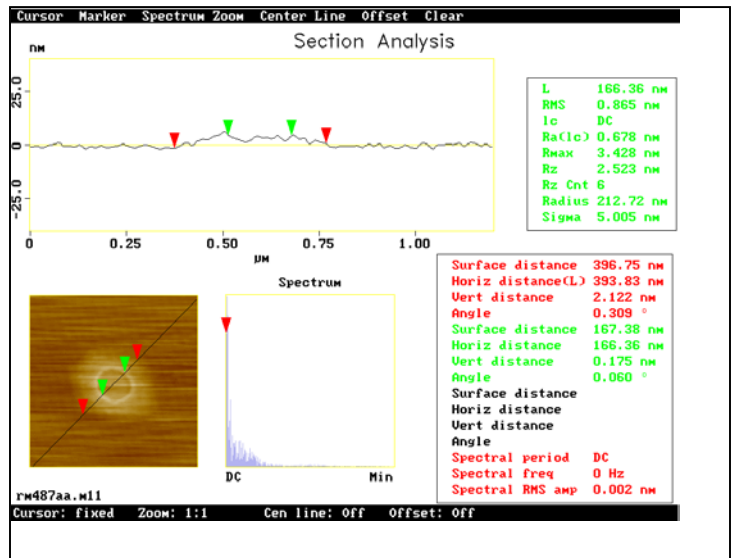


Figure 4.16. AFM of the gelatin particles after redispersion in water: a) samples RM484 (20 min of cross-linking) and b) RM485 (60 min of cross-linking) measured at room temperature.

In the next sets of experiments, the amount of water for preparation of the gelatin droplets in the inverse miniemulsion was varied. As a maximum amount of water 15 g / 500 mg gelatin was chosen. Due to the solubility reasons, water content of 8 g/ 500 mg gelatin could not be done. Figure 4.17 shows the AFM pictures of particles obtained with a high amount of water (sample RM487). Due to the higher water content, the particles appear softer. As can be seen in the section analysis in Figure 4.17b, the particle flattens almost completely on the mica surface. In contrast with that, a low amount of water used in the preparation (RM491) promoted the formation of harder particles with a rough surface.

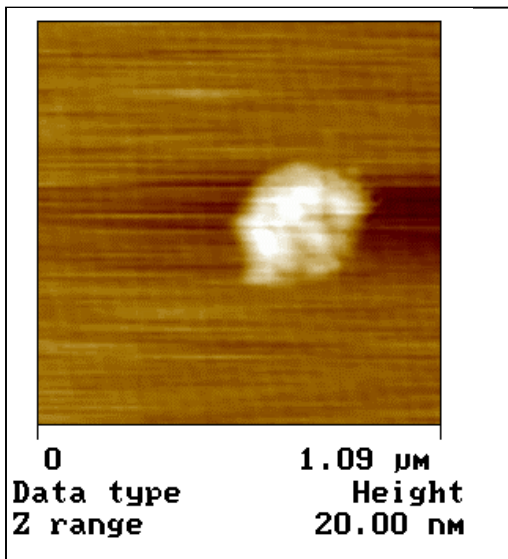


a

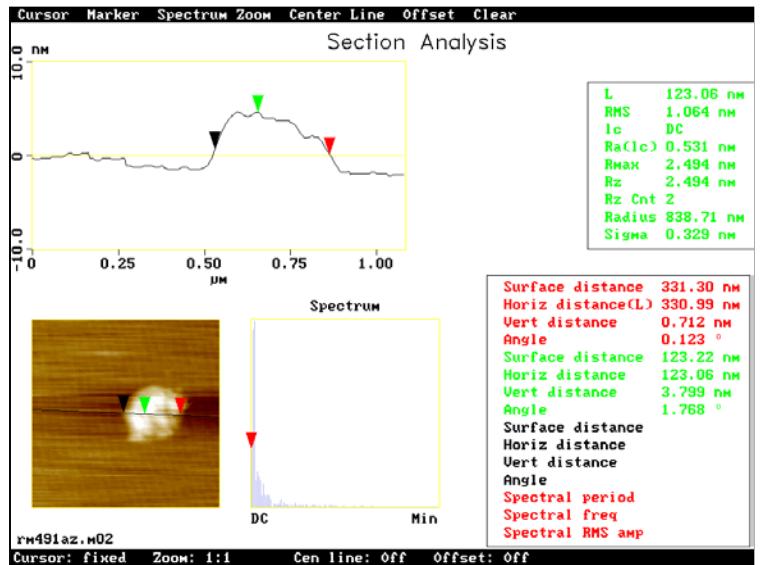


b

Figure 4.17. a) AFM picture of RM487; b) Section analysis of the sample RM487.



a



b

Figure 4.18. AFM picture of the sample RM491. The particle is harder with a rough surface.

FTIR was used to investigate the cross-linking efficiency on the gelatin chains inside the particles. In Figure 4.19, IR spectra of the cross-linked gelatin particles are compared to pure (not cross-linked gelatin) As can be seen in Figure 4.19, the evidence of the cross-linking is observed on the intensity increasing of the typical bands attributed to the amide groups, which are formed by the cross-linking agent glutardialdehyde and the gelatin chains. Although the exact mechanism of protein cross-linking with glutardialdehyde is not yet clearly defined, it is shown by the other authors that ϵ -amino groups of the lysine residues and the N-terminal amino groups of the protein are involved. It is described in the literature that the amide formed in the cross-linking process, even though they are in a small quantity compared to the amide groups from the peptide chain, can be identified by IR. This was attributed to a different chemical surrounding and mobility of the amides. The stretching of the $C=O$, which is attributed to the formed amide groups, is observed in the region between $1700\text{-}1600\text{ cm}^{-1}$. The stretching of the $N-H$ also from the amide groups is observed at 3303 cm^{-1} . The $C-H$ stretching is identified as a weak band at 3069 cm^{-1} . The deformation of $N-H$ bond in observed in two different regions, between $1500\text{-}1550\text{ cm}^{-1}$ and between 1200 and 1300 cm^{-1} .

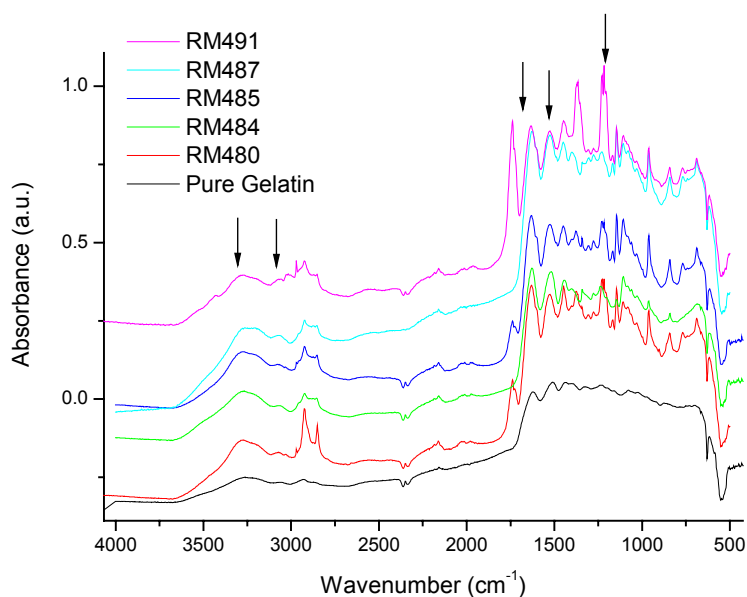


Figure 4.19. FTIR of the pure gelatin and the cross-linked gelatin nanoparticles.

From the infrared spectra, a cross-linking can be observed in all gelatin particles. The highest cross-linking concentration is seen in sample RM491 what is directly related to the higher number of gelatin chains per particle, since lower amount of water has been used to dissolve the gelatin, increasing the probability of inter-chain connections. This observation is in agreement with the AFM picture of sample RM491 (Figure 4.18) that shows very hard particles. In the same manner, one can look at the spectrum of the sample RM487 (the lowest initial gelatin concentration) and observe the inverse, since as also shown by the AFM picture (Figure 4.17); here the softest particles are formed. However, a longer cross-linking time in the samples RM484 and RM485 does not lead to a significant higher overall cross-linking degree, a few cross-linking bridges between the particles seem to form the big agglomerates. Therefore, the initial gelatin concentration is the most important parameter for the controlling of the cross-linking density within the particles.

The thermal behavior of the particles is of great interest. Figure 4.20 shows the DSC curves of the dried gelatin nanoparticles. As the sample is heated up, a transition starting at about 30 °C is detected. This transition can be attributed to the loss of physical cross-linking points. At temperatures below 30 °C, both physical *and* chemical cross-linking is still efficient. The degree of physical cross-linking is indirectly also related to the amount of chemical cross-linking. Whereas for sample RM487 the transition in DSC is very smooth and have decreased intensity, the transition in the case of RM491 is more abrupt and much shorter. In the cooling step the transition is not detected here with this cooling rate of 5 K/min, due to a retardation of the transition.

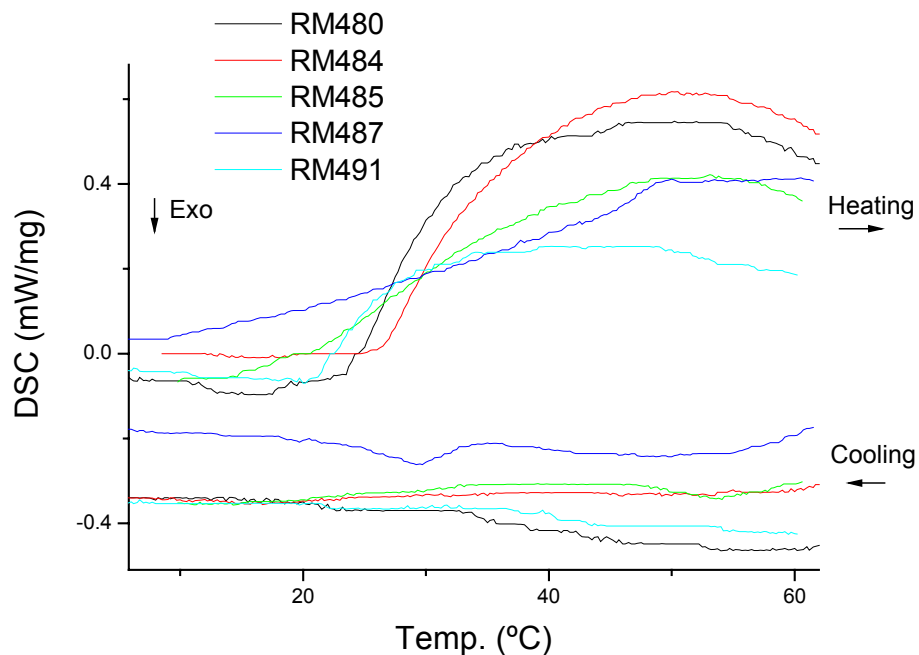


Figure 4.20. DSC measurement of dried gelatin particles (heating and cooling rate: $5 \text{ K}\cdot\text{min}^{-1}$).

To observe how the particles look like under heating, we have done AFM measurement of sample RM480 at $40 \text{ }^\circ\text{C}$. As nicely seen in the Figure 4.21, the particles undergo a softening process while heating, which again can be attributed to the loss of the physical cross-linking between the chains. Therefore, the particles flatten making the formed concave to become even more pronounced.

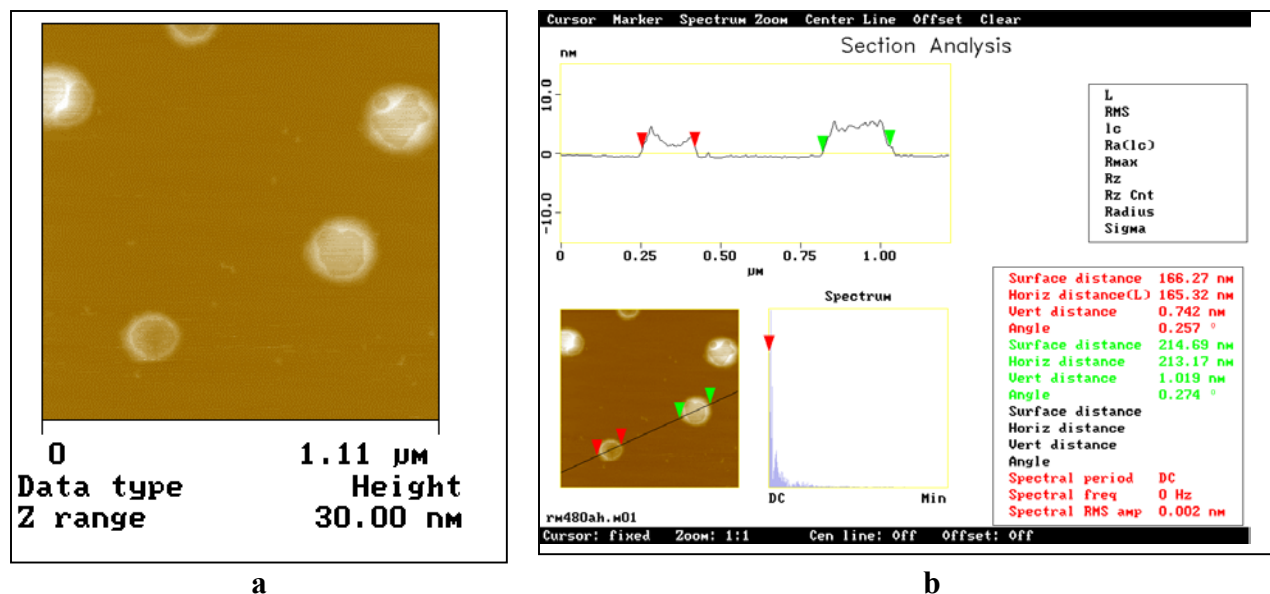


Figure 4.21. AFM picture of the sample RM480 at 40 °C.

The behavior of the particles in water was studied with dynamic light scattering. Figure 4.22 shows the mean diameter values for the samples against the temperature. It can be seen that the diameter of the gelatin particles increases at increasing temperature. This is in accordance to the previous experiments and again be attributed to the loss of physical cross-linking. Decreasing of the temperature leads to a shrink of the particles to a size which can be even lower than the size of the initial particles.

Here, two possible explanations can be given: 1) Chemically non-cross-linked gelatin chains might have exit the particles during the heating process or 2) a better packing of the chains is obtained.

The swelling and deswelling of particles in dependence of the temperature is of great advantage in field of drug delivery, e.g. drugs can be adsorbed in the particles and a drug-release is possible in near-natural temperature range.

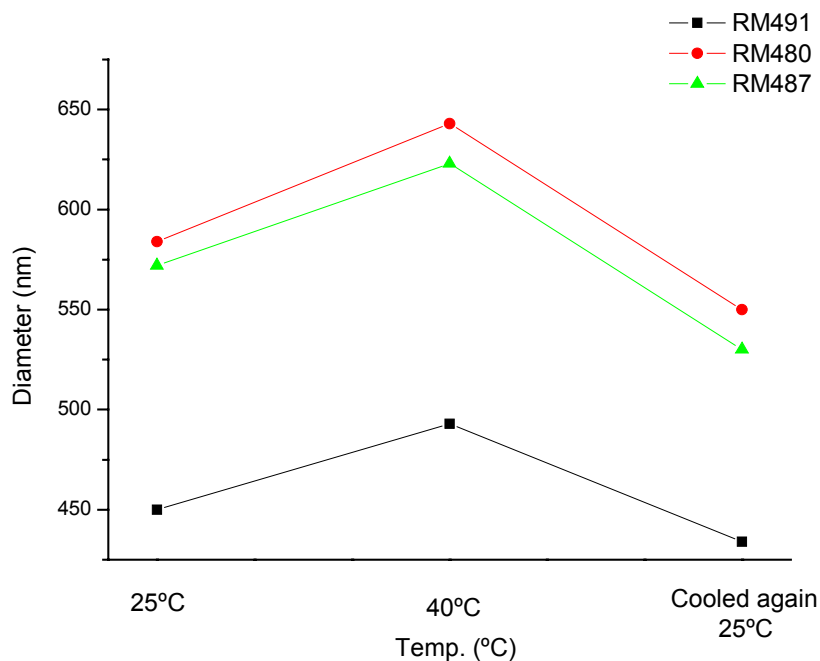


Figure 4.22. Swelling effect of the particles in water and thermo-reversibility.

It is shown in this part that the miniemulsion process together with the concept of fusion and fission is a reasonable method to prepare cross-linked gelatin particles. However, the glutardialdehyde seems to be not the most efficient cross-linking agent since degradation can take place in the presence of water. Therefore future work has to be done for an improvement of the stability of the cross-linking in the particles.

4.3.2 Biomineralization of hydroxyapatite within gelatin nanoparticles

Even though the gelatin particles cross-linked with glutardialdehyde are not yet perfect, we have performed first experiments to show the potential for future applications.

As a reference experiment, Na_2HPO_4 and CaCl_2 were first reacted in absence of any gelatin nanoparticles leading to the formation of platelet-like calcium phosphate (see Figure 4.23).

For the biomineralization experiment, the negatively charged gelatin particles were preloaded with the Ca^{2+} ions and then the Na_2HPO_4 solution was slowly added to the reaction mixture in order to obtain hydroxyapatite. The formation of hydroxyapatite in gelatin particles was performed at different temperature and different pH values since the properties of gelatin and the morphology of calcium phosphate are very sensitive to pH and temperature. Table 4.7 shows the characteristics of the prepared samples. Figure 4.24 shows the AFM pictures of HAP crystals, which are formed in gelatin particles at room temperature and 37 °C and at different pH values.

The formation of HAP in the presence of gelatin nanoparticles shows very different patterns than the calcium phosphate formed in the absence of gelatin.

A formation of HAP at neutral pH and at room temperature (Figure 4.24c) leads to neuron-like structures growing from each individual gelatin particle. No crystal formation outside the gelatin particles is found, but each crystal is started within the gelatin particles because of the Ca^{2+} “pool” in it. The whiskers are around 200 nm in length and few nanometers in thickness. The reactions performed at higher temperature (37 °C), but at the same pH value (pH 7) show basically the same pattern as the one at room temperature, but the whiskers are longer than at room temperature. This behaviour can be attributed to the higher swelling degree of the particles at higher temperature. Whereas at room temperature the swelling degree of gelatin particles is quite low due to physical and chemical cross-linking of the particles, at 37 °C an increased swelling of the gelatin nanoparticles due to the loss of physical cross-linking is observed.

Changing the pH to pH 5, also the formation of whiskers is seen, however, the HAP size is increased as is can be seen in the AFM pictures in Figure 4.24a for the preparation at room and in Figure 4.24b for the preparation at higher temperature. An increase of the pH

to pH 10 has a strong influence on the formation on HAP formation, here the whiskers where completed vanished. The differences can have two different origins: 1) the increasing pH leads to higher deprotonation of the gelatin and therefore a better complexation of the Ca^{2+} ions by two COO^- groups. 2) The pH of 10 already dissolves the HAP at the outside of the particles. Both explanation leads to the same conclusion, that the crystals grow takes place only inside the particle.

Table 4.7. Characteristics of the reaction conditions for biomineralization of HAP in gelatin particles.

Sample	PH	Temperature (°C)	Whiskers
1	5	RT	Yes
2	5	37	Yes
3	7	RT	Yes
4	7	37	Yes
5	10	RT	No
6	10	37	No

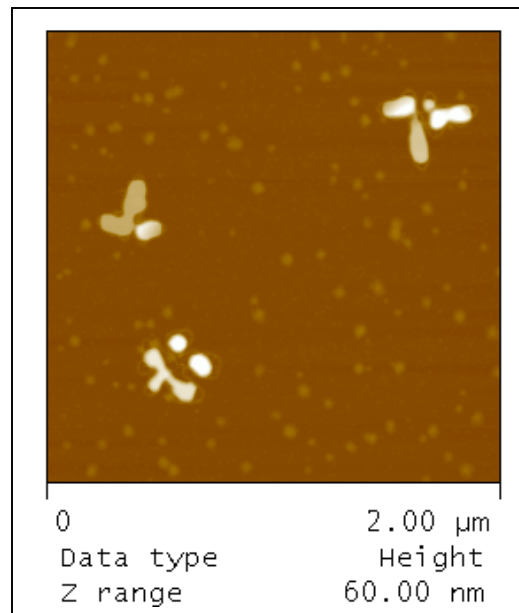
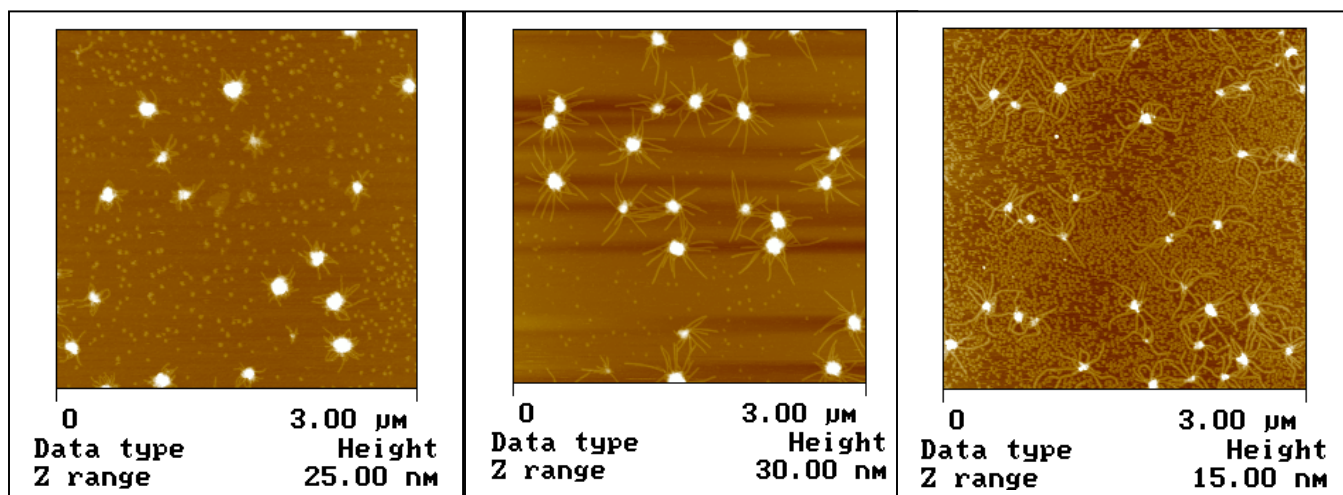


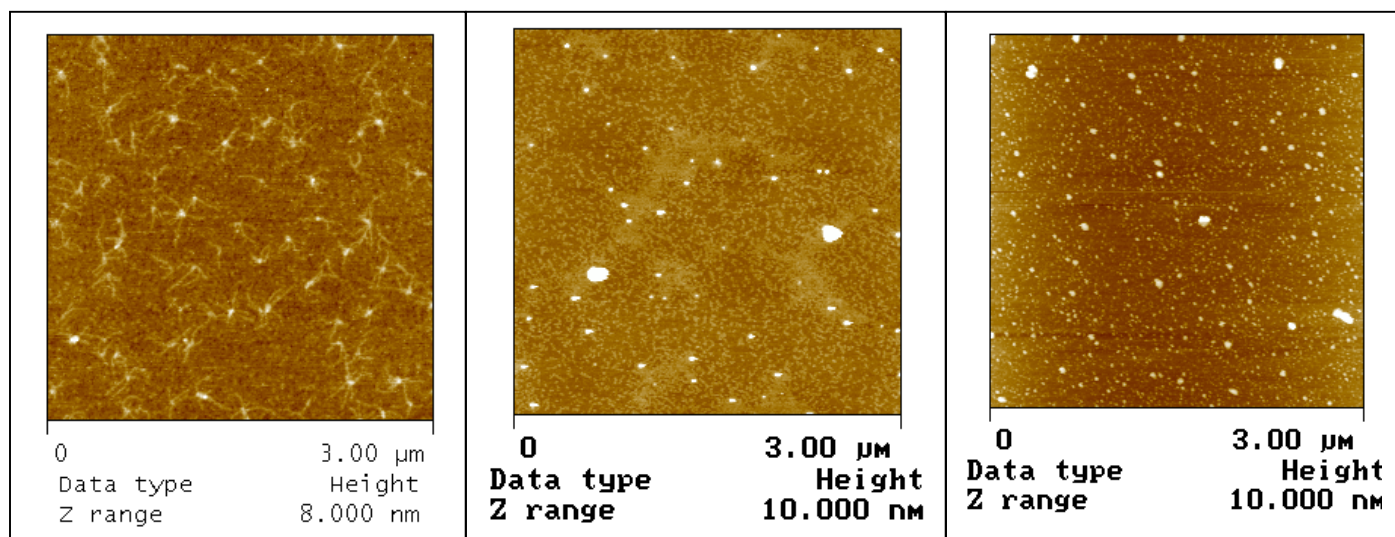
Figure 4.23. Calcium phosphate crystal formed outside the gelatin particles.



a-Sample 1

b-Sample 2

c-Sample 3



d-Sample 4

e-Sample 5

f-Sample 6

Figure 4.24. AFM (height) pictures. Influence of pH and temperature (Table 4.7).

Wide-angle X-ray (WAXS) was also used to investigate the differences in the morphologies of HAP formed in our method.

Figure 4.25 shows the X-ray diffraction diagrams for all samples listed in Table 4.7, for comparison the X-ray diffraction diagram of reference calcium phosphate is also shown.

The typical main diffraction peaks for HAP are present in all cases, independent whether the nucleation occurred at the different pH values inside or also outside the gelatin particles. The X-ray results show that the samples prepared at pH 7 and 5 but at 37 °C, samples 4 and 6 respectively, have produced longer whiskers than the corresponding samples prepared at room temperature. As indicated by the increased intensity of the peak (100) at $2\theta = 32.07^\circ$ the growth happens in one direction along the x-axis. This is in full agreement with the AFM pictures.

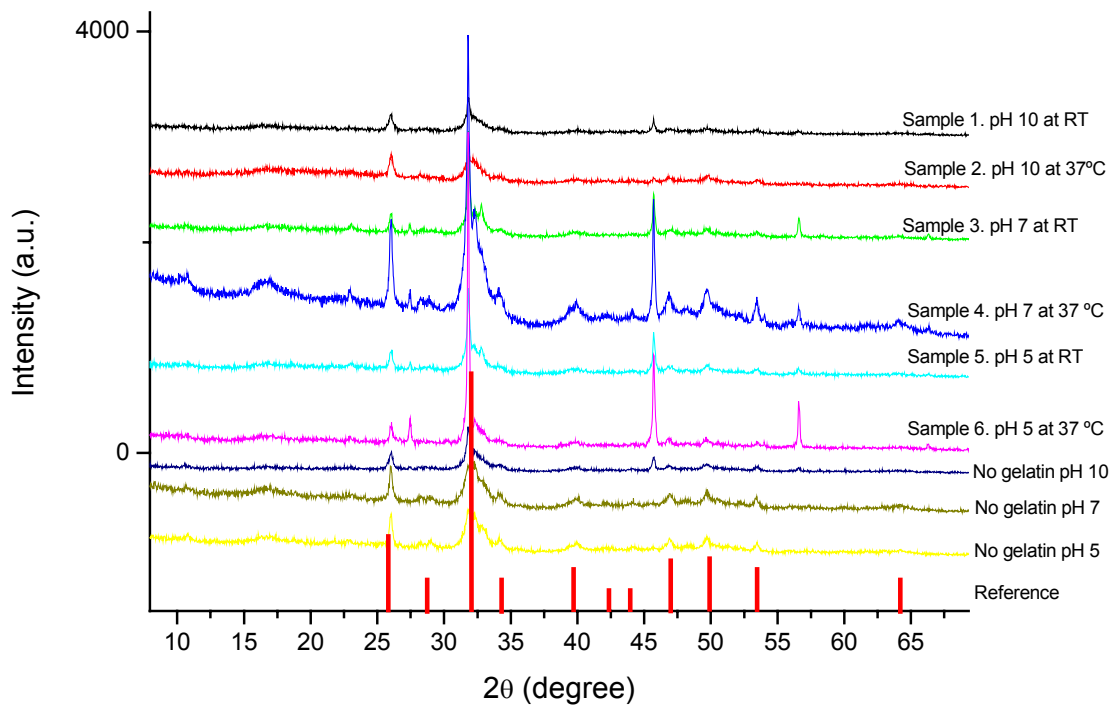


Figure 4.25. WAXS pattern of the different samples.

Figure 4.26 shows a TEM picture of sample 3. The whiskers can growth and interconnect in a drying process.

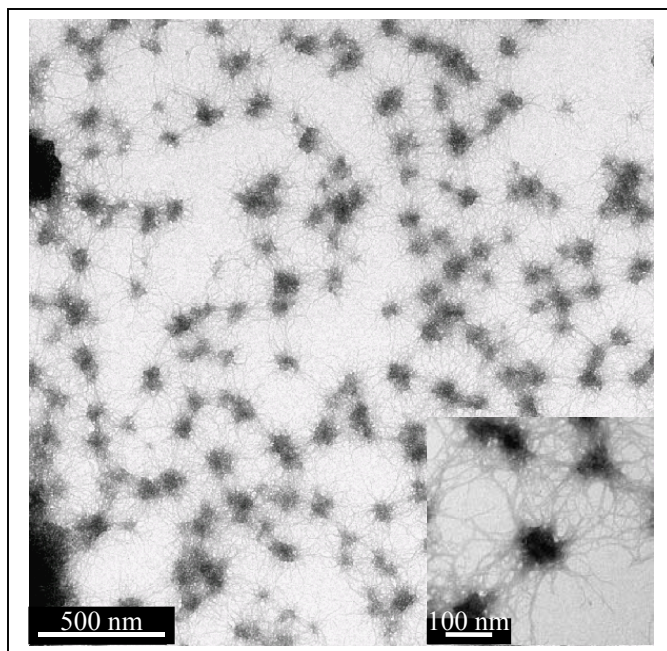


Figure 4.26. TEM picture of sample 3. Whiskers pattern of the HAP.

The whisker-like pattern for HAP has been also reported by Antonietti et al.,^[172] by using double-hydrophilic block copolymers. Although the structure is very similar, it seems to be that the mechanism of the whiskers formation in gelatin particles is different. The method of crystal growth and morphology control with the use of double-hydrophilic block copolymers is based on the design of the block copolymer. While one hydrophilic block is designed to interact with the appropriate inorganic salts and surfaces, the other hydrophilic block is designed to promote the dissolution in water without strongly interacting with the inorganic precipitate or soluble precursors. The interaction between one of the blocks and a specific face of the crystal promotes the blocking of the crystal growth in this particular face. Thus the growth happens in the free faces of the crystal.

However in our case, the development of HAP whiskers in the gelatin nanoparticles seems to be different. We believe that a second coarsening mechanism takes place, e.g. the HAP nanocrystals orient themselves one by one in the more energetic face via an attachment approach promoting the growth in one direction and therefore forming the long whiskers. A similar trend is also reported by Penn et al.^[173] for the case of anatase TiO_2 particles.

HAP is one of the most biocompatible ceramics because of its significant chemical and physical resemblance to the mineral constituents of human bones and teeth.^[174] Therefore it is widely used in orthopaedic and dental applications, however the usual synthetic HAP powders used for such applications have always exhibited a low fracture toughness of $\sim 1 \text{ MPa}\cdot\text{m}^{1/2}$ in contrast to the values observed for human bones which are in the range of 2-12 $\text{MPa}\cdot\text{m}^{1/2}$.^[126] For that reason, whiskers might be considered as a way of improving the fracture toughness of HAP bioceramics.^[174]

It is expected that the use of improved gelatin particles lead to even better results for the preparation of hybrid particles.

4.4 Semiconducting polymer nanoparticles

The research about semiconducting polymers has increased drastically since the first observation in 1977 of the electrical conductivity in doped polyacetylene. Since then many new polymers have been synthesized, however the focus has shifted to the semiconducting properties of those polymers.

The use of this new class of polymers in the fabrication of organic light emitting diodes (OLED), transistors, lasers, solar cells, etc. has become a very popular. However those polymers are synthesized in solution and are soluble in organic media only, what limits its further processing for the fabrication of electronic devices. Therefore the aim of this section is the development of a new method, based on the combination of miniemulsions and artificial latex concept, which allows one to obtain aqueous polymeric dispersions of those semiconducting polymers.

Those dispersions show several advantages over the typical solution from organic solvents, such as environmentally friendly, easily processed, capable of inject printing, as well as having good thickness control. Furthermore the formation of blends from polymers with complementary properties (e.g. electron donor and acceptor, etc) is possible, where the phase separation is well controlled in the nanometer range. This can lead to higher efficiency, as it will be shown by the energy transfer experiments.

The fabrication of an organic light emitting diode (OLED) from an aqueous semiconducting polymer dispersion here prepared will also be shown.

This work is a result of close collaboration between our group, which prepared the aqueous semiconducting polymer dispersions, the group of Prof. Ullrich Scherf at University of Wuppertal, responsible for the synthesis of the polymers, the group of Prof. Dieter Neher at University of Potsdam, where the PhD student Thomas Kietzke has performed the measurements and studies concerning optical and electrical properties presented here, and the group of Emil List of Graz University.

4.4.1 Semiconducting polymer aqueous dispersions^[175]

For the preparation of the aqueous semiconducting polymer we have combined the miniemulsion approach with the artificial latex concept as illustrated in the Figure 4.27. The polymer is dissolved in chloroform forming a homogeneous phase, which is

emulsified in the SDS aqueous solution. After the preparation of the miniemulsion via ultrasound, the solvent is evaporated. Thus the aqueous semiconducting polymer dispersion is obtained.

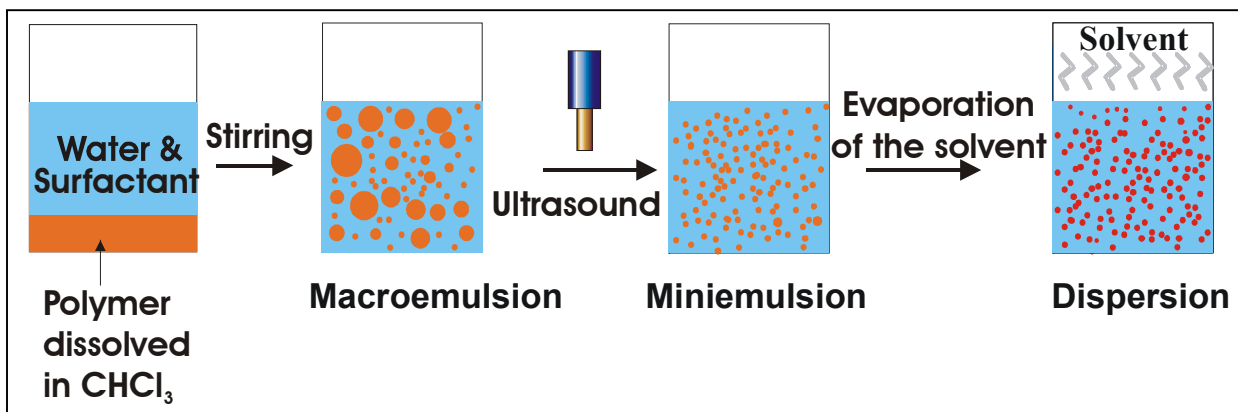


Figure 4.27. Method for the preparation of aqueous semiconducting polymer dispersions.

The structure formulas of the semiconducting polymers used in this work are given in Figure 4.28; characteristics of the aqueous dispersions are summarized in Table 4.8. Using Me-LPPP as polymer, SDS concentrations of as low as 0.71 % related to the polymer solution (RM114, 5.4 % polymer in chloroform) were sufficient in order to obtain miniemulsions with stable droplets in which the polymer itself as an absolutely water-insoluble material acts as a perfect ultrahydrophobe and therefore suppresses efficiently Ostwald ripening between the formed droplets. Due to the high stability of each droplet, evaporation of the solvent does not lead to any change of the droplet number. After evaporation of the chloroform, stable polymer dispersion with a solid content of 5.6 % and a polymer particle size of about 150 nm was obtained. It is well known for the formation of miniemulsions that with increasing amount of SDS related to the dispersed phase, the droplet size can easily be decreased. The final particle size of the polymer particles after evaporation of the chloroform also depends on the amount of polymer formally dissolved in the chloroform. By increasing the SDS amount to 1.83 %, the polymer particle size could be decreased to 75 nm. Particles were also obtained by miniemulsifying polyfluorene solutions in water. As low as 0.5 to 0.62 % of SDS allowed the formation of stable miniemulsions and after evaporation stable dispersions consisting

of low T_g (RM163) or high T_g (RM286) polymer particles. Due to a lower polymer concentration the particle size after evaporation is smaller than in the case of RM114.

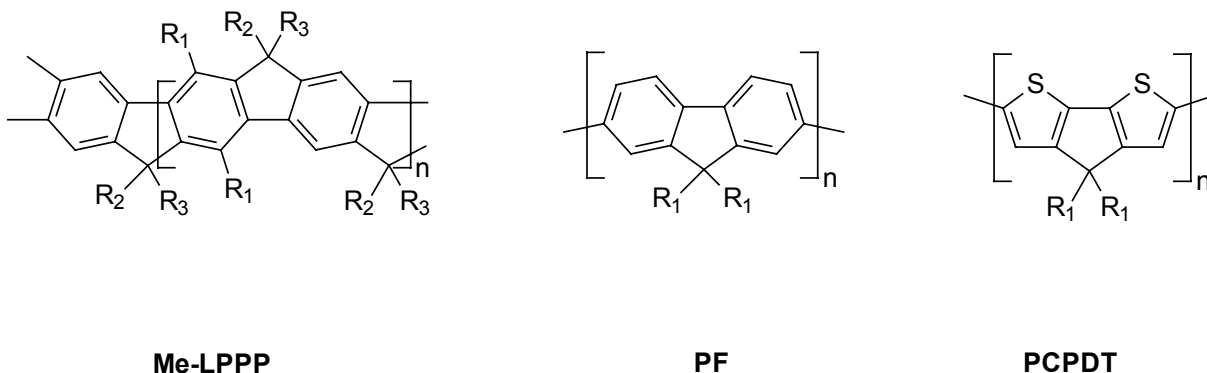


Figure 4.28. Chemical Structure of Me-LPPP (-R₁: hexyl, -R₂: methyl, -R₃: 4-decylphenyl), PF (-R₁: alkyl: 2-ethylhexyl – PF2/6, and 3,7,11-trimethyldodecyl - PF11112, respectively), and PCPDT (-R₁: 3,7-dimethylcloctyl).

Table 4.8 Characteristics of the aqueous dispersions consisting of different conjugated semiconducting polymers in 10 g of water.

Sample	Polymer	Mass of polymer (mg) % in CHCl ₃	CHCl ₃ (g)	SDS (mg) % compared to CHCl ₃	Solid content (%) after evaporation	Particle size (nm)
RM114	Me-LPPP	226 (5.4 %)	4.2	30 (0.71 %)	5.6	154
RM245	Me-LPPP	208 (4.2 %)	5.0	42 (0.84 %)	4.8	95
RM262	Me-LPPP	150 (5.0 %)	3.0	55 (1.83 %)	2.5	75
RM163	PF11112	222 (3.7 %)	6.0	30 (0.5 %)	9.3	120
RM116	PF11112	90 (3.0 %)	3.0	30 (1.0 %)	7.3	74
RM286	PF2/6	141 (2.1 %)	6.7	42 (0.62 %)	2.3	104
RM153	PCPDT	75 (1.5 %)	5.0	30 (0.6 %)	2.2	250

In Figure 4.29, a droplet of a polyfluorene dispersion is shown, once taken in white light (Figure 4.29a) and once where it was illuminated only with a UV lamp ($\lambda_{\text{max}} = 365 \text{ nm}$) (Figure 4.29b), which illustrates nicely the fluorescence behavior of the dispersion.

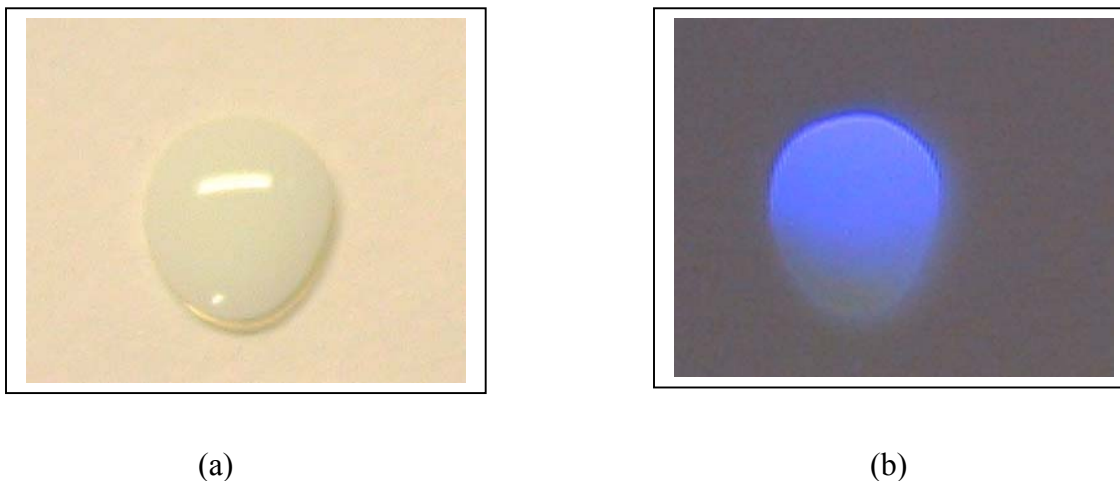


Figure 4.29. Photographs of a droplet of a dispersion of polyfluorene nanoparticles, taken either in white light (a) or when illuminated only with an UV lamp (b) ($\lambda_{\text{max}} = 365 \text{ nm}$).

In Figure 4.30a a TEM picture of a dispersion with Me-LPPP particles (sample RM116) shows spherical and, due to their high T_g , hard particles. It has to be mentioned that for this measurement, the dispersion is highly diluted leading to isolated clusters of particles. Homogeneous layers could be prepared by spincoating the dispersion with the negatively charged particles at the concentration as listed in Table 4.8 onto a glass substrate. The resulting films consist of closely packed particles, as seen by AFM, but the micrographs do not reveal any cracks within an area of $5 \times 5 \mu\text{m}^2$ (Figure 4.30b). Because Me-LPPP has its glass transitions temperature well above the onset of decomposition (300-350 °C), the particulate structure also does not change during annealing at 200 °C for 2 h.

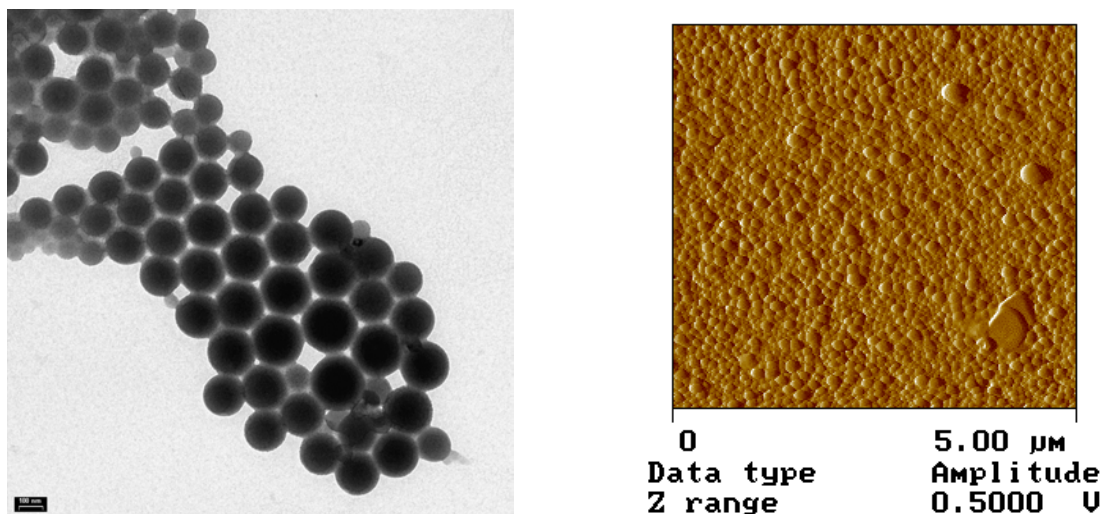


Figure 4.30. a) TEM picture of Me-LPPP particles; b) AFM of a film formed by spincoating a Me-LPPP dispersion

Large homogeneous layers of Me-LPPP could be prepared by taking advantage of the negative charge of the particles. It had recently been shown that well-defined layers of negatively charged CdS nanocrystals can be formed on polycationic films via spincoating.^[176] Layers of Me-LPPP particles (sample RM245, particle size 95 nm) coated on poly(allylamine hydrochloride) (PAH) exhibit a homogeneous fluorescence over large areas as shown in Figure 4.30a. Further, the absorption and photoluminescence (PL) emission spectra recorded on these films (Figure 4.31b) as measured by T. Kietzke [PhD thesis in preparation] are identical to those reported for layers of Me-LPPP from organic solvents.^[136,137] Since photoluminescence is very sensitive to defects, this result indicates that neither the preparation nor the deposition of the nanoparticles disturbs the principle electronic and optical properties of the conjugated polymers.

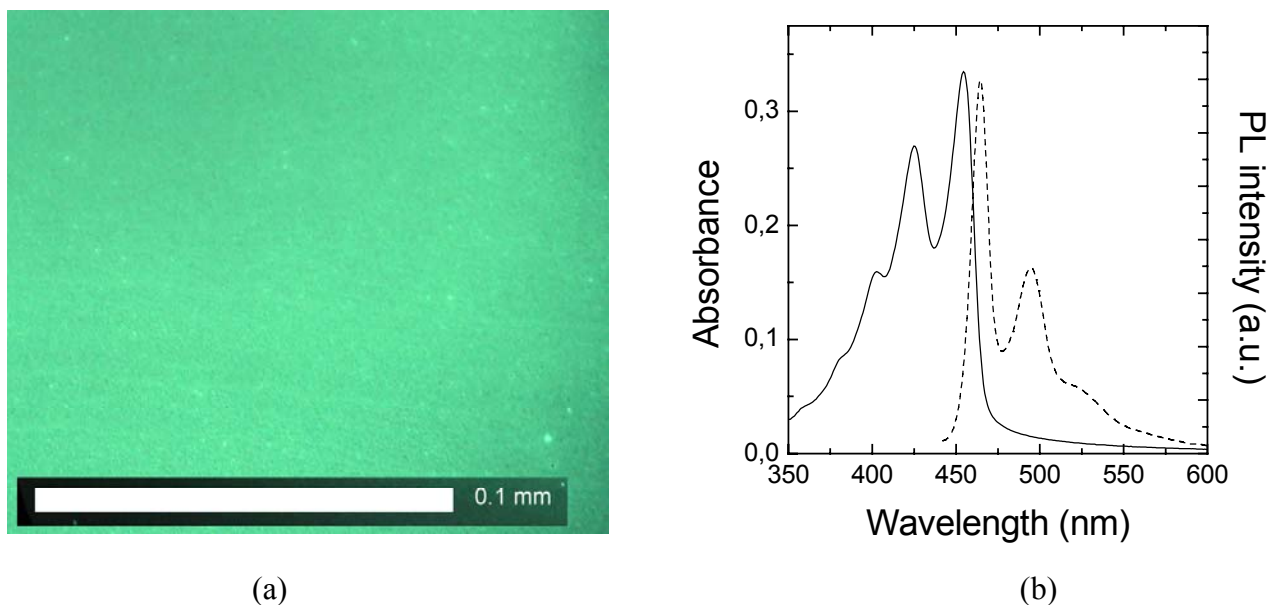
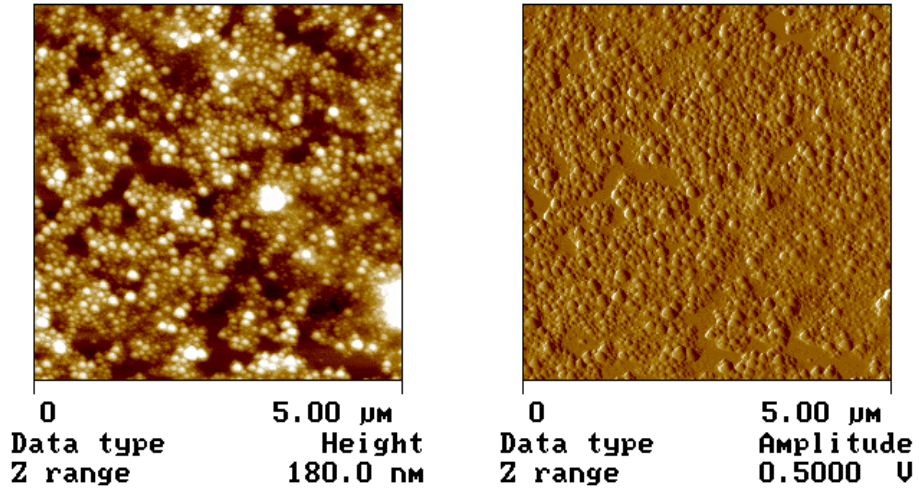
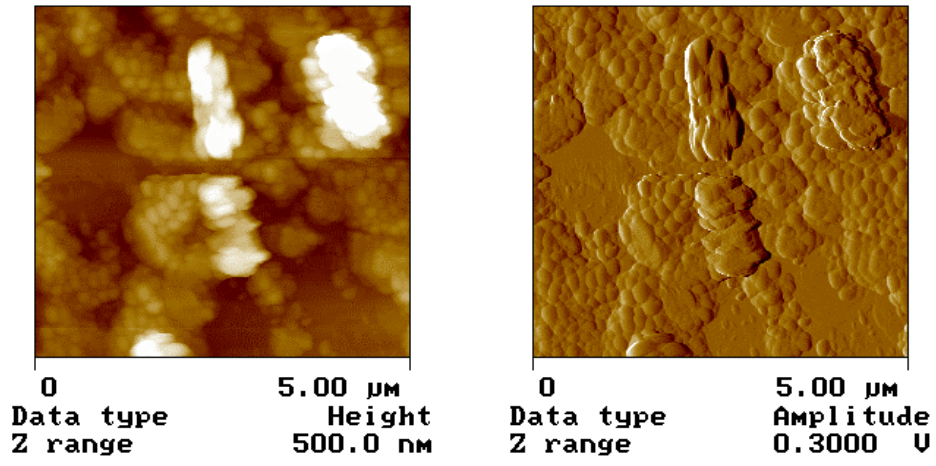


Figure 4.31. a) Photoluminescence micrograph of a Me-LPPP layer deposited from a nanoparticle dispersion on a thin polycationic PAH layer. b) absorption and photoluminescence spectrum of the layer in a).

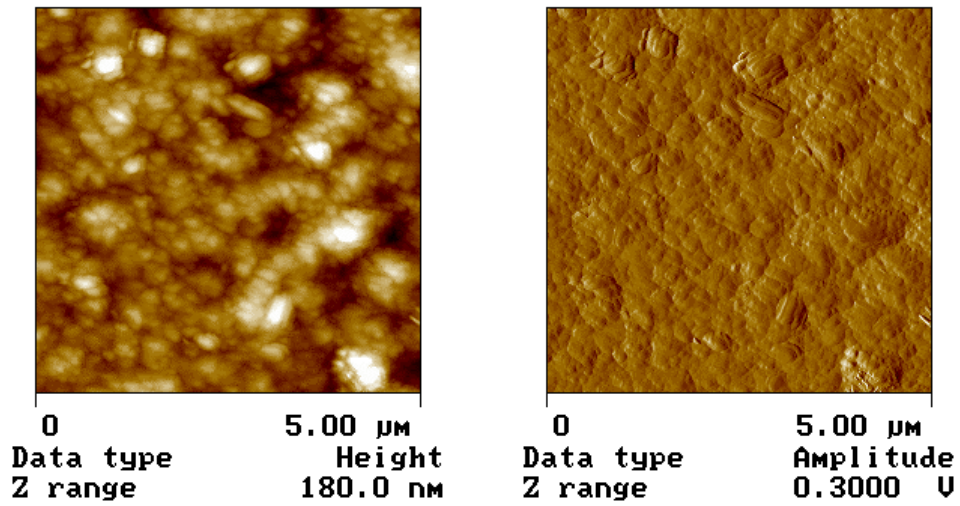
Homogeneous layers have also been prepared from dispersions of polyfluorene particles. In case of PF2/6 with a softening temperature at ca. 90 °C the particle structure can be well preserved and detected in the deposited layers (Figure 4.32a). But in contrast to Me-LPPP, annealing of these layers above T_g at 200 °C for 2 h (transition into the birefringent fluid (nematic) LC phase at ca. 170 °C, isotropization at >280 °C^[177]) results in coalescence of particles, and larger structures are formed (Figure 4.31b). This film formation shows remarkable characteristics, which are untypical for usual latex film formation: (a) the particle sizes grow, steps are built and (c) anisotropic structures can be detected resulting from the LC behavior of the polymer. When films are formed from the low T_g polyfluorene (PF11112,^[178] T_g below room temperature) nanoparticles (RM116), the particles already coalesce during film formation at room temperature, the sizes of the particles as found in the dispersion are not reflected in the film study, anisotropic structures are seen and the film exhibits also a lower surface roughness (Figure 4.30c). After annealing at 200 °C for 10 h, the surface roughness even decreases.



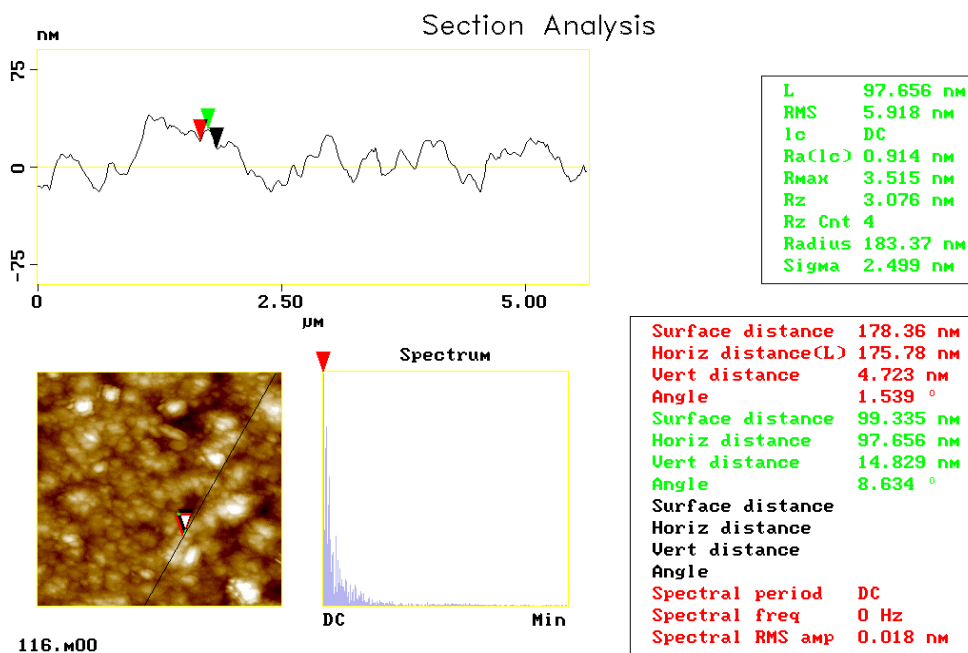
(a)



(b)



(c)



(d)

Figure 4.32 a) AFM of a film of the high T_g polymer (PF2/6) particles before annealing (sample RM286); b) AFM of the film of a) after annealing; c) AFM of a film of the low T_g polymer (PF11112) particles before annealing (RM116); d) section analysis of the film of c).

4.4.2 Fabrication of an Organic Light Emitting Diode (OLED)^[179]

For the fabrication of an organic light emitting diode is necessary to obtain a homogeneous layer from the semiconducting polymer aqueous dispersion. It is known from the literature, that the quality of the nanoparticle layers prepared from aqueous dispersions depends strongly on the wetting of the substrate, the spinning speed and the concentration of the emulsion.^[180] For low spinning speeds the film consisting of domains of multilayers will be formed, but with an irregular variation in thickness across the sample surface. If the spinning speed is too high, a monolayer will be formed, but the coverage will be not complete. However, within a certain range continuous monolayers of closely packed particles voids can be deposited. In our case, the best results could be

obtained with plasma-cleaned substrates, spinning speeds in the range of 3000-5000 RPM and solid contents of the dispersions of 4-6 wt.%. No significant differences have been observed for the different particle sizes.

To have a better view of the layer formed by spin casting of the semiconducting polymer dispersion, a film prepared from the sample RM245 (Me-LPPP, particle size 95 nm), was partially removed by scratching the surface. As seen in the Figure 4.33 a monolayer is formed and the thickness of the layer is controlled by the particle size.

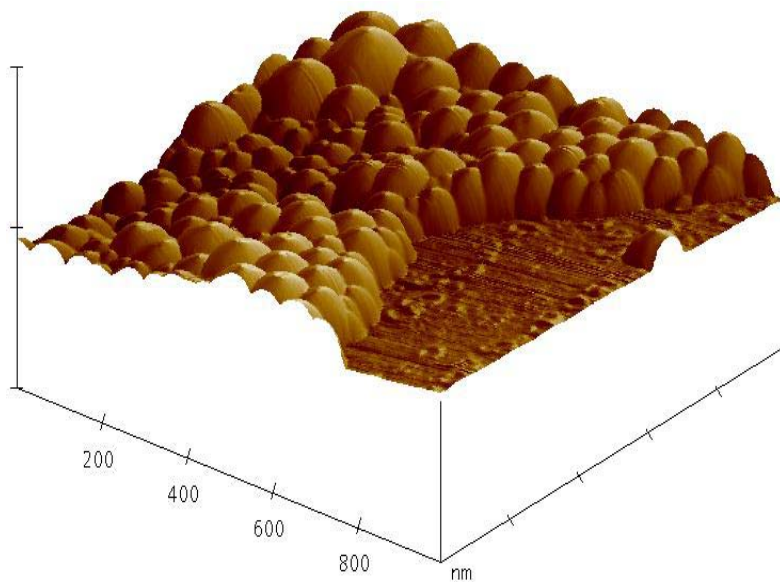


Figure 4.33. 3D AFM picture of a monolayer deposited on glass substrate from the sample RM245 (MeL-PPP, particle size 95 nm), where part of the material has been removed.

Light emitting diodes typically consist of a thin layer of our semiconducting polymer dispersion spin coated on a thin layer of poly(3,4-ethylenedioxy-thiophene)-polystyrene-sulfonic acid (PEDOT/PSS), which is one the most successful conducting polymer systems, also deposited by spin casting. The two layers are sandwiched between two electrodes, namely an indium tin oxide (ITO) layer, which is a transparent conductor, and aluminum as shown in the Figure 4.34.

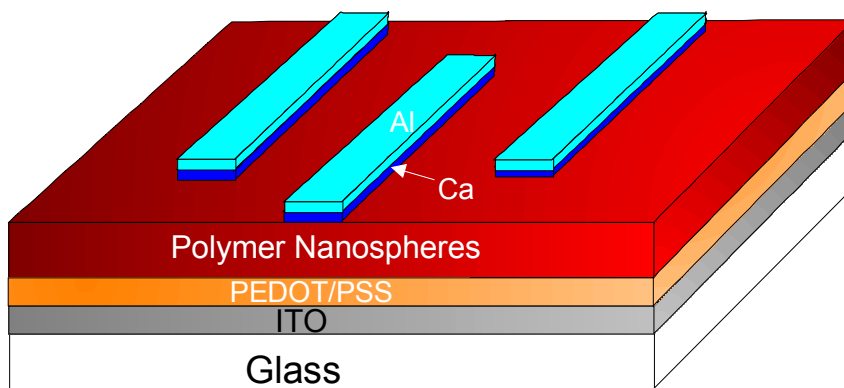


Figure 4.34. Scheme of an Organic Light Emitting Diode (OLED).

As shown in the Figure 4.35, devices fabricated from the semiconducting polymer dispersion (RM245) exhibit light emission and current onset at the single particle energy gap of the conjugated polymer at approximately 3 V in forward bias direction. The rather low electroluminescence onset in forward bias direction indicates the formation of a well-defined interface between the electro active polymer monolayer and the deposited metal cathode. Note that the formation of a well-defined interface has been found to be a key issue for achieving low onset voltages.^[181]

Taking in account that the surfactant (sodium-dodecylsulfate, SDS) used to stabilize the dispersion, could lead to electrochemical doping effects on the polymer layer and subsequent lowering of the onset voltage as observed in light emitting electrochemical cells.^[182] A sample was dialyzed and used for the preparation of an OLED to test the influence of the surfactant. However one can see that such electrochemical doping effects, if present, have only an inferior influence on the electrical characteristics. Moreover, both kinds of devices reveal a very similar maximum brightness of up to 145 Cd/m² at 8 V. On the other hand, a lot of the devices prepared from the dialyzed semiconducting polymer dispersions suffered from short circuits related to pinholes that could be observed by microscopic investigations of these films, which clearly qualifies the dispersions containing residual SDS (Figure 4.35a) of higher quality over dialyzed dispersions (Figure 4.35b) for the formation of films.

This experiment shows that in miniemulsification, the surfactant is used in a very efficient and optimal amount, which allows pinhole-free coatings.

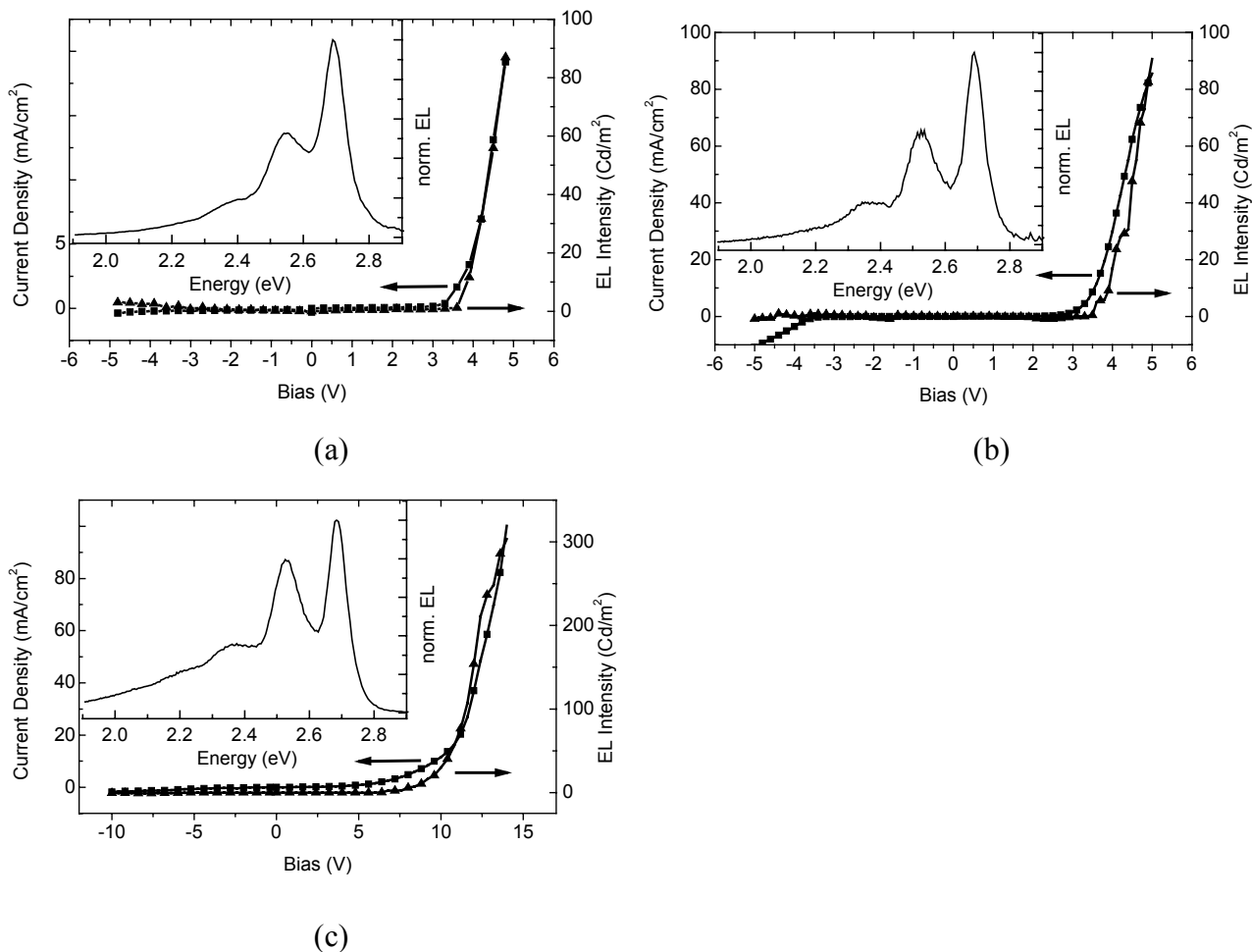


Figure 4.35. a) I/V (squares) and EL/V (triangle) characteristics of an OLED prepared from the sample RM245 (MeL-PPP, with a mean diameter of 95 nm) with SDS, the inset shows the electroluminescence emission spectrum of the OLED at a bias of 5 V. b) Dialyzed sample, the inset shows the electroluminescence emission spectrum of the OLED at a bias of 5 V. c) OLED prepared from regular Me-LPPP dissolved in Toluene, the inset shows the electroluminescence emission spectrum of the OLED at a bias of 12 V.^[179]

From the Figure 4.35, one can also see that the polymer dispersions (Fig. 4.35 a and b) has improved opto-electronic characteristics (lower onset, slightly higher efficiency)

compared with traditionally fabricated OLEDs for which the active layer is casted from a solution of the conjugated polymer in an organic solvent (Fig. 4.35c). We attribute this behavior to an enhanced electron injection from the cathode as a consequence of an *in-situ* formation of a stalactite type nanostructured cathode during aluminum evaporation. Figure 4.36 shows a photograph of such an OLED fabricated from a MeL-PPP aqueous dispersion. The emission occurs homogeneously across the layer and no black spots due to an inhomogeneous coverage by the semiconducting polymer monolayer can be observed.

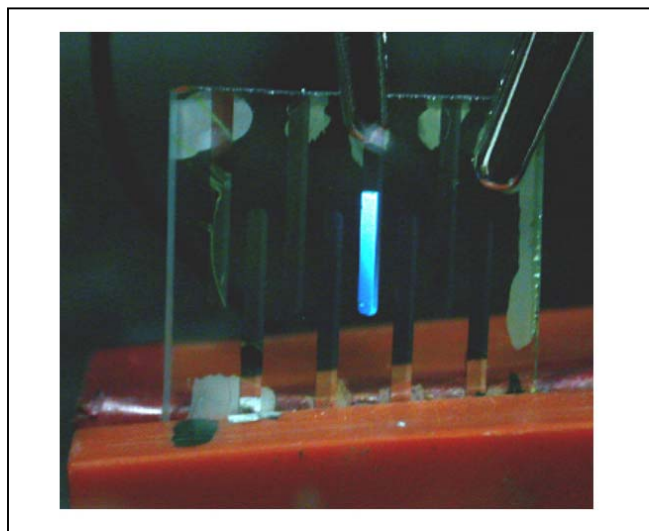


Figure 4.36 Photograph of an OLED prepared from a MeL-PPP aqueous dispersion.^[179]

4.4.3 Blends of semiconducting polymers^[183]

Here we show that it is possible to apply the miniemulsion technology to prepare blends of polymers, in which the lateral dimension of phase separation in thin layers is precisely controlled by the diameter of the nanospheres. Two different approaches are presented, utilizing semiconducting fluorescent polymers, and energy transfer is applied to probe the morphology of the nanophase-separated structures. In the first approach, two types of single component nanospheres are mixed to form a layer where the dimension of phase separation is expected to be in the range of the diameter of the nanospheres. In the second approach, nanospheres were prepared where each particle contained both polymers. In this case the phase separation occurs inside each particles, and therefore the dimension of

phase separation is smaller than the particle size (see Figure 4.37). Even though the results presented here were obtained for spincoated layers and dilute emulsions, it should be possible to utilize these nanoparticles to fabricate multicomponent polymer bulk samples.

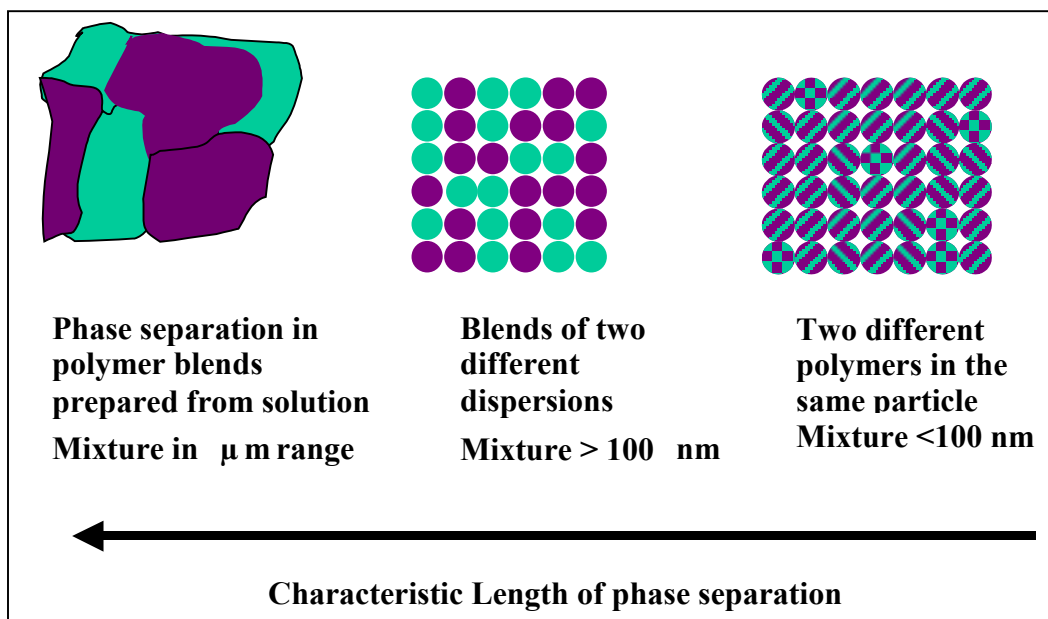


Figure 4.37. Strategies to prepare binary polymer blends utilizing polymer nanoparticles: In contrast to conventional polymer blends, which tend to phase-separate on the macroscopic scale, phase separated structures at the nanometer scale can be prepared either by mixing two polymer nanoparticle dispersions or by forming the miniemulsion from a solution containing both polymers.

Here, two alkyl-substituted polyfluorene derivatives, poly(9,9-bis(2-ethylhexyl)fluorene-2,7-diyl) (PF2/6) and poly(9,9-bis(3,7,11-trimethyldodecyl)fluorene-2,7-diyl) (PF11112), and Me-LPPP, a solution-processable poly(*para*-phenylene)-type ladder polymer, have been used. Fluorescence studies on our blends will, therefore, be indicative of any significant alterations of the polymers' physical and chemical structure during layer processing. As shown in Figure 4.38 there is a good overlap of the PF emission and the Me-LPPP absorption, which later will be utilized for energy-transfer experiments. Also,

the shapes of the spectra as well as the positions of the peaks compare well to those measured on layers of the pure components deposited from organic solvents,^[136,184] proving that the preparation of the nanoparticle dispersions does not affect the electronic structure of the polymers. The two derivatives of polyfluorenes were chosen because of their different softening temperatures, which is near room temperature for PF11112 and ca. 90 °C for PF2/6. Me-LPPP does not show any softening up to the decomposition temperature of ca. 300 – 350 °C.

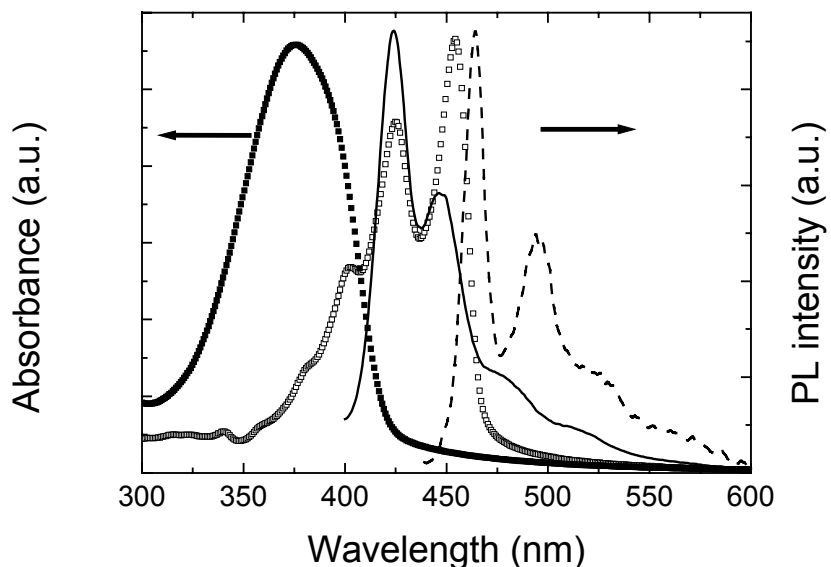


Figure 4.38. Absorption (symbols) and photoluminescence (lines) spectra of a PF2/6 layer (solid symbols and solid line) and a Me-LPPP layer (open symbols and dashed line) deposited from nanoparticles dispersions on glass.^[183]

In the first approach, dispersions of single component nanoparticles (see Table 4.9) were prepared from PF2/6 (mean diameter of the particles $d_m = 153$ nm), PF11112 ($d_m = 74$ nm) and Me-LPPP ($d_m = 95$ nm) by the miniemulsion process. After that the PF dispersion was mixed with the Me-LPPP dispersion at a 1:1 ratio. From this mixed dispersion, homogenous monolayers were deposited by spin coating the aqueous dispersion at spinning speeds of 4200RPM on glass substrates.

Table 4.9. Dispersions with nanoparticles consisting of homopolymers and of polymer mixtures (1:1 ratio).

Polymer 1	Polymer 2	Particle size (nm)
Me-LPPP	-	95
PF11112	-	74
PF2/6	-	153
PF2/6	Me-LPPP	149
PF2/6	Me-LPPP	64

Figure 4.39a shows an AFM picture of a layer prepared from a mixture of low T_g PF11112 and Me-LPPP nanoparticles with a 1:1 weight ratio of the two polymers. The resulting film consists of closely packed nanospheres, and the micrograph does not reveal any cracks within an area of $3 \times 3 \mu\text{m}^2$. Obviously, some of the particles already coalesce upon layer formation, which we assign to the low T_g of the PF11112 nanoparticles. In order to investigate how the Me-LPPP and the PF particles are distributed in the layer, the samples were annealed for 1 h under vacuum. Because of the softening temperatures of the two polymers we expected that the PF 11112 particles would form a homogeneous not-structured phase while the Me-LPPP nanospheres will maintain their original shape. This is proven by the AFM micrographs in Figure 4.39b and 4.39c. The micrograph obtained after annealing for 1 h at 200 °C shows small features, homogeneously distributed within a flat homogeneous layer. The actual size and heights of these features is smaller than the average diameter of the Me-LPPP, which is due to the fact that the particles are protruding into the PF layer, such that only the top portion of the Me-LPPP spheres sticks out from the PF phase. Obviously, the Me-LPPP particles do not agglomerate but appear to be randomly distributed within a continuous PF phase.

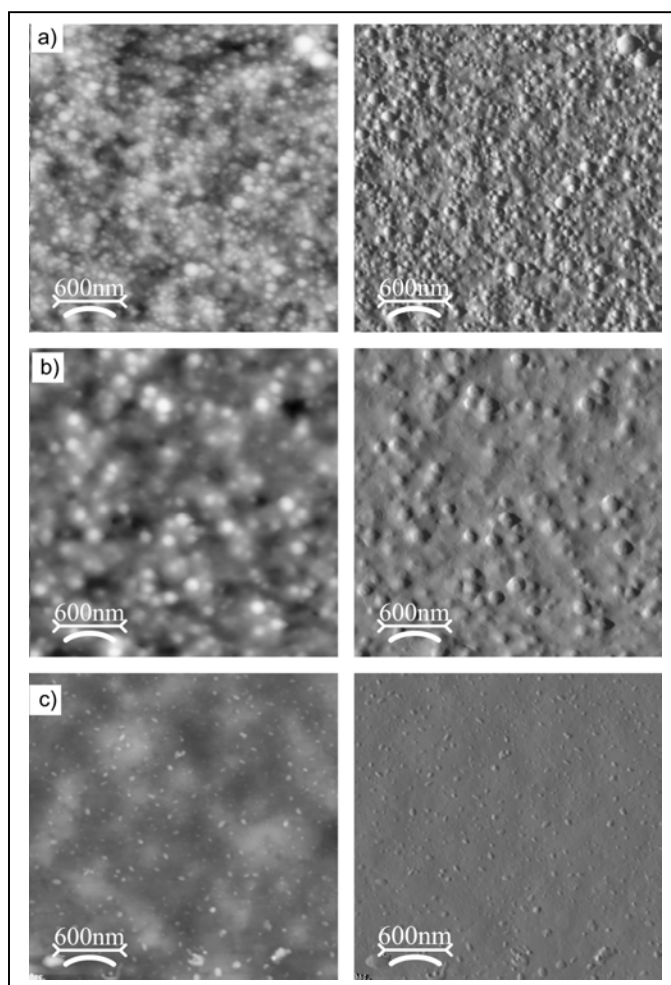


Figure 4.39: AFM picture of a film prepared from a 1:1 mixture of particles of the low T_g polymer (PF11112) and the high T_g polymer (Me-LPPP), a) before annealing, b) after annealing at 150 °C for 1 h, and c) at 200 °C for 1 h. The height picture is shown left, the amplitude picture on the right.

These observations are confirmed by energy transfer experiments as done by T. Kietzke [PhD thesis in preparation]. As the rate of energy transfer strongly depends on the distance between donor and acceptor moieties, this process has been extensively utilized to study the morphology of polymer blends.^[185] In the case of semiconducting polymers, the process will include exciton migration within one phase as well as Förster-type energy transfer between the two components. Samples were optically excited at the

wavelength of 380 nm, where the PF shows its maximum absorption but the Me-LPPP has only little absorption (see Figure 4.38). Figure 4.40a shows the PL spectrum of an as-prepared layer deposited from a 1:1 mixture of PF11112 and Me-LPPP nanoparticles. The PL emission of the PF is partially quenched, due to energy transfer from PF to Me-LPPP, which can be clearly identified by the Me-LPPP emission peaks at 463 nm and 492 nm. Upon annealing at 200 °C, the PF11112 emission is nearly completely quenched whereas the Me-LPPP peak has gained a fourfold intensity. At this stage, the PF11112 phase homogeneously surrounds the individual Me-LPPP particles, resulting in a large interface between the polyfluorene and Me-LPPP phases. For comparison the Me-LPPP emission intensity caused by direct absorption of photons is shown in the Figure 4.40b, proving that the Me-LPPP contribution in the PL spectrum of the mixed layer mainly originates from energy transfer. The absorption spectra in the inset prove that none of the components degraded upon annealing. The fact that the decrease in PF emission intensity is accompanied by an increase of the Me-LPPP emission is further proof that annealing does not lead to any significant changes in the structure of one or both components. Rather than that, annealing improves the energy transfer between the PF and the Me-LPPP phase due to morphological changes in the two components blend.

In comparison to that, as-prepared layers of PF2/6 and Me-LPPP (1:1 mixture) exhibit only weak energy transfer (Figure 4.40b). The rather low energy transfer in the PF26/Me-LPPP blend has mainly two origins: since both polymers have a softening temperature well above RT, the nanoparticles maintain their spherical shape, resulting in a monolayer of individual spheres. Also, the mean diameter of the PF2/6 nanoparticles is almost twice of that of the PF11112 particles and exciton diffusion to the surface of the spheres is less efficient in this case. After annealing the layer at 150 °C, well above the softening temperature of PF2/6, quenching of the PF emission due to the energy transfer to the Me-LPPP phase becomes more pronounced, comparable to that in the as-prepared layer of PF11112:Me-LPPP. This is due to the formation of a continuous PF phase.

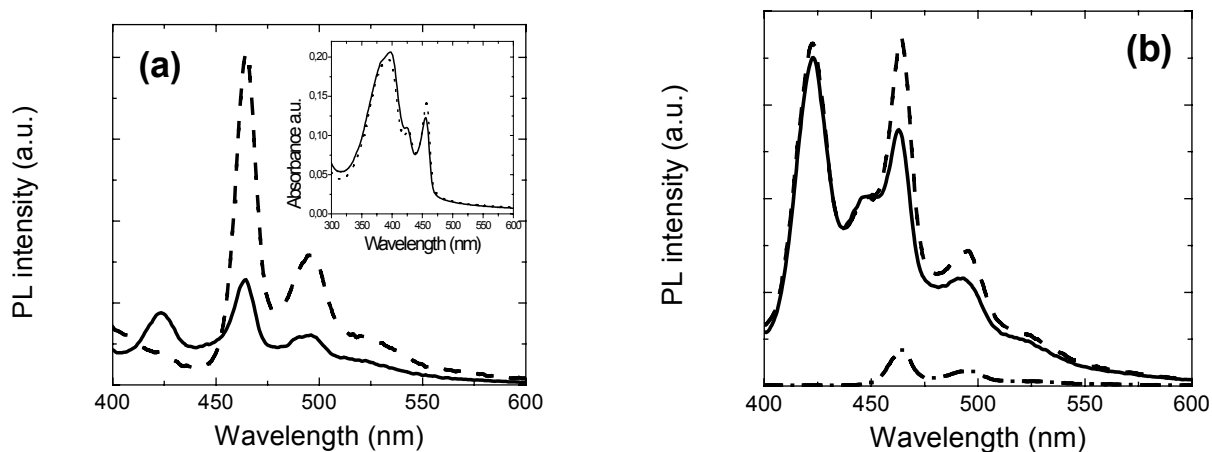


Figure 4.40. Photoluminescence spectra of layers prepared from 1:1 mixtures of a, Me-LPPP and PF11112 nanoparticles and b, Me-LPPP and PF2/6 nanoparticles on glass substrates. Data are shown for the as-prepared layers (solid lines) as well as for the same layers after annealing in inert atmosphere (dashed lines). The annealing temperatures were (a) 200 °C and (b) 150 °C, respectively. The excitation wavelength was 380 nm. Also shown is the emission spectrum of a Me-LPPP layer (dashed-dotted line) excited under the same conditions as the mixed layers. The inset in (a) shows the absorption of the Me-LPPP/ PF11112 layer before (solid line) and after annealing (dashed line).

In the second approach, miniemulsions were prepared starting from a solution containing two polymers in a common solvent. We expected that after evaporation of the solvent the resulting nanoparticles would contain a blend of both polymers phase separated inside the particles. As an example, a dispersion prepared by the miniemulsion process from solutions of PF2/6 and Me-LPPP at weight ratios of 1:1 was studied. Particles with different diameters were prepared to investigate the influence of the particle size on the energy transfer. Figure 4.41 shows the PL spectra of two highly diluted dispersion containing nanoparticles with mean diameters of 64 nm and 149 nm, respectively. The relative peak ratio of the Me-LPPP PL compared to the PF emission increases from 1.1:1 for the particles with 149 nm in diameter to 4.4:1 for the 69 nm particles. The significant

Me-LPPP emission clearly proves that both polymer components must be present in the individual particles. We insured that the generation and reabsorption of PF fluorescent light in different particles do not cause the Me-LPPP emission by comparing the shape of PL spectra measured at different concentrations, down to ca. 10^{-5} wt.% (Figure 4.42). The fact that the Me-LPPP emission is larger for the smaller particle further indicates that the two polymers are not homogeneously mixed within the nanospheres. Even though we have not further studied the process of particle formation we presume that phase separation occurs at the stage of solvent extraction, with the domain size controlled by the diameter of the particles.

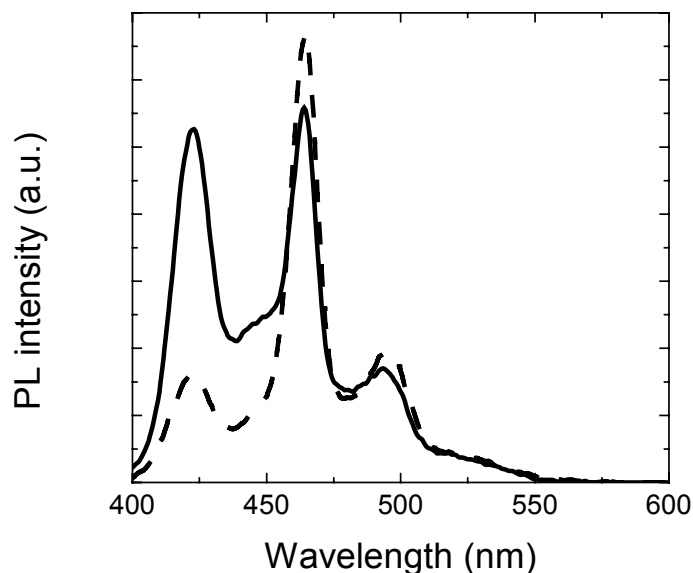


Figure 4.41. PL spectra of diluted dispersions of nanospheres containing Me-LPPP and PF2/6 in a weight ratio 1:1. Data are shown for nanoparticle dispersions with a mean particle diameter of 64 nm (dashed line) and 149 nm (solid line). The excitation wavelength was 380 nm.

At this point we acknowledge that, in principle, two component polymer blend layers can also be formed by nanoparticles prepared via emulsion polymerisation.^[186] Further, two-component polymer nanoparticles with core-shell morphologies are routinely made in two-step reactions using this synthetic approach.^[187] However, this type of heterophase polymerization is limited to the radical polymerization of a set of barely water-soluble monomers such as (meth)acrylates and styrene. The so-produced polymer particles are the product of a kinetically controlled growth and are built from the center to the surface, where all the monomer has to be transported by diffusion through the water phase. Thermodynamically driven structures in nanoparticles can be obtained by using the process of miniemulsion polymerization. In this case small, homogeneous, and stable droplets of monomer or polymer precursors are directly transferred by (as many as possible) polymer reactions to the final polymer latexes, keeping their particular identity without serious exchange kinetics involved. Here, a larger choice of monomers can be used in the case of the polymerization in miniemulsion, which is not also limited to radical polymerisation, but also allows one to perform polyaddition and polycondensation reactions in heterophase. However, no polymerisation in heterophases has yet been applied to functional polymers. A major drawback of the application of this approach to functional polymers is that polymerization catalyst will remain imbedded in the solid polymer nanoparticles.

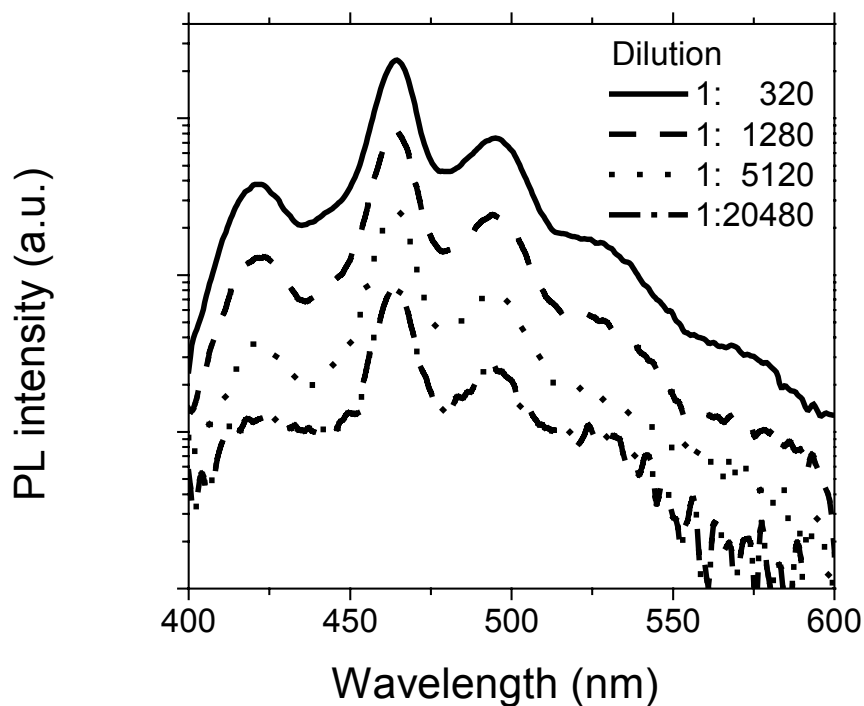


Figure 4.42. PL spectra of diluted dispersions of nanoparticles containing PF2/6 and Me-LPPP with a mean particle diameter 64 nm. The non-diluted dispersion had a solid content of 0.5 wt.%.

The miniemulsion approach applied for the preparation of the aqueous semiconducting polymer dispersions has shown very impressive results. However one still has to study in details the influence of the amount of solvent used to dissolve the polymer and the rate of evaporation, particularly for the blends of polymers in the same particle, since that can lead to different phase separation pattern. This will be subject of further investigation

5 Conclusions

In the first part of this work, dynamic crystallization and melting experiments were performed in small, stable and narrowly distributed nanodroplets of miniemulsions. Both regular and inverse systems were examined, characterizing, first, the crystallization of hexadecane, secondly, the crystallization of ice. It was shown for both cases that the temperature of crystallization in such droplets is significantly decreased (or the required undercooling is increased) as compared to the bulk material. This was attributed to a very effective suppression of heterogeneous nucleation. This means that crystallization occurs below the spinodal line, which increases the region of metastability by another 25 K.

Interestingly, it was also found that the required undercooling also depends on the nanodroplet size: with decreasing droplet size the undercooling increases. This can be understood by the approach that smaller droplets rely on smaller spinodal fluctuation of the chemical potential, which again is generated by deeper temperature quenches.

Furthermore, the confinement in droplets also influences the crystal morphology and crystal structure, as detected by X-ray analysis. The more plastic hexadecane crystals show a slight shift of the peaks and the occurrence of extra, symmetry forbidden peaks, suggesting a distortion of the crystal structure by the adaptation of an almost spherical shape. Water on the other hand shows the same hexagonal structure, but the relative peak intensities change significantly, suggesting a very flat shape of ice nanocrystals. At the same time, more than one ice crystal nucleates in each nanodroplet, making the crystalline nanodroplet superstructure potentially resembling a stack of pancakes. The nanocrystal size in the case of ice increases with decreasing droplet size, which can be due to heat flow effects, a decreased nucleation rate or from a better packing of the nanocrystals in smaller droplets.

It was shown that the temperature of crystallization of other *n*-alkanes in nanodroplets is also significantly decreased as compared to the bulk material due to a very effective suppression of heterogeneous nucleation. A very different behavior was detected between odd and even alkanes. In even alkanes, the confinement in small droplets changes the crystal structure from a triclinic (as seen in bulk) to an orthorhombic structure, which is attributed to finite size effects inside the droplets. An intermediate metastable rotator

phase is of less relevance for the miniemulsion droplets than in the bulk. For odd alkanes, only a strong temperature shift compared to the bulk system is observed, but no structure change. A triclinic structure is formed both in bulk and in miniemulsion droplets.

In the next part of the thesis it was shown how miniemulsions could be successfully applied in the development of materials with potential application in pharmaceutical and medical fields.

The production of cross-linked gelatin nanoparticles is feasible. Starting from an inverse miniemulsion, the softness of the particles can be controlled by varying the initial concentration, amount of cross-link agent, time of cross-linking, among other parameters. Such particles show a thermo-reversible effect, e.g. the particles swell in water above 37 °C and shrink below this temperature. Above 37 °C the chains loose the physical cross-linking, however the particles do not loose their integrity, because of the chemical cross-linking. Those particles have potential use as drug carriers, since gelatin is a natural polymer derived from collagen.

The cross-linked gelatin nanoparticles have been used for the biomineralization of hydroxyapatite (HAP), a biomineral, which is the major constituent of our bones. The HAP crystals biomineralized within the gelatin nanoparticles form whiskers starting from the gelatin particles. This behavior is however pH dependent. For high pH the HAP is formed, but whiskers are not present. The mechanism of whisker formation is probably due to the end-to-end fusion of HAP nanocrystals.

The biomineralization of HAP within the gelatin nanoparticles resulted in a hybrid material, which has potential use as a bone repair material.

In the last part of this work we have shown that layers of conjugated semiconducting polymers can be deposited from aqueous dispersion prepared by the miniemulsion process. Dispersions of particles of different conjugated semiconducting polymers such as a ladder-type poly(*para*-phenylene) and several soluble derivatives of polyfluorene could be prepared with well-controlled particle sizes ranging between 70 - 250 nm. Layers of these particles formed by spincoating exhibit a particulate structure, revealing the shape of the individual polymer nanoparticles. Annealing above the polymer's glass transition temperature results in the coalescence of particles, and larger domains of continuous structures are formed. It was therefore proposed that the concept of

semiconducting polymer nanoparticles will allow the formation of multilayer structures by depositing a first layer from a solution of a polymer and overcoating it by semiconducting polymer nanoparticles of the second polymer from an aqueous phase, followed by annealing and film formation. Most important, this will allow the formation of a multilayer structure from polymers, which are highly soluble in the same solvents, without introducing any additional chemical conversion steps.

The homogeneous formation of layers from the dispersions is well demonstrated (in collaboration with the group of D. Neher) by the construction of an Organic Light Emitting Diode (OLED), which exhibit light emission and current onset at the single particle energy gap of the conjugated polymer at approximately 3 V in forward bias direction. The rather low electroluminescence onset in forward bias direction indicates the formation of a well-defined interface between the electro active polymer monolayer and the deposited metal cathode. It has been shown that the preparation and processing of the aqueous polymer dispersions by the miniemulsion method does not alter the basic opto-electronic properties of materials such as m-LPPP and PF.

Layers of polymer blends were prepared with controlled lateral dimensions of phase separation on sub-micrometer scales, utilizing either a mixture of single component nanoparticles or nanospheres containing two polymers. Both approaches were demonstrated to give phase-separated structures with typical feature sizes defined by the size of the particles. In contrast to approaches published earlier, our strategy of nanostructured polymer blends does not require any chemical modification of the polymer structure. Moreover, it should be applicable to virtually any polymer material, which is soluble in an organic solvent immiscible with water. Further, blending miniemulsions of single component nanoparticles allows the formation of solid blends of polymers that are not soluble in a common solvent, thus widening the selection of possible polymer pairs.

From the results of energy transfer it is demonstrated that the blend of two polymers in the same particle leads to a higher efficiency due to the better contact between the polymers. Such an effect is of great interest for the fabrication of opto-electronic devices such as light emitting diodes with nanometer size emitting points and solar cells comprising of blends of electron donating and electron accepting polymers.

6 Experimental Section

6.1 Crystallization in miniemulsion droplets

Materials

n-Hexadecane and sodium dodecyl sulfate (SDS) from Aldrich and perfluorhexane from Fluka were used as received. The block copolymer emulsifier poly(butylene-*co*-ethylene)-*b*-poly(ethylene oxide) P(B-E)/PEO consisting of a hydrophobic block ($M_w = 3700 \text{ g}\cdot\text{mol}^{-1}$) and a hydrophilic block ($M_w = 3600 \text{ g}\cdot\text{mol}^{-1}$) was synthesized starting from Kraton L (Shell) dissolved in toluene by adding ethylene oxide under the typical conditions of anionic polymerization. Isopar M (an isoparaffinic hydrocarbon) was a gift from Exxon Chemical.^[188]

Miniemulsion preparation

Preparation of the direct miniemulsions

A 6 g sample of *n*-hexadecane and 250 mg of perfluorhexane were mixed and added to a solution of 100 mg sodium dodecyl sulfate (SDS) in 24 g of water. After stirring for 1 h, the miniemulsion was prepared by ultrasonication of the emulsion with a Branson sonifier W450 (1/2" tip) at amplitude of 90 %. To prevent a temperature rise in the sample, the emulsion was ice-cooled.

Preparation of the inverse miniemulsions

A 1 g NaCl solution (0.1 M) was added to a solution of 100 mg of poly(butylene-*co*-ethylene)-*b*-poly(ethylene oxide) P(B-E)/PEO and 10 g of Isopar M. After stirring for 1 h, the miniemulsion was prepared by ultrasonication of the emulsion with a Branson sonifier W450 at 90 % intensity under ice cooling.

6.2 Metastable phases (rotator phase) in *n*-alkanes

Materials:

Pentadecane, hexadecane and heptadecane (~99% purity) were purchased from Aldrich. Sodium dodecyl sulfate (SDS) (>98% purity) also from Aldrich. The others *n*-alkanes:

C₁₈ to C₂₄ (~98% purity) and perfluorhexane from Fluka. The compounds were used as received.

Preparation of the Miniemulsions:

The *n*-alkane (1 g) together with 50 mg of perfluorhexane (ultrahydrophobe used to suppress Ostwald ripening) was mixed with a solution of SDS (30 mg) in 10 g of distilled water. The mixture was rigorously stirred for 1 h at the melting temperature of the alkane.

After stirring for 1 h, the miniemulsion was prepared by ultrasonication of the emulsion with a Branson sonifier W450 (microtip) at amplitude of 70 %. In order to obtain different droplets sizes different sonication times were used.

6.3 Gelatin Nanoparticles

Materials:

Gelatin from porcine skin from Fluka with the following characteristics: gel strength on the Bloom scale 250, Average Molecular Weight 160 kD, PH (67 mg/ml H₂O, 25°C) 4.0 – 6.0, cyclohexan from BASF. Glutahaldehyde (50% solution in water) (cross-linking agent), and Resorcinol (antibactericidal agent) from Aldrich. The block copolymer emulsifier poly(butylene-*co*-ethylene)-*b*-poly(ethylene oxide) P(B-E)/PEO consisting of a hydrophobic block ($M_w = 3700 \text{ g}\cdot\text{mol}^{-1}$) and a hydrophilic block ($M_w = 3600 \text{ g}\cdot\text{mol}^{-1}$)^[188] was used for the preparation of the inverse miniemulsion.

Preparation of nanoparticles (inverse miniemulsion):

500 mg of gelatin were dissolved in distilled water (see Table 4.6 for exact values) at 50 °C under stirring. The pH was adjusted to 7.4 by the addition of sodium hydroxide (Aldrich).

A solution consisting of 70 mg P(B-E)/PEO in 30 g of cyclohexane was added at the same temperature (50 °C) to the gelatin solution, and then stirred for 30 min for pre-emulsification.

The inverse miniemulsion was then prepared by sonicating the mixture at 95 % of amplitude for 2 min with a Branson sonifier W450. The temperature range during sonication was between 45 and 55 °C.

A second miniemulsion with the cross-linking agent was also prepared. Here a solution consisting of 100 mg of a 50 % glutardialdehyde-solution, 100 mg resorcinol or 2.5 mg sodium azide and 500 mg of water was added to a solution consisting of 70 mg P(B-E)/PEO in 30 g of cyclohexane and sonicated at 95 % of amplitude. Then the two miniemulsions were unified and sonicated at the same previous conditions for two additional minutes carrying out the mass exchange between the gelatin and glutardialdehyde-resorcinol droplets by fission and fusion process. Such a concept of fission and fusion process have been already well described elsewhere.^[170]

The sample was brought to room temperature and slowly stirred for extra time (see Table 4.6) allowing the cross-linking reaction within the droplets.

The final inverse miniemulsion was lyophilized at 0.63 mbar and -50 °C for 10 h. From this process a beige powder was obtained.

Redispersion of the dried-cross-linked gelatin particles:

50 mg of dried-cross-linked gelatin particles were redispersed in 4 g of distilled water under stirring.

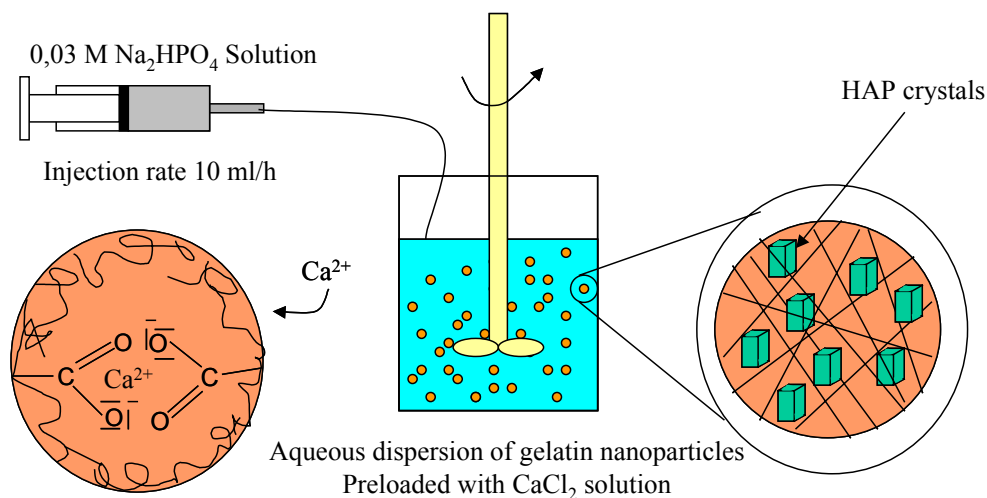
6.4 Biomineralization of HAP within gelatin nanoparticles

Pre-loading of gelatin nanoparticles:

100 mg of cross-linked gelatin nanoparticles were dispersed in 100 mg of bidestilated water at room temperature under magnetic stirring. To the dispersion was added 10 ml of 0,05 M CaCl₂ solution. The sample was stirred for 2 h to promote the pre-loading of the gelatin nanoparticles with Ca²⁺, since the gelatin chains are negatively charged due to the carboxylic groups. The pH was then adjusted to one of the studied pH, namely 5, 7 and 10.

Biom mineralization of hydroxyapatite within the gelatin nanoparticles:

The dispersion of Ca^{2+} pre-loaded gelatin nanoparticles was transferred to a reactor as shown in scheme below:



With the use of a syringe pump at injection rate of 10 ml/h, 10 ml of a 0.03 M Na_2HPO_4 solution was injected to the reactor.

6.5 Semiconducting polymer nanoparticles

Materials:

The conjugated polymers used in this work were synthesized by the group of Prof. Ullrich Scherf

- Methyl substituted ladder-type poly(*para*-phenylene) (Me-LPPP)^[189]
- poly(9,9-bis(2-ethylhexyl)fluorene-2,7-diyl) (PF2/6)^[177,190]
- poly(9,9-bis(3,7,11-trimethyldodecyl)fluorene-2,7-diyl) (PF11112)^[178,191]
- Poly(2,6-(4,4-dialkyl)-4*H*-cyclopenta[2,1-*b*:3,4-*b'*]dithiophene) (PCPDT)^[139]

Synthesis of the aqueous polymer dispersion:

The polymer was dissolved in CHCl_3 and given to an aqueous SDS solution. After stirring 1 h for pre-emulsification, the miniemulsion was prepared by ultrasonication of the mixture at 90 % amplitude until reaching the steady state of the droplet sizes as detected

by a constant turbidity of the miniemulsion (Branson sonifier W450 Digital). After sonication the sample was stirred in oil bath at 62 °C in order to evaporate the CHCl₃.

Preparation of the films:

Glass substrates were cleaned with the standard procedure. After ultrasonification in a hot mixture of H₂SO₄/H₂O₂ (7:3) for 3 h, the substrates were heated in a mixture of H₂O/H₂O₂ / NH₃ (5:1:1) at 80 °C for 1 h and dried under the purging of N₂. For a first layer a few drops of cationic PAH (10 mM) were placed on the substrate. The substrate was rotated on a spinner for 10 s with 3000 rpm. After deposition of the PAH layer the substrates were rinsed twice with plenty of MilliQ water. After that anionic LPPP (4.8 %) was deposited with the same method as described before.

Preparation of the OLED:^[179]

Commercially available ITO coated glass substrates were cleaned in a series of different organic solvents and treated with chromosulphuric acid. PEDOT/PSS as purchased from Bayer (Baytron P) was spin coated and dried according to the specifications of the distributor.

Afterwards the semiconducting polymer aqueous dispersions were spin coated, and the films were dried in an oven for about 15 min at 75 °C.

A Balzers MED010 vacuum coating unit was used for depositing the aluminum top electrodes at a base pressure of 4·10⁻⁶ mbar. The different devices were fabricated under identical experimental conditions and operated in house made sample holders in argon atmosphere. The current/luminance/voltage (I/L/V) characteristics were recorded in a customized setup using a Keithley 236 source measure unit for recording the current/voltage characteristics while the luminance characteristics were recorded using a calibrated photodiode attached to an integrating sphere. Electroluminescence spectra were recorded using an ORIEL CCD spectrometer. UV-VIS transmission spectra were measured using a Perkin-Elmer λ9 spectrophotometer. Photoluminescence (PL) emission spectra were recorded using a Shimadzu RF5301 spectrofluorometer. For the photoinduced absorption measurements the samples were mounted in a cryostat and

cooled to a temperature of 80 K. As transmission source we used a standard 160 W halogen lamp. As excitation source an Ar⁺ laser operated in the multi line UV mode (3,64 eV, 3,42 eV) was used. All photoinduced absorption spectra are corrected for the optical throughput of the set-up. The life times of the triplet excitons have been determined by modulation spectroscopy from frequency dependent photoinduced absorption measurements at an energy of 1,3 eV.

Blends of semiconducting polymers:

For the preparation of the mixtures of two polymers in each particle, 20 mg of MeL-PPP and 20 mg of PF2/6 were dissolved in 2.3 g (to obtain 150 nm particles) or 4.3 g (to obtain 64 nm particles) of chloroform. Each polymer solution was then mixed with 10 g of an aqueous SDS solution (2.4 wt.% related to the amount of chloroform) and stirred for 1 h for pre-emulsification. The miniemulsion was prepared by ultrasonication the mixture for 2 min at 70 % amplitude (Branson sonifier W450) using a microtip. After sonication the sample was stirred at 62 °C in order to evaporate the CHCl₃. Table 1 summarizes the characteristics of the different dispersion used for the measurements.

7 Appendix

7.1 Methods

Dynamic light scattering

The particle sizes were measured using a Nicomp particle sizer (Model 370, PSS Santa Barbara, USA) at a fixed scattering angle of 90°.

Electron Microscopy

Electron microscopy was performed with a Zeiss 912 Omega electron microscope operating at 100 kV. The diluted colloidal solutions were applied to a 400-mesh carbon-coated copper grid and left to dry; no further contrasting was applied.

Atomic Force Microscopy

Atomic force microscopy (AFM) was performed with a NanoScope IIIa microscope (Digital Instruments, Santa Barbara) operating in tapping mode. The instrument was equipped with a 10 x 10 micrometer E-Scanner and commercial silicon tips (model TSEP, the force constant was $50 \text{ N}\cdot\text{m}^{-1}$, the resonance frequency was 300 kHz and the tip radius was smaller than 20 nm).

Differential Scanning Calorimetry (DSC)

The DSC measurements were carried out using a Netzsch Thermal Analyse DSC 200.

Cooling and heating rates of $5 \text{ K}\cdot\text{min}^{-1}$ were used for all measurements. Sample masses between 10 and 20 mg were used. The cooling step was done using liquid nitrogen.

The measurements were carried out in two different modes, the scanning and the isothermal mode. In the first type of measurement the heat evolved by a sample as it was cooled or heated at a constant rate was measured. In the second one the heat evolved was recorded as a function of time when a sample was held at a fixed temperature.

For the isothermal method the sample was cooled to 3 degrees before the crystallization temperature, held for 1 min, then cooled quickly ($30 \text{ K}\cdot\text{min}^{-1}$) and held at that point for 5 min to enable full droplet crystallization.

Interfacial Tension

The surface and interfacial tension measurements were performed at room temperature with the K12 processor tensiometer from Krüss employing the DuNöuy-Ring method. The radius of the Pt-Ir ring RI12 was 9.545 mm, and the wire had a radius of 0.185 mm.

Wide Angle X-ray (WAXS)

The wide angle X-ray (WAXS) diffraction was measured in a Nonius CP120 Diffractometer using a Cu-K α radiation ($\lambda = 1.54 \text{ \AA}$)

The diffraction of the miniemulsion samples was measured at a temperature below the crystallization temperature of the droplets as well as for the bulk phases, as determined by DSC. The hydroxyapatite-gelatin samples were measured at dried conditions.

Absorption Spectra

Absorption spectra were measured in the group of D. Neher with a Perkin Elmer Lambda 19 UV/Vis spectrometer. The spectrum of the sample was corrected for the transmission of an uncoated glass slide.

Fluorescence Spectra

Fluorescence spectra were recorded in the group of D. Neher with a Perkin Elmer LS 50 luminescence spectrometer. The excitation was incident at an angle of 60° onto the front face of the sample and the emission was recorded in reflection at an angle of 30° with respect to the normal surface. For the dilution experiments the miniemulsions were diluted with MilliQ water.

Fourier Transform Infrared (FTIR) spectroscopy

The FTIR spectra of the dried samples were recorded on an FTS 6000 spectrometer (Bio-Rad).

7.2 Abbreviations and symbols

σ	Polydispersity
θ	Scattering angle
η	Viscosity
Γ	Cumulant
γ	Interface/surface tension
Π_{osm}	Osmotic pressure
A	Amplitude
AFM	Atomic force microscopy
cmc	Critical micelle concentration
D	Diffusion coefficient
DLS	Dynamic light scattering
DSC	Differential scanning calorimetry
EL	Electroluminescence
f	Frequency
FTIR	Fourier Transform Infrared
HAP	Hydroxyapatite
HLB	Hydrophilic-lipophilic balance
k	Spring constant
K_B	Boltzmann constant
MEH-PPV	poly(2-methoxy-5-(2'-ethyl-hexoxy)-1,4-phenylenevinylene)
Me-LPPP	Methyl substituted ladder-type poly(<i>para</i> -phenylene)
PCPDT	Poly(2,6-(4,4-dialkyl)-4 <i>H</i> -cyclopenta[2,1-b:3,4-b']dithiophene)
PF(11112)	poly(9,9-bis(3,7,11-trimethyldodecyl)fluorene-2,7-diyl)
PF(2/6)	poly(9,9-bis(2-ethylhexyl)fluorene-2,7-diyl)
P_{Laplace}	Laplace pressure
PL	Photoluminescence
PPV	poly(<i>p</i> -phenylenevinylene)
s	second
SAXS	Small angle X-ray
T	Temperature

t	Time
TEM	Transmission electron microscopy
US	Ultrasound
WAXS	Wide angle X ray scattering

8 References

- 1 W. D. Bancroft, *Applied Colloid Chemistry: General Theory*. (Mc-Graw-Hill, New York, 1921).
- 2 K. Landfester, *Adv. Mater.* **13** (10), 765 (2001); K. Landfester, *Macromol. Rapid. Comm.* **22**, 896 (2001).
- 3 G. Jeronimidis, presented at the The 35th John Player Memorial Lecture, London, 2000 (unpublished).
- 4 J. F. V. Vincent, in *Encyclopaedia Britannica Yearbook* (Bettman Archive, 1995), pp. 169.
- 5 S. Mann, *Biomaterialization and biomimetic materials chemistry*. (VCH, New York, 1996).
- 6 Klaus Tauer, in *Handbook of Applied Surface and Colloid Chemistry*, edited by Krister Holmberg (John Wiley & Sons, 2001), pp. 176.
- 7 M. Willert, Universität Potsdam, 2001.
- 8 Katharina Landfester, Habilitationsschrift, Universität Potsdam (2002).
- 9 Y. J. Chou, M. S. El-Aasser, and J. W. Vanderhoff, *J. Dispers. Sci. Technol.* **1**, 129 (1980).
- 10 W. Z. Ostwald, *Phys. Chem.* **37**, 385 (1901).
- 11 W. I. Higuchi and J. Misra, *J. Pharmaceutical Sci.*, 459 (1962).
- 12 A. S. Kabalnov, A. V. Pertzov, and E. D. Shchukin, *J. Colloid Interf. Sci.* **118**, 590 (1987).
- 13 I. M. Lifshitz and V. V. Slyozov, *J. Phys. Chem. Solids* **19**, 35 (1961).
- 14 A. J. Webster and M. E. Cates, *Langmuir* **14**, 2068 (1998).
- 15 H. Köhler, *Geofysiske publikasjoner* **2**, 3 (1922).
- 16 V. K. LaMer and R. Gruen, *Trans. Faraday Soc.* **48**, 410 (1952).
- 17 K. Welin-Berger and B. Bergenstahl, *International Journal of Pharmaceutics* **200**, 249 (2000).

18 M. Postel, J. G. Riess, and J. G. Weers, *Art. Cells, Blood Subs., ANd Immob. Biotech.* **22**, 991 (1994); K. C. Lowe, *Art. Cells, Blood Subs., and Immob. Biotech.* **28**, 25 (2000).

19 S. S. Davis, H. P. Round, and T. S. Purewal, *J. Coll. Interf. Sci.* **80**, 508 (1981).

20 B. Abismail, J. P. Canselier, A. M. Wilhelm et al., *Ultrasonics Sonochemistry* **6**, 75 (1999).

21 P. Walstra, *Chem. Eng. Sci.* **48**, 333 (1993); S. E. Friberg and S. Jones, 4th ed. (Wiley, New York, 1994).

22 R. W. Wood and A. L. Loomis, *Phil. Mag.* **4**, 417 (1927).

23 V. I. Sorokin, *Soviet Phys./Acoust.* **3**, 281 (1957); M. K. Li and H. S. Fogler, *J. Fluid Mech* **88**, 499 (1978); M. K. Li and H. S. Fogler, *J. Fluid Mech.* **88**, 513 (1978).

24 E. S. Rajagopal, *In Emulsion Science*. (Academic Press, London, 1968).

25 C. Bondy and K. Söllner, *Trans. Faraday Soc.* **31**, 835 (1935); T. J. Mason, *Ultrasonics Sonochemistry* **30**, 192 (1992).

26 W. Lauterborn, *Ultrasonics Sonochemistry* **4**, 65 (1997).

27 O. Behrend, K. Ax, and H. Schubert, *Ultrasonics Sonochemistry* **7**, 77 (2000).

28 K. J. J. Fontenot and F. J. Schork, presented at the In 4th International Workshop on Polymer Reaction Engineering, Weinheim, Germany, 1992 (unpublished); K. Fontenot and F. J. Schork, *Ind. Eng. Chem. Res.* **32**, 373 (1993).

29 K. Landfester, N. Bechthold, F. Tiarks et al., *Macromolecules* **32**, 5222 (1999).

30 K. Landfester, M. Willert, and M. Antonietti, *Macromolecules* **33**, 2370 (2000).

31 G. W. Burton and C. P. O'Farrell, *J. Elastomers and Plastics* **9**, 94 (1977).

32 J. B. Tuttle, *The India Rubber World* **January 1**, 213 (1923); J. B. Tuttle, *The India Rubber World* **May 1**, 488 (1923).

33 J. B. Tuttle, *The India Rubber World* **February 1**, 291 (1923).

34 J. B. Tuttle, *The India Rubber World* **January 1**, 219 (1924).

35 R. Ditmar, *Chemiker-Zeitung* **47**, 711 (1923).

36 A. Beerbower, G. W. Burton, and P. L. Malloy, United States of America Patent No. 3.998.772 (Dec. 21, 1976 1976).

- 37 J. W. Vanderhoff, M. S. El-Aasser, and J. Ugelstad, United States of America
Patent No. 4177177 (Dec. 4, 1979 1979).
- 38 M. S. El-Aasser, J. W. Vanderhoff, A. Humayun et al., *J. Coatings Technol.* **56**,
37 (1984).
- 39 K. E. Johnsen and R. R. Pelletier, United States of America Patent No. 5500469
(Mar. 19, 1996 1996).
- 40 D. B. Fahrenheit, *Phil. Trans. Roy. Soc.* **39**, 78 (1724).
- 41 W. J. Dunning, in *in Nucleation*, edited by A. C. Zettlemoyer (Marcel Dekker,
New York, 1969), pp. 1.
- 42 G. E. Fischer. (1804).
- 43 J. T. Lowitz, *Crells Chemische Annalen* **1**, 3 (1795).
- 44 J. L. Gay Lussac, *Ann de Chemie* **87**, 225 (1813); J. L. Gay Lussac, *Ann de*
Chemie **11**, 296 (1819).
- 45 H. Schröder and von Dusch, *Leibigs Annalen* **89**, 232 (1853); H. Schröder and
von Dusch, *Leibigs Annalen* **109**, 35 (1859); C. Violette, *Compte. Rend.* **60**, 831
(1865).
- 46 D. Gernez, *Compte. Rend.* **60**, 833 (1865); D. Gernez, *Compte. Rend.* **61**, 71
(1865).
- 47 W. Ostwald, *Z. Phys. Chem.* **22**, 289 (1897).
- 48 Lecoq de Boisbaudran, *Compte. Rend.* **63**, 95 (1866).
- 49 L. C. Coppet, *Ann. Chim. Phys.* **6**, 275 (1875).
- 50 W. Ostwald, *Z. Phys. Chem.* **34**, 493 (1900).
- 51 G. Tammann, *Z. Phys. Chem.* **25**, 441 (1898).
- 52 J. W. Gibbs, *Trans. Connect. Acad.* **3**, 108 (1876); J. W. Gibbs, *Trans. Connect.*
Acad. **3**, 343 (1878).
- 53 I. V. Markov, *Crystal Growth for Beginners: Fundamentals of Nucleation,*
Crystal Growth and Epitaxy. (World Scientific Publishing Co. Pte. Ltd., 1995).
- 54 M. Volmer and A. Weber, *Z. Phys. Chem.* **119**, 227 (1926).
- 55 L. Farkas, *Z. Phys. Chem.* **125**, 239 (1927).
- 56 I. N. Stranski and R. Kaischew, *Z. Phys. Chem.* **B26**, 100 (1934).
- 57 R. Becker and W. Döring, *Ann. Phys.* **24**, 719 (1935).

- 58 I. Ya Frenkel. (Dover, 1955).
- 59 K. F. Kelton, in *Solid State Physics: Advances in Research and Applications*,
edited by Henry Ehrenreich and David Turnbull (Academic, New York, 1991),
Vol. 45, pp. 75.
- 60 J. E. Hilliard. (American Society for metals, Metals Park, OH, 1970); H. Herman
and R. K. MacCrone, *J. Am. Ceram. Soc.* **55**, 50 (1971); C. M. F. Jantzen and H.
Herman. (Academic Press, New York, 1978).
- 61 V. Gerold and G. Kostorz, *J. Appl. Crystallogr.* **11**, 376 (1978); K. Hono and
Ken-Ichi Hirano, *Phase Transitions* **10**, 223 (1987).
- 62 Ph. Carlach, *Online Nanotechnologies Journal* **2** (2), 1 (2001).
- 63 D. Turnbull, *J. Chem. Phys.* **18**, 198 (1950).
- 64 J. W. Christian, 2nd ed. (Pergamon Press, Oxford, 1975).
- 65 H. Biloni, in *Physical Metallurgy*, edited by R. W. Cahn and P. Haasen (North-
Holland, Amsterdam, 1983), pp. 477; R. D. Doherty, in *Physical Metallurgy*,
edited by R. W. Cahn and P. Haasen (North-Holland, Amsterdam, 1983), pp.
477.
- 66 J. E. Shelby, *Introduction to Glass Science and Technology*. (The Royal Society
of Chemistry, 1997).
- 67 Richard R. Vanfleet and J. M. Mochel, *Surface Tension* **341**, 40 (1995).
- 68 N. Kaneko, T. Horie, S. Ueno et al., *Journal of Crystal Growth* **197**, 263 (1999).
- 69 D. Julian McClements, Eric Dickinson, Stephanie R. Dungan et al., *Journal of
colloid and interface Science* **160**, 293 (1993).
- 70 A. Schreiber, I. Ketelsen, and G. H. Findenegg, *Phys. Chem. Chem. Phys.* **3**, 1185
(2001).
- 71 B. Vonnegut, *J. Coll. Sci.* **3**, 563 (1948).
- 72 D. Turnbull, *J. Chem. Phys.* **20**, 411 (1952).
- 73 D. Turnbull and R. L. Cormia, *J. Chem. Phys.* **34**, 820 (1961).
- 74 H. F. Milhofer, N. Garti, and A. Kamyshny, *J. Cryst. Growth* **199**, 1365 (1999); J.
F. Yano, H. Milhofer, E. Wachtel et al., *Langmuir* **16**, 10005 (2000).
- 75 S. Charoenrein and D. S. Reid, *Thermochimica Acta* **156**, 373 (1989).

- 76 D. J. McClements, S. R. Dungan, J. B. German et al., *Journal of food science* **58**,
1148 (1993).
- 77 P. Walstra and E. C. H. Berensteyn, *Neth Milk Dairy J.* **29**, 35 (1975).
- 78 D. Turnbull and R. E. Cech, *J. Appl. Phys.* **21**, 804 (1950).
- 79 J. H. Perepezko, *Mat. Sci. Eng.* **65**, 125 (1984).
- 80 D. J. McClements, E. Dickinson, and M. J. W. Povey, *Chem. Phys. Lett.* **172**, 449
(1990); E. Dickinson, F. J. Kruizenga, M. J. W. Povey et al., *Colloids Surf. A* **81**,
273 (1993).
- 81 A. B. Herhold, D. Ertas, A. J. Levine et al., *Physical Review E* **59**, 6946 (1999).
- 82 D. Turnbull, *J. Appl. Phys.* **21**, 1022 (1950).
- 83 A. M. Taggart, F. Voogt, G. Clydesdale et al., *Langmuir* **12**, 5722 (1996).
- 84 A. Baeyer, *Ber. Chem. Ges* **10**, 1286 (1877).
- 85 Roland Boese, Hans-Christoph Weiss, and Dieter Bläser, *Angew. Chem. Int. Ed.*
38 (7), 988 (1999).
- 86 A. Müller, *R. Soc. London Ser. A* **138**, 514 (1932).
- 87 W. M. Mazee, *Rec. Trav. Chim. Pays-Bas* **67**, 197 (1948); K. Larsson, *Nature* **13**,
383 (1967).
- 88 G. Ungar and N. Masic, *J. Phys. Chem.* **89**, 1036 (1985); J. Doucet, I. Denicolo,
and A. Craievich, *J. Chem. Phys.* **75**, 1523 (1981); G. Ungar, *J. Phys. Chem.* **87**,
689 (1983); D. L. Dorset, *EMSA Bull* **20**, 54 (1990).
- 89 J. Doucet, I. Denicolo, A. Craievich et al., *J. Chem. Phys.* **80**, 1647 (1984).
- 90 I. Denicolo, A. F. Craievich, and J. Doucet, *J. Chem. Phys.* **80** (12), 6200 (1984).
- 91 E. B. Sirota and A. B. Herhold, *Polymer* **41**, 8781 (2000).
- 92 E. B. Sirota, J. King, D. M. Singer et al., *J. Chem. Phys.* **98**, 5809 (1993).
- 93 Amy B. Herhold, H. E. King Jr., and E. B. Sirota, *J. Chem. Phys.* **116** (20), 9036
(2002).
- 94 M. J. Oliver and P. D. Calvert, *J. Cryst. Growth* **30**, 343 (1975).
- 95 E. B. Sirota and A. B. Herhold, *Science* **283**, 529 (1999).
- 96 D. M. Small, *The Physical Chemistry of Lipids: from Alkanes to phospholipids*
(Plenum, New York) (1986).
- 97 E. B. Sirota, H. E. King Jr., H. H. Shao et al., *J. Phys. Chem.* **99**, 798 (1995).

- 98 J. Woodlouse, *Online Nanotechnologies Journal* **2** (2) (2001).
- 99 F. Banfield and et al., *Science* **289**, 751 (2000).
- 100 D. A. Bazylinski and et al., *App. and Env. Microbiology*, 3232 (1995).
- 101 D. Acost-Avalo and et al., *J. Exp. Biol.* **202** (2687-2692) (1999).
- 102 C. Hsu and C. Li, *J. Exp. Biol.* **180**, 1 (1993).
- 103 M. W. Walker, *Nature* **390**, 339 (1997).
- 104 S. Mann and D. Walsh, *Nature* **377**, 320 (1995).
- 105 Jia Kui Li, Muo Wang, and Xue Shen Wu, *J. Microencapsulation* **15** (2), 163
(1998).
- 106 Young Seon Choi, Sung Ran Hong, Young Moo Lee et al., *Biomaterials* **20**, 409
(1999).
- 107 P. J. Rose, H. F. Mark, N. M. Bikales et al., *Encyclopedia of polymer science and
engineering*. ed. New York, USA **7**, 488 (1989).
- 108 M. Djabourov and P. Papon, *Polymer* **24**, 537 (1983).
- 109 R. A. Jonas, G. Ziemer, F. J. Schoen et al., *J. Vasc. Surg.* **7**, 414 (1988); N.
Chakfe, Y. Marois, R. Guidoin et al., *Polym. Polym. Comput.* **1**, 229 (1993).
- 110 G. A. Digenis, T. B. Gold, and V. P. Shah, *J. Pharm. Sci* **83**, 915 (1994); E.
Esposito, R. Cortesi, and C. Nastruzzi, *Biomater.* **20**, 2009 (1995); Y. Otani, Y.
Tabata, and Y. Ikada, *Biomater.* **19**, 2091 (1998).
- 111 R. C. Oppenheim, *Int. J. Pharm.* **8**, 217 (1981); S. E Leucuta, *Drug Dev. Ind.
Pharm.* **12**, 2281 (1986); N. Tanaka, S. Takino, and I. Utsumi, *J. Pharm. Sci* **52**,
664 (1963); S. E Leucuta, G. Ponchel, and D. Duchene, *J. Microencapsulation* **14**,
511 (1997); Y. Tabata and Y. Ikada, *Pharm. Res.* **6**, 422 (1989).
- 112 M. A. Vandelli, F. Rivasi, P. Guerra et al., *Int. J. Pharm.* **215**, 175 (2001).
- 113 C. Chemtob, T. Assimacopoulos, and J. C. Chaumeil, *Drug Dev. Ind. Pharm.* **14**,
1359 (1988); B. Hazel, O.Roy, G. Roy et al., *Biochim Biophys Acta* **632**, 589
(1980).
- 114 G. Raymond, M. Degennaro, and R. Mikeal, *Drug Dev. Ind. Pharm.* **16**, 1025
(1990); O. Damink, P. J. Dijkstra, V. Luyn et al., *J. Mater. Sci. Mat. Med.* **6**, 460
(1995).
- 115 Y. Otani, Y. Tabata, and Y. Ikada, *J. Biomed. Mater. Res.* **31**, 157 (1996).

- 116 H. W. Sunk, H. L. Hsu, C. C. Shih et al., *Biomater.* **17**, 1405 (1996).
- 117 O. Damink, P. J. Dijkstra, V. Luyn et al., *J. Mater. Sci. Mat. Med.* **6**, 429 (1995).
- 118 K. Weadock, R. M. Olson, and F. H. Silver, *Biomater. Med. Dev. Art. Org.* **11**,
293 (1983).
- 119 R. C. Oppenheim and N. F. Stewart, *Drug Dev. Ind. Pharm.* **5**, 583 (1979); Y.
Tabata and Y. Ikada, *Pharm. Res.* **6**, 422 (1994).
- 120 R. Lakes, *Nature* **361**, 511 (1993).
- 121 S. Mann, *Nature* **365**, 499 (1993).
- 122 J. Currey. (Princeton, New Jersey, 1984).
- 123 B. S. Kraus, R. E. Jordan, and L. Abrams. (Williams & Williams, Baltimore,
1969).
- 124 A. L. Boskey, T. M. Wright, and R. D. Blank, *J. Biomed. Mater. Res.* **14**, 330
(1999).
- 125 L. Gineste, M. Gineste, X. Ranz et al., *J. Biomed. Mater. Res.* **48**, 224 (1999); G.
Carotenuto, G. Spagnuolo, L. Ambrosio et al., *J. Mater. Sci. Mater. Med.* **10**, 671
(1999).
- 126 L. L. Hench, *J. Am. Ceram. Soc.* **74**, 1487 (1991).
- 127 T. Kokubo, presented at the XVI int. Cong. Glass., Madrid, 1992 (unpublished).
- 128 S. Busch, U. Schwarz, and R. Kniep, *Chem. Mat.* **13**, 3260 (2001).
- 129 P. W. M. Blom and M. C. J. M. Vissenberg, *Materials Science & Engineering* **27**,
53 (2000).
- 130 Achmad Zen, Universität Potsdam, 2002.
- 131 C. K. Chiang, J. Fincher, Y. W. Park et al., *Phys. Rev. Lett.* **39**, 1098 (1977).
- 132 P. L. Burn, A. B. Holmes, A. Kraft et al., *J. Chem. Soc., Chem. Commun.* **32**
(1992); P. L. Burn, A. Kraft, D. D. C. Bradley et al., *J. Am. Chem. Soc.* **115**, 10117
(1993); D. A. Halliday, P. L. Burn, D. D. C. Bradley et al., *Adv. Mater.* **5**, 40
(1993).
- 133 D. Braun and A. J. Heeger, *Appl. Phys. Lett.* **58**, 1982 (1991); Y. Cao
Gustavsson, G. M. Treacy, F. Klavetter et al., *Nature* **357**, 477 (1992); I. D.
Parker, *J. Appl. Phys.* **75**, 1656 (1994).
- 134 N. C. Greenham, S. C. Moratti, D. D. C. Bradley et al., *Nature* **365**, 628 (1993).

- 135 J. Birgerson, M. Fahlman, P. Bröms et al., *Synthetic Metals* **80**, 125 (1996).
- 136 U. Scherf, *J. Mat. Chem.* **9**, 1853 (1999).
- 137 G. Lanzani, S. De Silvestri, G. Cerullo et al., in *Semiconducting Polymers*, edited
by G. Hadziioannou and P. F. van Hutten (Wiley-VCH, Weinheim, 1999), pp.
Chapter 9.
- 138 M. Gross, D. C. Müller, H.-G. Nothofer et al., *Nature* **405**, 661 (2000); T. Miteva,
A. Meisel, W. Knoll et al., *Adv. Mater.* **13**, 565 (2001); D. C. Müller, T. Braig,
H.-G. Nothofer et al., *ChemPhysChem* **1**, 207 (2000).
- 139 U. Asawapirom and U. Scherf, *Macromol. Rapid Commun.* **22**, 746 (2001).
- 140 R. H. Friend, R. W. Gymer, A. B. Holmes et al., *Nature* **397**, 121 (1999).
- 141 C. J. Brabec, N. S. Sariciftci, and J. C. Hummelen, *Adv. Funct. Mater.* **11**, 15
(2001).
- 142 A. R. Brown, C. P. Jarrett, D. M. Deleeuw et al., *Synthetic Metals.* **88**, 37 (1997).
- 143 T. R. Hebner and J. C. Sturm, *Appl. Phys. Lett.* **73**, 1775 (1998); T. R. Hebner, C.
C. Wu, D. Marcy et al., *Appl. Phys. Lett.* **72**, 519 (1998); L. M. Leung, C. F.
Kwong, C. C. Kwok et al., *Displays* **21**, 199 (2000); Y. Yang, S. C. Chang, J.
Bharathan et al., *J. Mater. Sci.-Mater.* **11**, 89 (2000).
- 144 K. Mori, T. L. Ning, M. Ichikawa et al., *Jpn. J. Appl. Phys. Part 2 - Lett.* **39**, L942
(2000); Z. N. Bao, Y. Feng, A. Dodabalapur et al., *Chem. Mat.* **9**, 1299 (1997).
- 145 K. S. Whitehead, M. Grell, D. D. C. Bradley et al., *Appl.Phys.Lett.* **76**, 2946
(2000); A. E. A. Contoret, S. R. Farrar, P. O. Jackson et al., *Adv. Mater.* **12**, 971
(2000).
- 146 B.L Groenendaal, F. Jonas, D. Freitag et al., *Adv. Mater.* **12**, 481 (2000).
- 147 J. J. M. Halls, C. A. WALSH, N. C. GREENHAM et al., *Nature* **376**, 498 (1995);
G. Yu, J. Gao, J. C. Hummelen et al., *Science* **270**, 1789 (1995).
- 148 M. Böltau, S. Walheim, J. Mlynek et al., *Nature* **391**, 877 (1998); G. Krausch,
Materials Science & Engineering R-Reports **14**, 1 (1995); S. Walheim, M. Böltau,
J. Mlynek et al., *Macromolecules* **30**, 4995 (1997); P. Müller-Buschbaum, J. S.
Gutmann, and M. Stamm, *Macromolecules* **33**, 4886 (2000); J. J. M. Halls, A. C.
Arias, J. D. MacKenzie et al., *Adv. Mater.* **12**, 498 (2000); S. E. Shaheen, C. J.
Brabec, N. S. Sariciftci et al., *Appl. Phys. Lett.* **78**, 841 (2001).

149 I. W. Hamley. (Oxford University Press, New York, 1998); K. Binder. (1999).
150 C. Schmitt, H.-G. Nothofer, A. Falcou et al., *Macromol. Rapid. Comm* **22**, 624
(2001); D. M. Johansson, M. Theander, T. Granlund et al., *Macromolecules* **34**,
1981 (2001).
151 C. W. Macosko, P. Guegan, A. K. Khandpur et al., *Macromolecules* **29**, 5590
(1996); M. A. Hillmyer, W. W. Maurer, T. P. Lodge et al., *J. Phys. Chem. B* **103**,
4814 (1999).
152 H. Pernot, M. Baumert, F. Court et al., *Nature Materials* **1**, 54 (2002).
153 R. Jenkins and R. L. Snyder. (John Wiley & Sons, New York, 1996).
154 M. von Laue, *Muench. Sitzungsber.*, 363 (1912).
155 S. F. Sun. (John Wiley & Sons, New York, 1994).
156 P. Scherrer, *Nachr. Ges. Wiss. Göttingen, Math.-Phys. Kl.* **2**, 96 (1918).
157 H. P. Klug and L. E. Alexander, 2nd ed. (Wiley (Interscience), New York, 1974).
158 G. Binning, C. Quate, and Ch. Gerber, *Phys. Rev. Lett.* **56**, 930 (1986).
159 S. N. Magonov and M.-H. Whangbo. (VCH, Weinheim, 1996).
160 T. R. Albrecht, S. Akamine, T. E. Carver et al., *J. Vac. Sci. Technol. A* **8**, 3386
(1990).
161 P. K. Hansma and J. Tersoff, *J. Appl. Phys.* **61**, R1 (1987); S. Park and C. F.
Quate, *Rev. Sci. Instrum.* **58**, 2010 (1987); D. Sarid. (Oxford University Press,
New York, 1991); C. J. Chen. (Oxford University Press, New York, 1993).
162 J. P. Cleveland, S. Manne, D. Bocek et al., *Rev. Sci. Instrum.* **64**, 1 (1993).
163 R. Montenegro, M. Antonietti, Y. Mastai et al., *J. Phys. Chem. B* **Submitted**
(2002); R. Montenegro and K. Landfester, *Langmuir* **Accepted** (2003).
164 J. W. Cahn and J. E. Hilliard, *J. Chem. Phys.* **28**, 258 (1958); J. W. Cahn and J. E.
Hilliard, *J. Chem. Phys.* **31**, 688 (1959).
165 D. Cullity. (Addison-Wesley Pub. Inc., Reading, MA, 1978).
166 J. P. Dumas, M. Krichi, M. Strub et al., *Int. J. Heat Mass Transfer.* **37** (5), 737
(1994).
167 A. Röttele, T. Thurn-Albrecht, J.-U. Sommer et al., *Macromolecules* **in press**
(2003).

- 168 A. R. Gerson, K. J. Roberts, J. N. Sherwood et al., *J. Cryst. Growth* **128**, 1176
(1993).
- 169 K. J. Roberts, J. N. Sherwood, and A. M. Taggart, *Proceedings from 12th
Symposium on Industrial Crystallization* **3**, 63 (1993).
- 170 Katharina Landfester, *Advanced Materials* **13** (10), 765 (2001).
- 171 E. Leo, M. A. Vandelli, R. Cameroni et al., *Int. J. Pharm.* **155**, 75 (1997).
- 172 M. Antonietti, M. Breulmann, C. G. Göltner et al., *Chem. Eur. J.* **4** (12), 2493
(1998).
- 173 R. Lee Penn and Jillian F. Banfield, *Geochimica et Cosmochimica Acta* **63** (10),
1549 (1999).
- 174 A. C. Tas, *J. Am. Ceram. Soc.* **84** (2), 295 (2001).
- 175 K. Landfester, R. Montenegro, U. Scherf et al., *Adv. Mater.* **14** (9), 651 (2002);
U. Asawapirom, F. Bulut, T. Farrell et al., *Macromol. Symp.* **Accepted** (2003).
- 176 J. Cho, K. Char, J. D. Hong et al., *Adv. Mater.* **13**, 1076 (2001).
- 177 M. Grell, W. Knoll, D. Lupo et al., *Adv. Mater.* **11**, 671 (1999).
- 178 E. J. W. List, R. Güntner, P. Scanducci de Freitas et al., *Adv. Mater.* **14**, 374
(2002).
- 179 T. Piok, S. Gamerith, C. Gadermaier et al., *Adv. Mater.* **Accepted** (2003).
- 180 H. W. Deckman and J. H. Dunsmuir, *Appl. Phys. Lett.* **41** (4), 377 (1982); Y. Xia
and et al., *Adv. Mater.* **12** (10), 693 (2000).
- 181 N. Koch, A. Pogantsch, E. J. W. List et al., *Appl. Phys. Lett.* **74**, 2909 (1999).
- 182 Q. Pei, G. Yu, C. Zhang et al., *Science* **269**, 1086 (1995).
- 183 T. Kietzke, D. Neher, K. Landfester et al., *Nature Materials* **Submitted** (2002).
- 184 D. Neher, *Macromol. Rapid Commun.* **22**, 1366 (2001).
- 185 Y. Zhao, J. Levesque, P. C. Roberge et al., *J. Polym. Sci. Part B-Polymer Physics*
27, 1955 (1989); M. Jiang, W. J. Chen, and T. Y. Yu, *Polymer* **32**, 984 (1991).
- 186 M. A. Winnik, *Current Opinion in Colloid & Interface Science* **2**, 192 (1997).
- 187 D. C. Blackley. (Chapman & Hil, London, 1997).
- 188 H. Schlaad, H. Kukula, J. Rudloff et al., *Macromolecules* **34**, 4302 (2001); A.
Thomas, H. Schlaad, B. Smarsly et al., *Langmuir* **Submitted** (2003).

- ¹⁸⁹ U. Scherf and K. Müllen, *Macromol. Rapid Commun.* **12**, 489 (1991); U. Scherf, *J. Mat. Chem.* **9**, 1853 (1999); U. Scherf, A. Bohnen, and K. Müller, *Macromol. Chem.* **193**, 1127 (1992).
- ¹⁹⁰ D. Lieser, M. Oda, T. Miteva et al., *Macromolecules* **33**, 4490 (2000).
- ¹⁹¹ U. Scherf and E. J. W. List, *Adv. Mater.* **14**, 477 (2002).

Acknowledgments

I would like to express my acknowledgements to all those who directly or indirectly helped me for the successful conclusion of this work at MPI.

I have indeed an enormous list of very important names.

Firstly I would like to thank Prof. Markus Antonietti for the great opportunity to work in his department and for the support, encouragement and discussions.

Many thanks to Katharina Landfester, our group leader, for all the brilliant ideas, encouragement, help and for bringing me to the “world of the miniemulsions”.

Special thanks to our collaborators: Prof. U. Scherf from the University of Wuppertal and his group, Prof. D. Neher from the University of Potsdam and his PhD student Thomas Kietzke, and Emil List from the Graz University of Technology.

Angelo Valleriani, coordinator of the IMPRS, *grazie per tutto*.

Helmut Cölfen, for the useful discussions concerning biomineralization.

Thanks to all the group members, both new and former ones: Regina (*danke für alles. Ich wünsche dir und deiner Familie alles Gute*), Liliana (*gracias por todo y buena suerte en la defensa e en el futuro*), Christian (thanks for the intelligent discussions and the nice environment in the office), Andreas (thanks for the explanations on chemistry and the passes in the football matches), Oychai, Matthieu, Ufuk, Dirk (thanks for your friendship), Emmanuelle (*merci de tout que vous avez fait pour nous*), Mirjam (thanks for everything) and Franca.

Viktor and Sophie, my former officemates, thanks for the nice time together.

Anne Heilig and Roy Knocke for the wonderful AFM pictures, Ingrid Zenke and Bernd Smarsly for the X-ray measurements and for teaching me how to use it, Carmen Remde for the DSC, Jürgen Hartmann and Rona Pitschke for the TEM measurements.

For the help with the biomineralization experiments, I would like to thank Jordis.

All the other students, post-docs, staff and table-football players who helped me: Yitzhak, Karin, Atul, Conny, Nathan, Ana, Antje, Cilaine, Sandra, Liying, Sebastian, Gordon, Vesko, Rumi, Paul, Andreas, Reinhard, Valentina, Samira, Klaus, Theodora, Chris, Pape, Charl, Ines, Magda, Justyna, Stefan, Franck, Jeremy, Hans, Arne, Matthijs, Markus,

Julien, Hartmut, Byram, Remi, Pirok, Danielle, Jan, Doreen, Jessica, Christopher, Patrycja, Shu-Hong, Hannes, Guan, Hamilton, Yong and many others.

Thanks to the brothers and sisters from the 7th Day Adventist Church both in Potsdam and Berlin who showed us (to me and my wife) that we belong to a much bigger family, without frontiers. May God bless all of you. Among the lovely families we had the pleasure to meet in this church I would like to point out the Engel, Oppermann and Schwarz, who will certainly stay forever in our hearts and prayers.

To my family, that always supported my ideas and endeavors. I hope I made them proud of me. *Muito obrigado!*

Obviously I could not conclude these acknowledgements without thanking my lovely wife for her patience, support and love: *Muito obrigado por tudo, você sabe que eu te amo!*

I always wanted to visit Germany because it is the country of Bach, Beethoven, Luther, Gauss, Einstein and others who changed the world with their ideas, now I have reasons to miss it...my own friends.

Auf wiedersehen!